Dissertation

submitted to the

Combined Faculties for the Natural Sciences and for Mathematics

of the Ruperto-Carola University of Heidelberg, Germany

for the degree of

Doctor of Natural Sciences

presented by

Diploma-Physicist: Oksana Geithner

born in: Kharkov, Ukraine

Heidelberg, July 26, 2006

Monte Carlo simulations for heavy ion dosimetry

Referees: Prof. Dr. Oliver Jäkel

Prof. Dr. Josef Bille

Zusammenfassung

Rechnungen zur Bestimmung der Water-to-air Stopping Power Ratio ($s_{w,air}$) für die Ionisationskammer-Dosimetrie von klinisch relevanten Ionenstrahlen mit Energien von 50 bis 450 MeV/u wurden unter Verwendung der Monte Carlo Methode durchgeführt. Um den Transport von geladenen Teilchen in Wasser zu simulieren, wurde der Computercode SHIELD-HIT v2 verwendet, der eine substanzielle Weiterentwicklung seiner Vorgängerversion SHIELD-HIT v1 darstellt. Das Programm wurde in großen Teilen neu geschrieben, wobei single-precision Variablen durch double-precision Variablen ersetzt wurden. Die niedrigste für die Simulation relevante Teilchenenergie, wurde von 1 MeV/u auf 10 keV/u vermindert, indem eine Modifikation der Bethe-Bloch Formel eingeführt wurde. Somit wurde es möglich, den Einsatzbereich von SHIELD-HIT auf medizinisch-dosimetrische Anwendungsgebiete auszuweiten. MSTAR und ICRU-73 Stopping Power Daten können optional vom Anwender bei der Durchführung der Simulationen verwendet werden. Das Fragmentationsmodell wurde anhand einer Vielzahl zur Verfügung stehender experimenteller Daten verifiziert und somit einige Modellparameter angepasst. Die aktuelle Version des Codes zeigt eine hervorragende Übereinstimmung mit den experimentellen Daten. Zusätzlich zu den Berechnungen der Stopping Power Ratios $s_{w,air}$, wurde der Einfluss der Fragmente und *I*-Werte auf $s_{w,air}$ für Kohlenstoff-Ionenstrahlen untersucht. Für eine Energie von 50MeV/u weicht $s_{w,air}$ um bis zu 2.3% im Bereich des Bragg-Peaks vom durch TRS-398 empfohlenen Wert von 1.130 ab.

Abstract

Water-to-air stopping power ratio ($s_{w,air}$) calculations for the ionization chamber dosimetry of clinically relevant ion beams with initial energies from 50 to 450 MeV/u have been performed using the Monte Carlo technique. To simulate the transport of a particle in water the computer code SHIELD-HIT v2 was used which is a substantially modified version of its predecessor SHIELD-HIT v1. The code was partially rewritten, replacing formerly used single precision variables with double precision variables. The lowest particle transport specific energy was decreased from 1MeV/u down to 10 keV/u by modifying the Bethe-Bloch formula, thus widening its range for medical dosimetry applications. Optional MSTAR and ICRU-73 stopping power data were included. The fragmentation model was verified using all available experimental data and some parameters were adjusted. The present code version shows excellent agreement with experimental data. Additional to the calculations of stopping power ratios, $s_{w,air}$, the influence of fragments and *I-values* on $s_{w,air}$ for carbon ion beams was investigated. The value of $s_{w,air}$ deviates as much as 2.3% at the Bragg peak from the recommended by TRS-398 constant value of 1.130 for an energy of 50 MeV/u.

To my family

Table of Contents

List of Figures xiii

List of Tables xviii

1 Introduction 1

2 Materials and Methods 3

2.1 Dosimetry: Basics 3

2.1.1 Definition of absorbed dose *3*

2.1.2 Measurement of absorbed dose *5*

2.1.3 Cavity theory *6*

Bragg-Gray theory 6

Spencer-Attix theory 7

2.2 Dosimetry: Practical Aspects 8

2.2.1 Calorimeters *9*

2.2.2 Photographic Films *10*

2.2.3 Thermoluminescent Dosimeters *10*

2.2.4 Ionization chambers *12*

Principle 12

Correction factors 15

2.3 Dosimetry: Recommendation for heavy ion beams 16

2.3.1 $N_{D,w}$ based formalism *16*

2.3.2 Monte Carlo calculations of stopping power ratios for light ions *20*

2.3.3 Alternative approach *21*

2.3.4 Stopping Power: definition and main dependencies *22*

2.4 Monte Carlo: Technique 25

2.4.1 Modeling of nuclear reactions *25*

Exclusive approach 25

Inclusive approach 26

2.4.2 Monte Carlo hadron transport codes *27*

Development of SHIELD; SHIELD-HIT v1 28

2.5 Monte Carlo: Modifications of the SHIELD-HIT v1 for the application in heavy ion dosimetry; SHIELD-HIT v2 30

2.5.1 Transport in low density medium 31

2.5.2 Stopping power 31

External table data 31

Modification of Bethe-Bloch formula 31

2.5.3 Fragment production 32

2.6 Monte Carlo: Validation of SHIELD-HIT v2 using experimental data 33

Bragg curves 33

Production of fragments 34

Spatial distribution of derived fragments 34

3D Dose distribution derived from the scanned carbon beam 34

2.7 Measurements performed at GSI for present thesis 34

2.7.1 Monoenergetic Depth Dose profiles (Bragg curves) with ^{12}C and ^{3}He ion beams 36

2.7.2 Lateral profiles of the scanned cubic volume and Spread-Out Bragg Peak (SOBP) 37

2.8 Simulation with SHIELD-HIT v2 39

2.8.1 Simulations for the validation of the code 39

Bragg curves 39

Fragment production 40

3D Dose distributions 40

2.8.2 Calculation of the STPR 42

2.8.3 Simulations for antiprotons 43

2.8.4 Calculations of the F-factor 43

3 Results 45

3.1 Verification of SHIELD-HIT v2 45

3.1.1 Stopping Power 45

3.1.2 Depth Dose Profiles 46

3.1.3 Production of fragments 51

3.1.4 Comparison with GEANT4 55

3.1.5 Lateral Profiles of a Scanning Beam; SOBP 60

3.2 Calculation of Stopping Power Ratios for Heavy Ions dosimetry 66

3.2.1 Calculation of STPR using Stopping Power Data from ICRU reports 66

3.2.2 Calculation of STPR using BEST stopping power data with different I-values 73

3.3 Other Applications 77

3.3.1 Antiprotons 77

3.3.2 Particle Transport in Low Density Medium; F-factor 78

4 Discussion 81

4.1 The code validation 81

4.2 Stopping power ratios 85

4.2.1 Calculation with ICRU stopping power data 85

4.2.2 Calculation with BEST data using different I-values 87

4.3 Other applications of the SHIELD-HIT v2 88

5 Conclusions and Outlook 91

Appendix A 95

NMTC 95

FLUKA 97

MARS 98

GEANT 98

Appendix B 101

Appendix C 103

List of Publications and Conference Contributions 105

Bibliography 107

Acknowledgement 115

List of Figures

Figure 1 Schematic view of a dosimeter as a sensitive volume *V* (cavity), surrounded by medium 5

Figure 2 A typical thermogram (glow curve) of LiF:Mg,Ti measured with a TLD reader at a low heating rate. 11

Figure 3 TL response of a TLD-700 for a spherical volume with a homogeneous dose deposition of 1Gy [Geiss97]. The dotted line shows the absorbed dose. 12

Figure 4 Schematic view of a cylindrical (thimble) ionization chamber 13

Figure 5 Schematic view of a plate parallel ionization chamber in a simple electrical circuit 13

Figure 6 Sketch of the Current-Voltage characteristic of an ionization chamber shown in Fig.5. 14

Figure 7 Schematic picture of a Roos chamber (cross-section) in a water phantom. 21

Figure 8 Schematic view of nuclear reaction in exclusive approach. 26

Figure 9 Schematic view of nuclear reaction in inclusive approach. 27

Figure 10 Schematic overview of hadron transport codes. 29

Figure 11 Schematic view of the active beam delivery system used at GSI. The pencil beam is scanned over the transversal area by the deflection magnets, while the penetration depth is modified by an active variation of the beam energy from synchrotron. 36

Figure 12 Set of devices used for the measurements. Left: PMMA phantom filled with water with array of pin-point ionization chambers. Right: 2 UNI-DOSE and MP3 control device for the ionization chambers operation. 37

Figure 13 The superposition of the depth dose profiles with different beam energies issues a so-called spread-out Bragg peak (SOBP), which covers the tumor volume in depth. 38

Figure 14 Array of 24 pin-point ionization chambers in a PMMA holder. 38

Figure 15 Comparison of the stopping power for carbon ions in water calculated with classical and modified Bethe-Bloch formula with data from ICRU-73 [ICRU05]. 45

Figure 16 Comparison of the stopping power for carbon ions in cortical bone calculated with classical and modified Bethe-Bloch formula with data from ICRU-73 [ICRU05]. 46

Figure 17 Comparison of the SHIELD-HIT calculations with measurements performed at GSI [Sihver98] for the distribution of energy deposition (normalized to the entrance dose value) as a function of depth in water. The measurements and simulations were

done for a water phantom, irradiated with a carbon beam with initial energies of 270MeV/u and 330MeV/u. 47

Figure 18 Comparison of the SHIELD-HIT calculations with measurements at GSI and RIKEN [Sihver98] for the distribution of energy deposition (normalized to the entrance dose value) as a function of depth in water. The measurements and simulations were done for a water phantom, irradiated with a carbon beam with initial energies of 135MeV/u and 195MeV/u. 48

Figure 19 Comparison of the depth dose depositions from carbon beam with three different energies of 195, 270 and 330Mev/u measured at GSI and calculated with SHIELD-HIT v2. 49

Figure 20 Bragg curve for a ^{3}He beam with the energy of 168MeV/u measured at GSI and compared with SHIELD-HIT v2 simulations. 49

Figure 21 Distribution of the dose deposition from ^{4}He of 150MeV/u measured at HIMAC [Mastufuji03] compared with SHIELD-HIT v2 calculations. 50

Figure 22 Comparison of the depth dose deposition from ^{18}O measured at GSI [Sihver98] with SHIELD-HIT v2 calculations 50

Figure 23 Top: Fluence of primary (Z=6) and light fragments (Z=1, 2) relative to the incident particle fluence, N_0, as a function of depth in water produced by an incident carbon beam of 290Mev/u. Bottom: Fluence of intermediate fragments (Z=3-5).The experimental data from HIMAC [Matsufuji03] are compared with the calculations from SHIELD-HIT v2 and YIELD. 52

Figure 24 Attenuation in water for beams of ^{12}C, ^{14}N and ^{16}O with an initial energy of about 670MeV/u. Measured data [Schall96] are compared to those calculated with SHIELD-HIT v1 and SHIELD-HIT v2. 53

Figure 25 Comparison between calculated data from SHIELD-HIT v2 and Geant4 [Wilkens06] obtained for the carbon beam of 240MeV/u in water. 55

Figure 26 Contribution to the total dose deposition from secondary particles. Calculation was done for the carbon beam energy of 240MeV/u in water by SHIELD-HIT v2 and Geant4. 56

Figure 27 Fluence of primary (Z=6) and light fragments (Z=1, 2) relative to the incident particle fluence as a function of depth in water produced by an incident carbon beam of 240Mev/u. 56

Figure 28 Fluence of intermediate fragments (Z=3-5) relative to the incident particle fluence as a function of depth in water produced by an incident carbon beam of 290Mev/u.... 57

Figure 29 Fluence differential in energy of light fragments (neutrons and protons) for ^{12}C with initial energy of 200MeV/u after passing 12.78 cm of a water phantom. The angular distribution of secondary particles was measured at GSI [Gunzert04] (circles) and is compared with SHIELD-HIT v2 (solid line) and SHIELD-HIT v1 (long dash line) calculations. 58

Figure 30 Fluence differential in energy of light fragments (deuterons, tritons and He ions) for ^{12}C with initial energy of 200MeV/u after passing 12.78 cm of a water phantom. The angular distribution of secondary particles was measured at GSI [Gunzert04] (circles) and is compared with SHIELD-HIT v2 (solid line) and SHIELD-HIT v1 (long dash line) calculations. 59

Figure 31 Lateral profiles of a scanning beam in plateau region. Measured spread-out peak from carbon beam is compared with calculations done with SHIELD-HIT v2 and TRiP BEAM. 60

Figure 32 Lateral profiles of the scanning beam in Bragg peak region. Measured spread-out peak from carbon beam is compared with calculations done with SHIELD-HIT v2 and TRiP BEAM. 61

Figure 33 Lateral profiles of the scanning beam in fragments tail region. Measured spread-out peak from a carbon beam is compared with calculations done with SHIELD-HIT v2 and TRiP BEAM. 61

Figure 34 Contribution of carbon ions and secondary particles to the total dose deposition in the plateau region. The lateral profiles of the carbon beam in water are calculated with SHIELD-HIT v2. 63

Figure 35 Contribution of carbon ions and secondary particles to the total dose deposition in the Bragg peak region. The lateral profiles of the carbon beam in water are calculated with SHIELD-HIT v2. 64

Figure 36 Contribution of carbon ions and secondary particles to the total dose deposition in the fragments' tail region. The lateral profiles of the carbon beam in water are calculated with SHIELD-HIT v2. 65

Figure 37 Comparison of a spread-out Bragg peak measured at GSI with calculations done by SHIELD-HIT v2 and TRiP BEAM [Krämer06]. 66

Figure 38 Ratio of stopping power values from different sources to those from ICRU-73 [ICRU05] for carbon in water, as a function of the energy. The dotted line is for MSTAR [Paul02] data; dashed lines are for SHIELD-HIT v1 (long dash) and v2 (short dash) using the original and the modified Bethe-Bloch formula respectively. 67

Figure 39 Monte Carlo calculated values of the water/air stopping power ratio for a carbon beam as a function of the depth in water for carbon beams with initial energies between 50MeV/u and 450MeV/u. The solid line at 1.130 corresponds to the constant $s_{w,air}$ value recommended by IAEA TRS-398. 68

Figure 40 Deviation of $s_{w,air}$ for the produced fragments from the value for ^{12}C alone with initial energy of 450MeV/u. 69

Figure 41 Comparison of the stopping power ratio calculated just for primary ^{12}C ions with a calculation for the whole spectrum of primary and secondary particles. The calculation is done with SHIELD-HIT v2. 69

Figure 42 Peak position of the stopping power ratio (blue solid line) relative to the position of the Bragg peak of corresponding primary energy of 450MeV/u (red solid line). 70

Figure 43 Ratio of the stopping powers water to air from ICRU-49 [ICRU93] for protons and alpha particles and ICRU-73 for heavier ions [ICRU05]. 70

Figure 44 Monte Carlo calculated values of the water/air stopping power ratio for different ion beams as a function of the depth in water. The solid line at 1.130 corresponds to the constant $s_{w,air}$ value recommended by IAEA TRS-398. 72

Figure 45 Comparison of Monte Carlo calculated stopping power ratios for ^{3}He and ^{4}He. . 73

Figure 46 The ratio of the stopping powers water to air for carbon ions using different data for stopping powers versus the adopted constant proposed by TRS-398 [IAEA00]..... 74

Figure 47 The stopping power ratio for ^{12}C of 400MeV/u calculated with SHIELD-HIT v2 using different *I*-values in stopping power data from BEST. The stopping power ratios calculated for the primary particles only (solid line) are compared with those calculated for the whole spectrum (dotted line) and TRS-398 adopted constant. 75

Figure 48 Contribution of the fragments to the stopping power ratio calculated with SHIELD-HIT v2 for a primary ^{12}C beam of 300MeV/u. 75

Figure 49 Depth dose deposition from the antiprotons of 47MeV in polystyrene cylinder measured with Alanine detectors and calculated with SHIELD-HIT v2. 77

Figure 50 Depth dose deposition from the antiprotons of 47MeV in polystyrene cylinder measured with TLD700 and TLD600 and calculated with SHIELD-HIT v2. 78

Figure 51 Comparison of the depth dose deposition in air of carbon ions with an energy of 20MeV/n calculated with different versions of the SHIELD-HIT code. 79

Figure 52 The stopping power ratio and *F-factor* calculated with SHIELD-HIT v2 for a Roos chamber irradiated with carbon beam of 300MeV/u with different calculation statistics. 80

Figure 53 Comparison of the physical and biological doses of carbon beam with energy of 270MeV/u calculated with SHIELD-HIT v2 and TRiP BEAM..... 92

Figure 54..... 101

Figure 55..... 103

List of Tables

Table 1 Overview over the planned centers for radiation therapy with light ions..... 1

Table 2 List of the initial energies and corresponding number of primary particles, obtained from the optimization procedure for homogeneous irradiation of cubic volume with a length of 2.5cm situated in 19-21.5cm water depth (so-called CUB113). 41

Table 3 Calculation of energy deposition from a carbon beam of 4692 MeV (391MeV/u) in a cylindrical water phantom (20x30 cm). The first two columns show the energy, deposited inside the phantom and the last three give the number per primary projectile and the energy, deposited outside the cylinder. Last row is the sum of the every column. 54

Table 4 *I*-values for water and air, obtained from the values for constitutes (see equation (2.3.2.4)), from different sources. 74

1 Introduction

The physical and biological properties of light ions (i.e. ions heavier than protons) make them very suitable for radiation therapy. An inverted dose profile with a sharp dose fall-off at the end of the particle range and negligible lateral scattering provide an accurate dose deposition to the volume of interest and spare the healthy tissue around. Moreover, the increase of ionization density at the end of the range (so-called Bragg peak) increases the biological effectiveness for ions like carbon. Hence, compared to photons or electrons, the use of light ions offers an advantage in treating of deep-seated tumors.

In radiation therapy light ions have been applied since 1957, when first studies were made in Berkeley, USA. Until today they attract a lot of interest with promising prospects for the future [Cas95]. Up to now more than 4500 patients have been treated with ions. Presently, there are three centers world wide offering medical application of light ion beams [Tsu94, Kraft98]. Five additional centers are in the planning phase (see Table 1).

Table 1 Overview over the planned centers for radiation therapy with light ions.

INSTITUTION	COUNTRY	TYPE	PLANNED START
Heidelberg	Germany	p, ion	2007
CNAO, Pavia	Italy	p, C-ion	2007
Med-AUSTRON	Austria	p, ion	2009
IMP, Lanzhou	PR China	C-Ar ion	?
ETOILE	FRANCE	p, C-ion	?

The interest in ion therapy led to considerable effort in improving the dosimetry of light ions in the last few years. In comparison with well established photon, electron and even proton dosimetry standards, the application of light ions suffers from the lack of standard laboratories that could supply reference beams or data for clinical applications.

Since the depth dose curve has a well-defined maximum and a steep fall-off, a small variation in the position of the Bragg peak results in significant changes in the local tumour control and unwanted complications. Hence, there is a great need to improve the accuracy of dosimetrical parameters for radiation therapy with light ions. For photons, electrons and protons in recent years a considerable amount of work has been invested to improve the accuracy of determining the absorbed dose in water [Andreo90, Andreo86].

The first dosimetry protocol that gave recommendations for the dosimetry of light charged particles in general was formulated by the American Association of Physicists in Medicine [AAPM86]. The charge collected by an ionization chamber was converted to dose, absorbed in the chamber wall with a conversion factor C_p with its main uncertainty arising from that of the so-called W-value (5-10%).

The experience in carbon ion dosimetry [Hartm99] was used by the International Atomic Energy Agency to issue a new formalism for clinical light ion-beam dosimetry: the Technical Reports Series 398 (TRS-398) [IAEA00]. As there is currently no primary standardization laboratory for light ion beams, it is recommended by TRS-398 to use a calculated beam quality correction factor k_Q for the derivation of the absorbed dose to water for an ion beam of arbitrary beam quality, where the measurements are carried out with an ionization chamber, calibrated in a beam of reference quality. The relative standard uncertainty of the calculated k_Q for carbon beam was estimated to be 2.8% for cylindrical chambers and 3.2% for plane-parallel chambers (as compared to 2% for protons) [IAEA00]. The largest contribution to this uncertainty arises from the stopping power ratio water-to-air that is estimated to be 2% (as compared to about 1% for protons). In contrast, in conventional radiotherapy the combined standard uncertainty of k_Q is estimated to be 1%. This comparison illustrates the importance of improvements in ion dosimetry and especially in the knowledge of stopping power ratios.

One widespread method that is used today in dosimetry is the Monte Carlo technique. By simulating the transport of particles in matter, one gets information about the spectra of primary and secondary particles and the deposited dose in every defined geometrical zone, which can be used for further calculations of correction factors or physical quantities. Nowadays, such calculated parameters are widely used in the clinical application of proton therapy. The aim of this work is the calculation of accurate water-to-air stopping power ratios for the ionization chamber dosimetry of carbon ions in the energy range of 50-450 MeV/u which is typical for radiotherapy. Another aim is the investigation of the influence of secondary particles generated by nuclear interactions of the primary carbon ions and of the ionization potential on the total dose deposition. Moreover, the calculation of stopping power ratios for other ions (from Li up to O) that are of interest for particle therapy is performed. For these tasks the Monte Carlo code SHIELD-HIT v2 was used, which has been significantly improved implementing substantial modifications to its predecessor SHIELD-HIT v1 [Gudow04].

2 Materials and Methods

The following chapter is divided into four main parts. The basics of dosimetry, practical aspects and dosimetry recommendations for heavy ion beams are presented in the "Dosimetry" subchapters. The principle of modeling of nuclear reactions with the Monte Carlo technique, history of SHIELD development and its modifications within the present work are given in the "Monte Carlo" subchapters. The measurements performed at GSI for the verification of the new code version SHIELD-HIT v2 are described in the "Measurement" subchapter. Finally, the simulations, made with SHIELD-HIT v2 for the code validation and calculations of the stopping power ratios are described in the last subchapter "Simulations".

2.1 Dosimetry: Basics

2.1.1 Definition of absorbed dose

During the penetration of a given volume of matter by an ionizing particle, a certain amount of energy ε will be deposited in the considered volume. The value of ε is a result of basic interaction processes, each contributing with an elementary amount of energy $\delta\varepsilon$ [Carls85]. The deposited energy $\delta\varepsilon$ is defined by following equation:

$$\delta\varepsilon = \mathrm{T} - \sum_n \mathrm{T}_n + \Lambda \,. \qquad (2.1.1.1)$$

Here T is the kinetic energy of the primary particle before the interaction with the target atoms, $\sum_n \mathrm{T}_n$ is the sum of kinetic energies of all secondary ionizing particles created during the interaction and leaving the volume (including the primary particle, if still able to ionize); Λ is the rest-mass energy released by transformations of nuclei and elementary particles.

The total energy ε imparted in a volume V therefore is presented by a sum of all elementary energies $\delta\varepsilon$ deposited from all processes in the considered volume:

$$\varepsilon = \sum_n \delta\varepsilon_n \qquad (2.1.1.2)$$

ε is a stochastic quantity, because the interaction processes have a stochastic nature. In order to avoid the variation in the definition of the deposited energy the energy deposited in an infinitesimal volume is expressed my means of its expectation value $\bar{\varepsilon}$. If the volume V approaches zero, also the value of $\bar{\varepsilon}$ tends to zero and it can be mathematically shown

that their ratio $\frac{\bar{\varepsilon}}{V}$ approaches a finite value. According to these definitions, the absorbed dose is introduced by:

$$D = \lim_{V \to 0} \frac{1}{\rho} \frac{\bar{\varepsilon}}{V} = \lim_{m \to 0} \frac{\bar{\varepsilon}}{m} \tag{2.1.1.3}$$

where m is the mass of medium contained in the volume V. Hence, the absorbed dose is the energy deposited per unit mass of an infinitesimal volume. The unit of absorbed dose is Joule per kilogram (J/kg). The technical name for this unit is Gray (Gy).

If the primary particle leaves the considered volume V and secondary particles are absorbed locally, the absorbed dose to the medium D_{med} is related to the particle fluence Φ_{med} as follows:

$$D_{med} = \Phi_{med} \left(\frac{S}{\rho} \right)_{med} \tag{2.1.1.4}$$

here, $(S/\rho)_{med}$ is the mass stopping power of particles in a medium at the energy E.

Equation (2.1.1.4) is valid for the ideal case of a monoenergetic beam. In reality accelerators deliver the beam already with some energy spread and additionally the effect of energy straggling occurs in the medium. This means that the particle fluence Φ_{med} in the medium is differential in energy E, $\Phi_{med,E}$. For the case of photon or electron beams the ionizing particles are electrons. Using heavy ion beams one has to consider the production of fragmented nuclei with different ion charge. This means that for the calculation of the absorbed dose in medium, D_{med}, the whole spectrum of primary and secondary particles has to be taken into account $\Phi_{med,E,i}$. Considering these statements, the absorbed dose in medium is given by the following expression:

$$D_{med} = \sum_i \int_0^\infty \Phi_{med,E,i} (S(E)/\rho)_{med,i} \, dE \, . \tag{2.1.1.5}$$

Here $(S(E)/\rho)_{med,i}$ is the mass stopping power at energy E for different ions i in the chosen medium.

2.1.2 Measurement of absorbed dose

The aim of clinical radiation dosimetry is the precise measurement of the absorbed dose or dose rate[1] at all points of interest in the irradiated tissue of the patient's body. For this goal dosimeters have been established that deal with the measurement of the absorbed dose or dose rate resulting from the interaction of ionizing radiation with matter.

A radiation dosimeter provides a reading M that is a measure of the absorbed dose D_{cav} deposited in its sensitive volume *V* by ionizing radiation (See Fig.1).

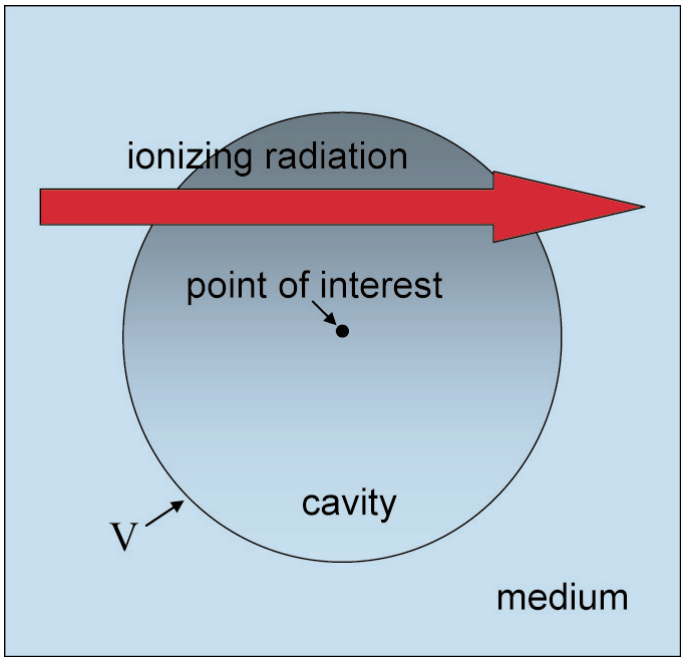

Figure 1 Schematic view of a dosimeter as a sensitive volume *V* (cavity), surrounded by medium

If the sensitive volume (cavity[2]) is relatively large and the dose within V is not homogeneous, then M represents the mean value $\overline{D_{cav}}$. Ideally, the reading M is proportional to D_{cav} and each part of the volume V has equal influence on M. In practice this is not always achievable. Most dosimeters have some degree of nonlinearity of M versus D_{cav} over at least some part of their dose range. For instance, not all segments of a large scintillator may deliver light to the photomultiplier with equal efficiency or an ionization chamber may contain regions from which the ions are not completely collected.

[1] Dose rate is dose, deposited per unit time

[2] Cavity is a gas filled sensitive volume of a dosimeter

The absorbed dose in the cavity D_{cav} derived from the reading M must be converted to the corresponding dose in medium D_{med}, absorbed at the point of interest[3]. The interpretation of a dosimeter reading in terms of absorbed dose in medium D_{med} at the point of interest is the central problem in dosimetry. To overcome this problem, several important theories have been developed for electron beams. They can also be interpreted for heavy ion beams.

2.1.3 Cavity theory

Usually, the cavity of the dosimeter consists of a medium, which is not the same material as the medium in which it is embedded[4]. Cavity theory relates the absorbed dose in the dosimeter cavity (sensitive medium) to the absorbed dose in the surrounding medium containing the cavity. In relation to the range of secondary charged particles created in the cavity, the cavity size may be small, intermediate or large. Various cavity theories have been developed, which depend on the cavity size; for example, the Bragg-Gray and Spencer-Attix theories for small cavities and Burlin theory for intermediate size cavities.

Bragg-Gray theory

This theory, developed by Bragg and Gray was the first cavity theory to provide the relation between the absorbed dose in a dosimeter and the absorbed dose in the medium containing the dosimeter [Attix86]. There are two main conditions for the application of this theory.

The first condition relates to the fluence, described in equation (2.1.1.5). The electron fluence in the cavity should be the same as the electron fluence established in the surrounding medium. Hence, **the cavity must be small in comparison to the range of secondary electrons in it, so that its presence does not perturb the fluence of the electrons in the medium.** In reality, the presence of a cavity always causes some degree of fluence perturbation that requires correction.

The second condition is related to the difference between the particles that cross completely the cavity or stop there. **The absorbed dose in the cavity is deposited only by charged particles crossing it (crossers).** This implies that all secondary charged

[3] Point of interest is a chosen infinitesimal volume in media where one wants to know the absorbed dose.

[4] Water is the standard reference medium in dosimetry with photons, electrons, protons and heavy ions to define the absorbed dose. Air is usually used as a medium in the cavity filling of ionization chambers.

particles depositing the dose inside the cavity are produced outside and completely cross the cavity. It means no secondaries are produced or stop inside the cavity.

Following these two conditions, one can relate the dose measured by a dosimeter D_{cav} to the dose in medium at the point of interest by equation:

$$D_{med} = D_{cav} \cdot \frac{(S/\rho)_{med}}{(S/\rho)_{cav}} \qquad (2.1.3.1)$$

where (S/ρ) is the average unrestricted mass stopping power for the medium and cavity, respectively. The difference between the restricted and unrestricted stopping power is explained below.

Spencer-Attix theory

The Bragg-Gray theory does not take into account the production of secondary charged particles in the sensitive volume. The Spencer-Attix cavity theory is a more general formulation that takes into account the contribution of the crossers as well as the stoppers[5] to the absorbed dose [Spenc95]. Spencer and Attix extended the cavity theory of Bragg-Gray and took into account the finite range of secondary electrons. Therefore, they introduced the cut-off energy Δ, which is set equal to the energy of electrons whose range in the cavity material is equal to the cavity size. Those electrons with energy *E* greater than 2Δ are assumed to cross the cavity and for the $2\Delta > E > \Delta$ case it becomes possible for an electron to drop below Δ as a result of a collision with an atomic electron and to deposit the energy locally. The Spencer-Attix relation between the dose to the medium and the dose in cavity is given by:

$$D_{med} = D_{cav} \cdot s_{med,cav} \qquad (2.1.3.2)$$

Here $s_{med,cav}$ is a ratio of fluence-weighted average stopping powers, the so-called stopping power ratio. The full expression for the Spencer-Attix stopping power ratio is:

$$s_{w,air} = \frac{\int_{\Delta}^{E_{\max}} \left(\Phi_E\right)_{med} \left(L/\rho\right)_{\Delta,med} dE + \left(\Phi_E(\Delta)\right)_{med} \left(S(\Delta)/\rho\right)_{med} \Delta}{\int_{\Delta}^{E_{\max}} \left(\Phi_E\right)_{med} \left(L/\rho\right)_{\Delta,cav} dE + \left(\Phi_E(\Delta)\right)_{med} \left(S(\Delta)/\rho\right)_{cav} \Delta} \qquad (2.1.3.3)$$

[5] Stopper is a secondary charged particle that stops in the cavity of the dosimeter.

Here $(\Phi_E)_{med}$ is the distribution of the total electron fluence as a function of energy at the point of interest in medium and $(L/\rho)_\Delta$ is the restricted mass collision stopping power[6] in the medium or cavity. $(\Phi_E(\Delta))_{med}$ and $(S(\Delta)/\rho)$ are the total electron fluence differential in energy and the mass collision stopping power evaluated at energy $E = \Delta$, respectively. The product of these two quantities is the number N of electrons at Δ. When multiplied by the energy $E = \Delta$, it yields approximately the total energy deposited by the so-called track-ends. This is an important point, as the contribution by these "track-ends" to the total absorbed dose in the cavity for electrons accounts for six to eight percent [Nahum80].

The the stopping power ratio equation for the heavy ion dosimetry will be discussed in paragraph 2.3.1.

The given cavity theories are the theoretical basis of the ionization chamber dosimetry and applicable in the case of ideal ionization chambers that do not perturb the fluence of primary particles. In practice, there are some additional aspects like reference conditions or the beam quality that introduce additional correction factors into equation (2.1.3.2). Their detailed description will be outlined below. In the next chapter, a short overview of dosimeters that are relevant for heavy ion dosimetry today is given.

2.2 Dosimetry: Practical Aspects

The basic theoretical principles of the measurement of an absorbed dose are given in paragraph 2.1.2. It concerns mainly ionization chambers. In general, dosimeters should satisfy certain requirements, which are the following:

- Proportionality of the dosimeter reading to the absorbed dose
- Independency of the system response from the dose rate
- Independency of the system response from the radiation quality[7] and energy
- Determination of the dose in a point-like volume

Besides these requirements, it is advantageous if a dosimetrical device has a direct reading of the absorbed dose.

---

[6] Restricted mass collision stopping power is the mean energy loss that is smaller than some chosen cut-off energy Δ. More about stopping power is presented in paragraph 2.3.4.

[7] Beam quality is a characteristic of the ionizing properties of the primary particles. Photon, Electron and heavy ion beams cause different ionization density of the target.

There are many different kinds of dosimeters and methods of measurement in dosimetry. Unfortunately, none of them is ideal. The dose described in (2.1.1) may not always be proportional to the effect observed in a dosimeter. Beyond a certain dose range a non-linear behavior in the dosimeter response always appears. The range of linearity depends on the type of device and its physical characteristics.

A huge variety of different dosimeters exist today. They can be distinguished by different physical principles that are used for the absorbed dose measurements. A short description of the most important of them is presented below.

2.2.1 Calorimeters

Calorimetry is the measurement of the energy absorbed by a volume of matter by measuring the temperature rise in the volume. The measurement of the temperature rise in calorimetric dosimeters thus directly measures the energy imparted to matter by radiation. Only relatively small corrections for thermal leakage and for chemical reactions are necessary.

The temperature increase per unit of absorbed dose to the material in the sensitive volume of the calorimeter depends on its specific thermal capacity[8], which is usually expressed in $Jkg^{-1}K^{-1}$.

The quantity of heat produced in the calorimeter core is proportional to the absorbed energy. However, depending on the material used for the calorimeter, a certain amount of absorbed dose is always transferred to radiochemical reactions, requiring a correction to relate the measured temperature increase to the energy absorbed (the so-called caloric defect). For instance, for a water calorimeter the uncertainty raised from the caloric effect is evaluated to be 0.14%.

For a sensitive volume of a calorimeter, containing a material of thermal capacity h and caloric defect δ, the mean dose $\overline{D}$, absorbed in the calorimeter core is given by:

$$\overline{D} = \frac{\Delta T \cdot h}{(1-\delta)} \qquad (2.2.1.1)$$

Given these properties, calorimeters are presently used as a dosimetry standard in Secondary Standards Dosimetry Laboratories (SSDL). However, despite the very simple principle of calorimetric dosimetry, in practice the need for measuring extremely small

[8] Specific thermal or heat capacity is the ratio of the change in heat energy of a unit mass of a substance to the change in temperature of the substance; the heat capacity is a characteristic of a substance.

temperature differences makes the technique rather delicate [Bred95]. For instance, an absorbed dose of 7.52J/kg causes a temperature increase of 0.1K. Hence, this type of dosimeter is not often used in routine applications.

2.2.2 Photographic Films

Films play an important role in charged-particle beam alignment and conventional photon and electron dosimetry. They are used in various functions in diagnostic radiology, radiotherapy and radiation protection and can be used as a radiation detector, relative dosimeter and as display device. A photographic emulsion consists of microscopic grains of silver bromide (AgBr), dispersed in a gelatin layer on either one or both sides of a carrier medium. The radiation effect in such a film can be measured in terms of optical density (OD) with devices called densitometers. The OD is given by the equation

$$OD = \log_{10}(I_0 / I) \qquad (2.2.2.1)$$

where I_0 is the initial beam intensity and I is the intensity transmitted through the film. This type of dosimeter is a perfect tool for 2-dimensional beam homogeneity check which, in a single exposure, also provides information about the spatial distribution of radiation in the area of interest. However, the relationship between dose and *OD* is not always linear. Film emulsions show a linear response to the exposure to radiation in a limited dose range that depends on the type of emulsion. For the case of heavy charged particle dosimetry, the sharp increase of LET at the Bragg peak region causes a non-linear response of the film. The optical density decreases at very high LET regions due to a reversal of the process of formation of developable grains, called *solarization.* The interpretation of a given *OD* in terms of dose thus may require other information about the general dose level to be expected. The accuracy of the filmdosimetry with heavy ions is around 10% [Bath00].

2.2.3 Thermoluminescent Dosimeters

Some chemical mixtures retain a part of the absorbed dose energy in a metastable state of electron after the irradiation. This preserved energy can be released from the metastable state in the form of ultraviolet, visible or infrared light via stimulation with heat or light. This phenomenon is called luminescence. If heat is applied for the extraction of the reserved energy, the release process is known as thermoluminescence and the detector is called thermoluminescent dosimeter (TLD)[9]. The main characteristic of the TL material is its

[9] LiF:Mg,Ti is the most commonly used chemical formula for TLD material in medical applications because of its tissue equivalence.

intrinsic thermoluminescence efficiency, which is the ratio of the TL light emitted per unit mass to the absorbed dose.

To the advantages of TL dosimeters contribute its compact size, passive energy storage capabilities and the suitability for *in vivo* dosimetry direct on patients, without disturbing the primary fluence. The thermoluminescence intensity emission is a function of the TLD temperature *°C* during heating. The resulting curve is called the TLD glow curve (see Fig.2).

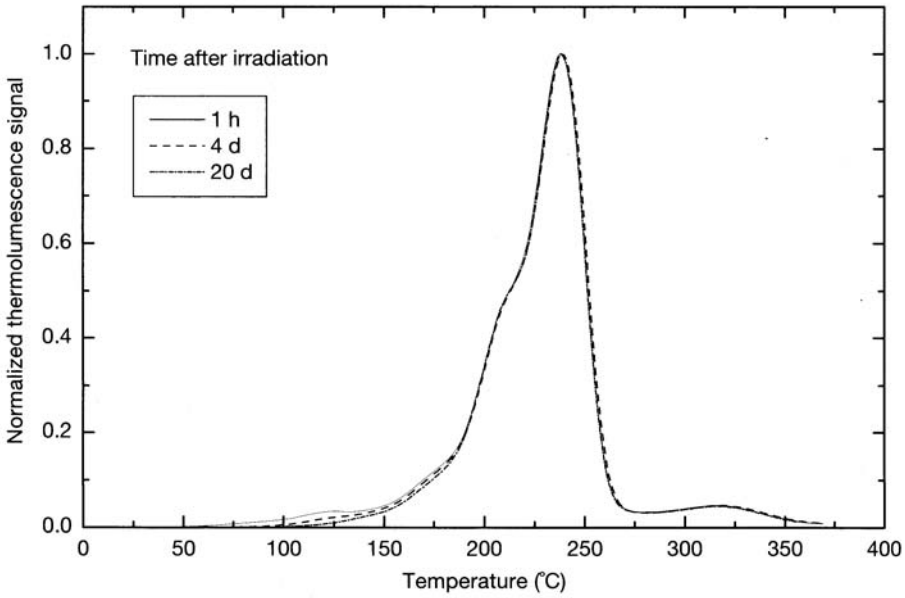

Figure 2 A typical thermogram (glow curve) of LiF:Mg,Ti measured with a TLD reader at a low heating rate.

The main dosimetric peak of the glow curve between 180°C and 260°C is used for dosimetry, and is not affected by room temperature. The total thermoluminescence signal received from the TLD can be correlated to the delivered dose through proper calibration. The dose response is linear over a wide range of doses relevant in radiotherapy. For electron and photon beams a precision of 3% in dose measurements with a TLD can be achieved. However, for high LET regions in heavy charged particle beams a nonlinear behavior appears [Geiss97]. Hence, the dependence of the TLD response on the particle type and energy make them unsuitable for the absorbed dose measurements in heavy ion therapy. Nevertheless, knowing the efficiency of material for every type of fragments and energy, dose-verifications can be done. For this purpose a model to calculate the TLD efficiency for heavy ion beams was developed at the Gesellschaft für Schwerionenforschung (GSI), Darmstadt [Geiss97]. (The model convolutes the TLD response to X-ray irradiation with the track structure of the heavy ions using the calculated particle spectra differential in energy $dN(E, Z, r)$). If the applied dose is known, it is possible to calculate the expected TL signals and compare it with the measurements.

An example of measured and calculated results for dose verification is given in Fig.3.

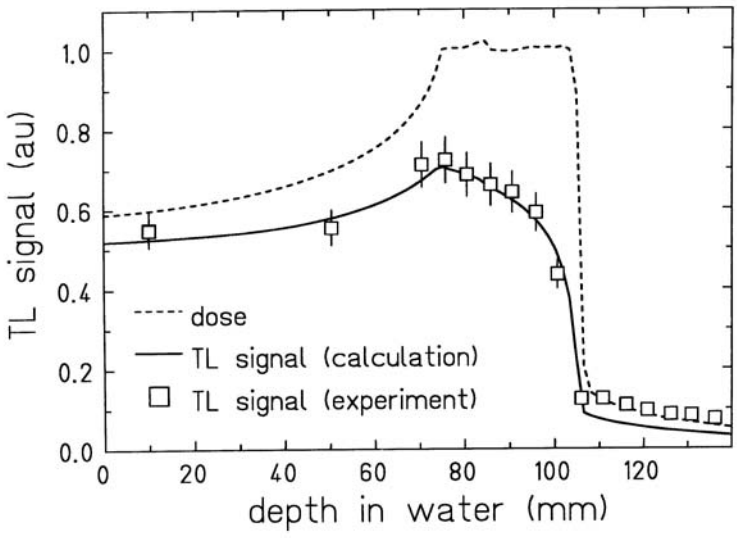

Figure 3 TL response of a TLD-700 for a spherical volume with a homogeneous dose deposition of 1Gy [Geiss97]. The dotted line shows the absorbed dose.

2.2.4 Ionization chambers

The most widely used type of dosimeters is the air filled ionization chamber. Ionization chambers give an output from the collection of the charge created by crossing ionizing radiation in a sensitive volume.

Principle

An ionization chamber is basically a gas filled cavity surrounded by a conductive outer wall and having a central collecting electrode (see Fig.4).

A high quality insulator separates the wall and the collecting electrode and reduces the leakage current when a polarizing voltage is applied to the chamber.

The simplest schematic configuration is given in Fig.5. The gas volume is contained by a pair of electrodes that create an electric field in the gas by applying of an external voltage. When an ionizing radiation traverses the cavity it ionizes the gas molecules producing ion-electron pairs. The ions and electrons drift along the electric field towards the electrodes where they are collected.

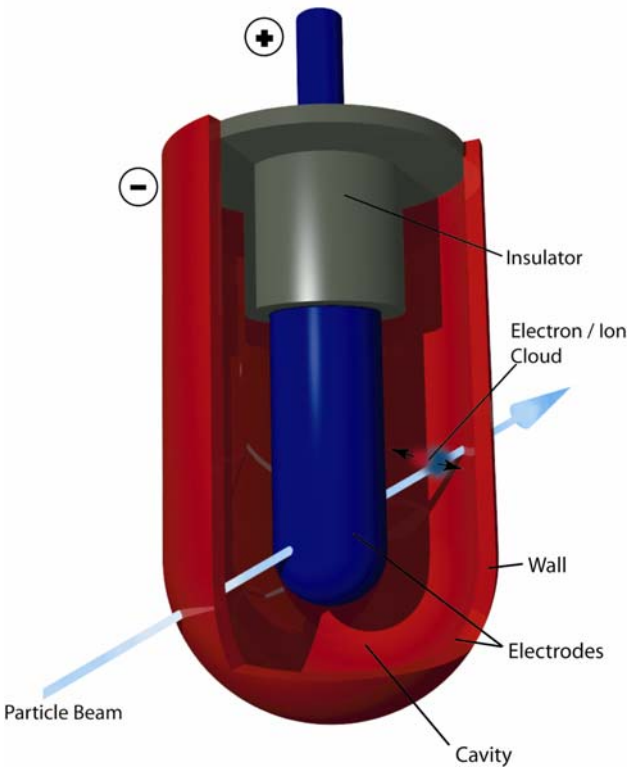

Figure 4 Schematic view of a cylindrical (thimble) ionization chamber

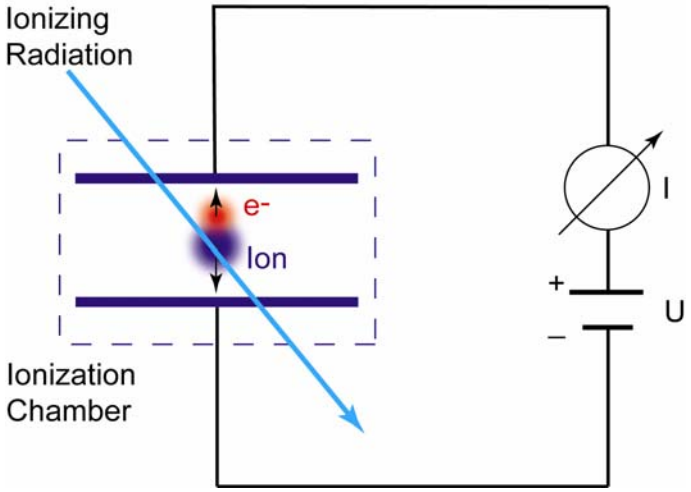

Figure 5 Schematic view of a plate parallel ionization chamber in a simple electrical circuit

The current-voltage characteristic is shown in Fig.6. In the absence of an external voltage there is no electric field created between the electrodes and the ions and electrons produced by the ionizing radiation in the gas disappear due to recombination. By increasing the voltage, the resulting electric field begins to separate the electron-ion pairs. The measured current thus increases with increasing voltage, approaching a flat plateau. This region, where a complete collection of the produced charge is achieved is called ion

saturation. Increasing the voltage the current will rise again due to the ionization gain of electrons in the gas.

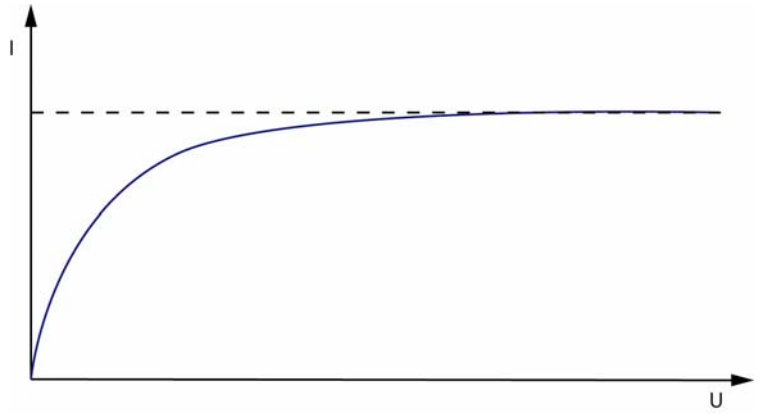

Figure 6 Sketch of the Current-Voltage characteristic of an ionization chamber shown in Fig.5

The charge collected by the ionization chamber is proportional to the number of ionization interactions per unit time that took place in the chamber cavity, each resulting in the creation of an electron-ion pair. The mean value of the energy, necessary to produce such a pair in the gas is called W-value. A more detailed description of this value is given below in paragraph 2.3.1. With the W-value as multiplication factor the collected charge (reading M of dosimeter) on the electrodes is directly proportional to the energy deposited in the gas and the dose can be calculated as follows:

$$D_{cav} = \frac{M}{m}\left(\frac{W_{cav}}{e}\right). \qquad (2.2.4.1)$$

Here M is the charge produced in the cavity, *e* is the electron charge and *m* is the mass of the gas in the cavity. For the determination of the absorbed dose in the cavity, M is measured and the e and W values are known (W_{cav}/e for air is 33.77 J/C). To define the mass m of the gas in the cavity a calibration of the ionization chamber is necessary. The procedure of the calibration is performed under reference conditions[10] usually using a reference beam of ^{60}Co.

Following the given prescriptions and performing the measurements under reference conditions with a calibrated ionization chamber one receives the absorbed dose in the chamber cavity. This is an ideal theoretical case. In practice several correction factors have to be taken into account.

[10] Reference conditions imply the environmental conditions: air temperature 22°C, humidity 50% and pressure 101.325 kPa.

Correction factors

As already mentioned above, one is not interested in knowing the dose absorbed in the chamber cavity, but primarily in the surrounding medium at the point of interest. In this case the Spencer-Attix cavity theory can be used to calculate the dose in the medium, as given by equation (2.1.3.2). Using this equation, it should be kept in mind that the theory treats the ionization chamber as an ideal dosimeter that does not perturb the primary particle fluence. Dealing with realistic ionization chambers that always perturb the primary fluence, a correction of the calculated dose in the medium is required. Therefore, the dose delivered in the medium at the point of interest by a reference beam of photons (^{60}Co), measured under reference conditions is given by:

$$D_{med} = \frac{M}{m} \cdot \left(\frac{W_{cav}}{e} \right) \cdot s_{med,cav} \cdot p = M \cdot N \,. \qquad (2.2.4.2)$$

Here p is a perturbation factor for the actual ionization chamber; N is the so-called calibration factor, which initially includes W_{cav}, $s_{med,cav}$ and p (see a more detailed description of these correction factors below in paragraph 2.3.1). The calibration factor is measured for every individual ionization chamber in a standard laboratory with a reference beam under reference conditions. Hence, the application of equation (2.2.4.2) has two limitations: a) the measurement should be done under reference conditions with a reference beam; b) the calibration factor for the ionization chamber is valid only for the reference conditions which apply to the calibration. The measurements are always influenced by some effects like atmospheric variation or chamber effects (perturbations).

For non-reference conditions, the reading M of the dosimeter must be corrected according to the following equation:

$$M_{ref} = M \cdot k \qquad (2.2.4.3)$$

where k is correction factor which consists of several influencing quantities:

$$k = k_{\rho} \cdot k_{P} \cdot k_{S} \,. \qquad (2.2.4.4)$$

Here k_{ρ} is the pressure, temperature and humidity correction to the ambient air, which corrects the mass of air in the cavity volume according to atmospheric variations; k_P is the polarity corrections, that is due to the use of polarizing potentials of opposite polarity. k_S is the recombination correction factor which corrects for incomplete charge collection due to ion recombination in the cavity volume. These factors must be taken into account for every measurement procedure under non-reference conditions.

Moreover, if the measurements are performed in the beam quality different from the reference beam quality of Co^{60}, as is the case for heavy ion beams, one more factor – the beam quality correction factor k_Q must be taken into account. A more detailed description of this parameter and its composition is given below in paragraph 2.3.1.

2.3 Dosimetry: Recommendation for heavy ion beams

Although light ions are used since 1957 for radiotherapy, no dosimetry recommendations have been published up to 1986. The first dosimetry protocol was issued by the American Association of Physicists in Medicine [AAPM86]. It lighted up some general principles for heavy particles dosimetry, but was not supported by comprehensive data for ionization chambers that may be used clinically. The use of Faraday cups or calorimeters was strongly recommended for the use in absolute dosimetry. Dosimeters like Faraday cups introduce two experimental uncertainties in the measurement: the area and the energy spread of the beam, which are very important for high accuracy results. Concerning the use of ionization chambers, protocols consider the W-value as a main source of uncertainty for the absorbed dose (the uncertainty of W-value is in the range of 5-10%). Still significant uncertainties arise as well from the stopping power ratio. AAPM provided data for those values in the plateau and peak region, independent of the type of projectile, energy of the incident ion beam and the spectral energy distribution.

In 2000 the International Atomic Energy Agency (IAEA) issued the Technical Report Series 398 (TRS-398): “International Code of Practice for Dosimetry Based on Standards of Absorbed Dose to Water” [IAEA00]. TRS-398 gives comprehensive information and recommendations for electron, photon, proton and ion beams. The main concept was based on the use of air-filled ionization chambers calibrated in terms of absorbed dose to water of a beam of Co^{60}. Although the specific recommendations for heavy ion dosimetry were also formulated, still the absence of a standard laboratory for heavy ion beams left open a lot of questions and hence a field for further research in definition of correction factors. In the two following subchapters the concept for the calculations of the correction factors given by TRS-398 and some modifications using a Monte Carlo technique are described.

2.3.1 $N_{D,w}$ based formalism

The determination of the absorbed dose to water in a reference beam of quality Q_0 according to IAEA TRS-398 is given by:

$$D_{w,Q_0} = M_{Q_0} \cdot N_{D,w,Q_0} . \qquad (2.3.1.1)$$

Here M_{Q_0} is the reading of a dosimeter corrected according to equation (2.2.4.3), determined in the same reference beam used for calibration in the standard laboratory. N_{D,w,Q_0} is a calibration factor of the dosimeter in terms of absorbed dose to water obtained from a standard laboratory using a reference beam. For the measurements with heavy ion beams one is confronted with a beam quality Q different from the reference Q_0 (Co^{60}). For this case the beam quality correction factor k_{Q,Q_0} is introduced into the above equation:

$$D_{w,Q} = M_Q \cdot N_{D,w,Q_0} \cdot k_{Q,Q_0}. \qquad (2.3.1.2)$$

This chamber-specific beam quality correction factor takes into account all differences between the reference beam quality Q_0 and the actual quality Q used in the measurement. Ideally, the beam quality correction factor k_{Q,Q_0} should be measured for each individual chamber at the same quality as the user beam. As there are still no primary standard laboratories for light ion beams, the dosimetry protocol IAEA TRS-398 relies on a theoretical determination of k_{Q,Q_0}. If the Bragg-Gray theory can be applied, the following expression for k_{Q,Q_0} can be derived [Andreo92]:

$$k_{Q,Q_0} = \frac{\left(s_{w,air}\right)_Q \cdot \left(W_{air}\right)_Q \cdot p_Q}{\left(s_{w,air}\right)_{Q_0} \cdot \left(W_{air}\right)_{Q_0} \cdot p_{Q_0}}. \qquad (2.3.1.3)$$

Here W_{air} is the energy required to produce one electron-ion pair in air, p_Q is the perturbation factor and $s_{w,air}$ is the Spencer-Attix water to air stopping power ratio. The factors in the denominator are well known for a reference beam of Co^{60}.The specific light ion beam correction factors are less well known. Here is the brief description of each of them.

A direct measurement of $\boldsymbol{W_{air}}$ value is very complex, as one has to measure accurately the number of ions produced and the total energy loss. This is typically done with a low energy beam stopping in the cavity. Another possibility is to use an absolute dosimeter like a calorimeter. Knowing the absolute dose in water, D_w, at the point of interest measured with a calorimeter, one measures the dose at the same position with the ionization chamber

calibrated in Co^{60} to get the corrected signal M_Q. The following formula describes the equation between these two measurements:

$$D_w = \frac{M_Q}{m} \cdot (W_{air})_Q \cdot (S_{w,air})_Q \cdot p_Q . \quad (2.3.1.4)$$

The mass m of the cavity gas of ionization chamber is determined from the calibration of the ionization chamber by:

$$\frac{1}{m} = \frac{N_{D,w}}{(S_{w,air})_{Q_0} \cdot p_{Q_0}} . \quad (2.3.1.5)$$

Thus, the equation for the experimental definition of W_{air} is given by:

$$(W_{air})_Q = \frac{D_w}{M_Q} \cdot \frac{1}{N_{D,w}} \cdot \frac{(s_{w,air})_{Q_0} \cdot (W_{air})_{Q_0} \cdot p_{Q_0}}{(s_{w,air})_Q \cdot p_Q} \quad (2.3.1.6)$$

Since there are only very few experimental data on W_{air} values, one can currently only rely on theoretical data. For mixed particle beams (primary particles and fragments) W_{air} can be obtained by averaging over the complete spectrum of primary particles and fragments at the reference depth:

$$(W_{air})_Q = \frac{\sum_i \int_0^\infty \Phi_{E,i} \cdot (S_i(E)/\rho)_{air} \, dE}{\sum_i \int_0^\infty \frac{\Phi_{E,i} \cdot (S_i(E)/\rho)_{air}}{w_i(E)/e} dE} \quad (2.3.1.7)$$

where $w_i(E)$ is the differential value of W_{air} at energy E for particle i. The calculation of W_{air} with such an approach requires the knowledge of $w_i(E)$ for every species of particles and their fluence from the whole energy spectrum.

Only a small number of measurements are available for the determination of W_{air} in heavy ion beams and until more information is available, the value W_{air} =34.50J/C and a standard uncertainty of 1.5% is recommended by TRS-398 for heavy ion beam dosimetry.

The factor $\boldsymbol{p_Q}$ describes the perturbation caused by an ionization chamber on the particle fluence. While an ideal Bragg-Gray detector does not influence the primary fluence, a realistic ionization chamber introduces some changes that have to be corrected for. The perturbation factor p_Q consists of several components:

$$p_Q = p_{cav} \cdot p_{dis} \cdot p_{wall} \cdot p_{cel} \qquad (2.3.1.8)$$

here p_{cav} is the cavity correction for the perturbation of the particle fluence due to scattering differences between the air cavity and the medium; p_{dis} is required for cylindrical (thimble) chambers and accounts for the effect of replacing a volume of water with the chamber cavity when the center of detector is taken as reference point; p_{wall} corrects the influence of detector wall and waterproofing material on ionization chamber response; p_{cel} corrects the effect of the central electrode that perturbs the detector response. Until now there is no information available on perturbation factors for heavy ion beams. The uncertainty of 1% is assumed according to the evaluation of Hartmann et al in [Hartm99]. However, there is a method to calculate this correction value theoretically. The detailed description is given in paragraph 2.3.3.

The value for $s_{w,air}$ for light ion beams in TRS-398 can be obtained as a fluence-weighted average ratio of stopping powers (henceforth referred to as 'stopping-power ratio', not to be confused with a direct ratio of stopping powers) over the complete spectrum of primary particles and secondary particles at the reference depth [IAEA00]:

$$s_{w,air} = \frac{\sum_i \int_0^\infty \Phi_{E,i} \cdot \left(S_i(E)/\rho\right)_w dE}{\sum_i \int_0^\infty \Phi_{E,i} \cdot \left(S_i(E)/\rho\right)_{Air} dE}. \qquad (2.3.1.9)$$

Here, $(S_i(E)/\rho)$ is the mass stopping power for a particle i with energy E in water or air and $\Phi_{E,i}$ is the particle fluence differential in energy, in water, for particles of type i.

Equation (2.3.1.9) was first introduced for electron beams by the National Council on Radiation Protection and Measurements (NCRP) according to the Bragg and Gray cavity theory within an arbitrary medium independent of the size of the cavity [NCRP27].

According to an analysis in TRS-398 on the values of W_{air}, p_Q and $s_{w,air}$, the biggest uncertainty (2%) originates from the stopping power ratio $s_{w,air}$ [IAEA00]. For the clinical application of carbon beams an adopted constant value of 1.13 is recommended for this factor.

In the present work the calculation of stopping power ratios for heavy ions was made using the Monte Carlo technique [Geithner06], according to a modified equation outlined below in 2.3.2.

2.3.2 Monte Carlo calculations of stopping power ratios for light ions

For a calculation with equation (2.3.1.9) the whole particle spectrum differential in energy down to 0 is required. One limitation is due to the fact that there is a lack of information on light ion physics at very low energies. Therefore, in a Monte Carlo approach it is easier and less time consuming to calculate the transport of particles down to certain cut-off energy $E = \Delta$ where the remaining particle range is negligible, and then to score their remaining energy as being deposited locally without transporting them. These particles below Δ are thus treated as "stoppers".

For the present work, the stopping power ratios for light ions were calculated using the following equation:

$$s_{w,air} = \frac{\sum_i \int_{E_i>\Delta}^{E_{\max}} \Phi_{E,i,w} \cdot \left(S_i(E)/\rho\right)_w dE + \sum_{i(E_i \le \Delta)} (E_i \cdot N_{i,w} / m_w)}{\sum_i \int_{E_i>\Delta}^{E_{\max}} \Phi_{E,i,w} \cdot \left(S_i(E)/\rho\right)_{air} dE + \sum_{i(E_i \le \Delta)} (E_i \cdot N_{i,w} / m_{air}) \cdot (S_i(\Delta)_{air} / S_i(\Delta)_w)} \quad (2.3.2.1)$$

Here the energy, deposited in water (numerator) and in the air (denominator) is divided in two parts coming from "crossers" (first term) and "stoppers" (second term).

Δ is the Monte Carlo transport cut off energy, E_i is the energy deposited by stoppers, $N_{i,w}$ is the number of stoppers in water, m is the mass of the water or air cavity. The sum of the energy E_i from all stoppers $N_{i,w}$, divided by the mass of water of a volume equal to the cavity of the ionization chamber, gives the dose deposited by "track-ends". In the denominator, the second term is the same energy, divided by the mass of air of the chamber cavity and multiplied by the ratio of stopping-powers air/water at that energy, which gives the dose from "track-ends" in air.

The value of the cut-off energy Δ is defined by the corresponding range of the particles, which is equal to the cavity size. In contrast to electrons light ions produce fragments. Hence, ideally, the value of the cut-off energy should be different for each ion species, because at the same energy different ions have different range. As an approximation, a single mean value for the cut-off energy of 25keV/u of the primary particles is used, whose choice is justified later on in paragraph 2.8.2.

When the spectrum of secondary electrons produced by light ions is considered, the vast majority of delta-electrons have a very low energy (around 100eV or less) [Krämer94]. Hence, their transport can be neglected for dosimetry purposes. Their energy deposition is assumed to be taken into account by the (non-restricted) electronic stopping power of ions, S/ρ, which circumvents the complication of using restricted ion stopping powers and further

transport of secondary electrons [ICRU93]. It should be noted that, in comparison with light ions, the stopping power of electrons is three orders of magnitude lower.

As one can see from equation (2.3.2.1), the uncertainty in the $s_{w,air}$-values for light ion beams depends on the spectra of primary particles and their fragments ($\Phi_{E,i}$), as well as on the stopping power values for all these particles ($S_i(E)$). In order to obtain these $\Phi_{E,i}$ values for the calculations, the Monte Carlo code SHIELD-HIT v2 was used, which is described in paragraphs 2.4 and 2.5.

2.3.3 Alternative approach

The classical approach of the $N_{D,w}$ based formalism discussed above defines every correction factor separately. For their calculation or measurement the absence of any correlations between them is assumed. Another method for the calculation of correction factors was proposed by Sempau and Andreo for electron beams [Medin04]. Instead of calculating all parameters separately, one can simulate a realistic ionization chamber in a water phantom (see Fig.7).

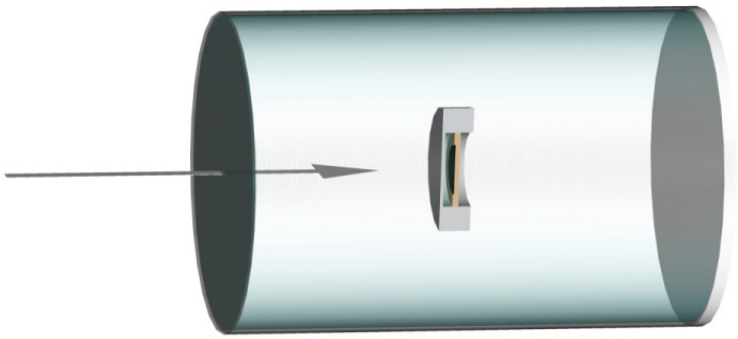

Figure 7 Schematic picture of a Roos chamber (cross-section) in a water phantom.

The Bragg-Gray theory assumes that the particle fluence in the sensitive volume of the detector is the same as the fluence in the undisturbed medium. To avoid this approximation, the stopping power ratio can be calculated in a Monte Carlo simulation together with the perturbation factor as a direct coefficient of proportionality between the dose in water D_w at the point of interest and the dose in air from the ionization chamber averaged over the gas cavity:

$$D_w = \overline{D_{air}} \cdot f_{c,Q} \,. \qquad (2.3.3.1)$$

In terms of the beam quality correction factor for the absorbed dose to water one obtains:

$$k_{Q,Q_0} = \frac{f_{c,Q}}{f_{c,Q_0}} \cdot \frac{w_Q}{w_{Q_0}} \qquad (2.3.3.2)$$

where $f_{c,Q}$ is a chamber- and quality-dependent factor that can be identified with the product of $(s_{w,air} \cdot p)$. Using modern Monte Carlo computer codes with detailed geometry description and including all relevant interactions one can calculate accurately both doses D_w and $\overline{D_{air}}$ and derive $f_{c,Q}$ directly.

2.3.4 Stopping Power: definition and main dependencies

The passage of charged particles through matter is mainly characterized by the energy transfer to the surrounding matter and the deviation from the particle's primary direction. Multiple Coulomb scattering processes cause the deviation of the projectiles and their fragments from the primary direction, which is not in the focus of the present work. Five groups classify the energy transfer or energy loss processes for charged particles:

- Collisions: electronic excitation and ionization of the target
- Elastic scattering from nuclei
- Electron capture
- Nuclear Reactions
- Electromagnetic radiation (Bremsstrahlung).

Depending on the type of projectile and its energy these processes influence the projectile's total energy loss in different ways. The dominating contribution to the stopping power of light charged particles over a very wide energy range is the excitation and ionization of target atoms (so called collision stopping power). These inelastic collisions with the atomic electrons of the material are well described by the Bethe-Bloch theory and its extensions [ICRU93], which treat the Coulomb interaction between the projectile and the target electrons in the first Bohr approximation. The resulting equation for the energy loss is:

$$-\frac{dE}{dx} = 0.307\rho\frac{Z}{A}\frac{z^2}{\beta^2}\left[L_0(\beta) + zL_1(\beta) + z^2L_2(\beta)\right] \qquad (2.3.4.1)$$

Equation (2.4.3.1) is commonly known as the Bethe-Bloch formula. Here L_0 is given by

$$L_0(\beta) = \frac{1}{2}\ln\frac{2m_ec^2\beta^2W_{\max}}{1-\beta^2} - \beta^2 - \ln I - \frac{C}{Z} - \frac{\delta}{2} \quad \text{with}$$

m_e: Electron mass

$\frac{Z}{A}$: Atomic number and atomic mass of the target. For a target with *i* components this ratio is obtained as $\frac{Z}{A} = \sum_i w_i \frac{Z_i}{A_i}$ according to Bragg rule, where w_i is a fraction by weight.

ρ*:* target density

z*:* charge of the projectile

$\beta = v/c$ of the incident particle

I: ionization potential of the target

$W_{\max}$*:* maximum energy transfer in a single collision

$L_1(\beta)$*:* Barkas correction (negligible at high energies)

$L_2(\beta)$: Bloch correction (negligible at high energies)

C*:* shell correction (negligible at high energies)

δ: density correction (negligible at low energies)

Shell and density corrections are relevant only for very high and low energies, respectively. The resulting stopping power is proportional to the square of the projectile charge z^2. The mean excitation potential, I-value*,* is another essential parameter of the Bethe-Bloch formula. The value of I is independent of the projectile's properties and depends only on the properties of the medium. The mean excitation potential is theoretically a logarithmic average of the orbital frequency ν weighted by the so-called oscillator strengths of the atomic levels. In practice this is a quantity very difficult to calculate since the oscillator strengths are not known for most materials. Hence, the most frequently applied method of obtaining I-values is to extract them from measured stopping powers values using the Bethe-Bloch formula (2.3.4.1). This method has the significant disadvantage that the shell corrections and Barkas corrections are usually not known independently of each other with the desired precision and must be evaluated together with the mean excitation potential. This problem is irrelevant only at very high energies where the shell and Barkas corrections are negligible.

Experimental data on I for mixtures or compound materials are often missing. Hence, a simple alternative is to use Bragg's additivity rule [Bragg05]. According to this rule, the relation for the mean excitation energy can be derived from the atomic constituents:

$$\ln I = \frac{\left[\sum_i w_i (Z_i / A_i) \ln I_i\right]}{\sum_i w_i (Z_i / A_i)} \qquad (2.3.4.2)$$

The accuracy of the calculation can be improved by applying the additivity rule not to constituent atoms, but to molecular fragments. A theoretical approach for the modified I-values in different chemical environments was developed by Oddershede and Sabin [Odder89].

It was shown in the ICRU Report 37 [ICRU84] that in most cases the differences between the experimental I-values and the corresponding I-values from the additivity rule are smaller than the uncertainties of the experimental values.

For the last forty years a number of data sets with recommended I-values were published. The ICRU-37 report issued the estimation of I-values for all elements based on the analyses of measured stopping power values for protons, deuterons and alpha particles [ICRU84]. These data were retained in a more recent ICRU Report 49 [ICRU93]. The most recent publication on ionization potentials was issued in 2005 by IAEA in the ICRU Report 73 [ICRU73] where the latest knowledge and experimental database was applied.

The precise value of the ionization potential is of great importance for heavy ion dosimetry. The position of the Bragg peak depends strongly on the I-value. For instance, for a carbon ion beam of 400MeV/u in water a deviation of the I-value by 5 eV results in a peak shift of approximately 2mm [Paul06B].

Concerning the stopping power ratio water-to-air for primary particles the mean ionization potential becomes the main source of uncertainty. As an approximation, the stopping power ratio for primary particles can be calculated as a ratio of stopping powers for water and air. As it was shown by Paul [Paul06A], the ratio is directly dependent on the I-value for water and air:

$$S_{w,air}^{prim} = \frac{(Z/A)_{water}}{(Z/A)_{air}} \frac{\ln(2m_e v^2 / I_{water})}{\ln(2m_e v^2 / I_{air})} = \frac{0.5551}{0.4992} \frac{\ln(2m_e v^2 / I_{water})}{\ln(2m_e v^2 / I_{air})} \qquad (2.3.4.3)$$

where (Z/A) for water and air is calculated from Bragg's additivity rule.

Another important constituent of the stopping power ratio calculation is the spectrum of the primary and secondary particles differential in energy. These data were derived from the Monte Carlo simulation as described below

2.4 Monte Carlo: Technique

The so-called Monte Carlo technique is used in computational algorithms for simulating the behavior of various physical and mathematical systems. The simulation is based on random numbers, which are chosen by statistically sampling the probability distributions of the physical quantities characterizing the interaction event of ions with target atoms. After propagating many ions (multiple “trials” or ”histories”), the desired result is taken as an average over the number of observations.

The name “Monte Carlo” originates from the city Monte Carlo (Monaco) that is famous for its casinos, where the roulette serves as a simple generator of random numbers. For the first time this method was officially described in 1949 by Metropolis and Ulam [Metrop49]. One should emphasize that the theoretical basics of the Monte Carlo method were developed considerably earlier. However, before computers were generally available, the Monte Carlo technique could not become a universal numerical method, because the manual calculation of random numbers is a tedius process.

2.4.1 Modeling of nuclear reactions

Modern computer technology provides the advantage to do different mathematical calculations at any level of complexity and to simulate various physical processes in a reasonably short time. The progress in this field gave a powerful incentive for the development of computer codes based on the Monte Carlo method for hadron transport processes, which have been successfully applied to many fields like radiation effects on spacecrafts, shielding, accelerator physics and radiotherapy.

All hadron transport codes presently existing can be divided into two main groups according to the approach used for the modeling of nuclear reaction: exclusive and inclusive [Byckl75].

Exclusive approach

The exclusive approach treats the nuclear reaction between two nuclei A_1 and A_2 (see Fig.8) in the following way: all possible products $B_1 \ldots B_n$ considering all possible channels of such reaction are registered.

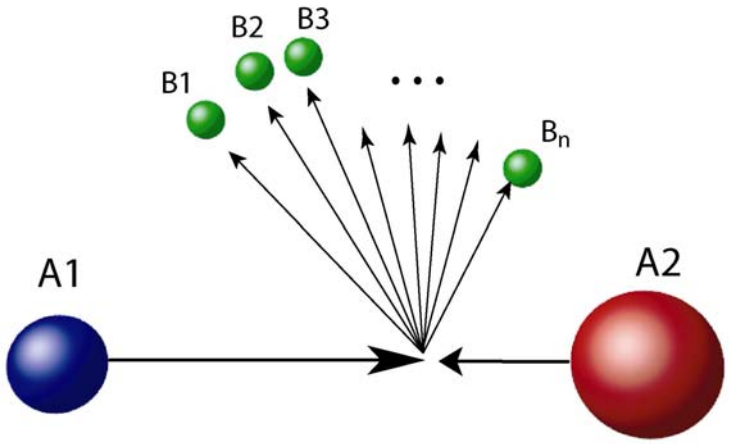

Figure 8 Schematic view of nuclear reaction in exclusive approach.

The reaction equation describing this concept is given by:

$$A_1 + A_2 \rightarrow B_1 + B_2 + ... + B_n \qquad (2.4.1.1)$$

The exclusive approach is based on a many-particle distribution of secondaries for the description of a hadron-nucleus (hA) interaction. It implies the calculation of all individual characteristics of each hA interaction, i.e. of energy and direction of each secondary particle as well as individual variables of residual nucleus. It provides energy-momentum conservation laws in each event, takes into account channels with different number of secondary particles *n* and allows to consider any correlation between reaction products.

Inclusive approach

The inclusive approach follows only one reaction product B_1, while the remaining fraction of all unidentified products is represented just by X (see Fig.9)

On the contrary, in an inclusive approach the single-particle distributions of secondary particles are used for the description of hA interactions. Evidently an essential convolution of information occurs, because a many-particle distribution of secondary particles is being integrated over all secondary variables excluding a single particle. It provides energy-momentum conservation laws on the average only. Different channels of the reaction are summarized and any correlations between reaction products are lost.

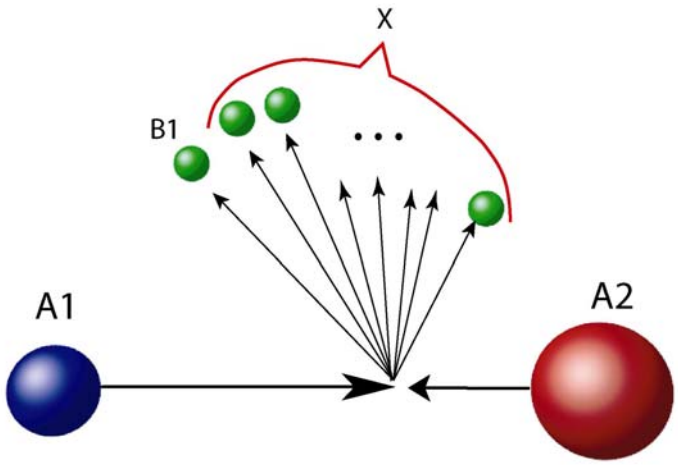

Figure 9 Schematic view of nuclear reaction in inclusive approach.

2.4.2 Monte Carlo hadron transport codes

First successful trials to develop a nucleon transport code were done in the mid-1960ies. Two programs were developed independently at virtually the same time: the NTC (Nucleon Transport Code) [Kinn64] and a code designed by Barashenkov and Toneev [Barash1973]. Both codes were based on cascade evaporation models (CEM)[11] which were available at that time and allowed to simulate the transport of nucleons up to 500MeV. These simulations could only be done in very simple geometries and with restricted chemical composition.

These first steps were immediately followed by further developments, NMTC (Nucleon-Meson Transport Code) [Colem71] and SHIELD [Sobol70]. The new code HETC (High Energy Transport Code) included NMTC and a special extrapolation procedure for extending the applicable energy range [Armstr72].

The SHIELD and HETC codes included different physical models, but both modeled the nucleon-π-meson cascade in the target with energies up to 30 GeV and yielded similar results. The code SHIELD used a Cascade Model developed in Dubna [Barash72, Barash73]. The transport of neutrons with energies lower then 10.5MeV was done using the neutron database БНАБ [Abag64]. The HETC code was based on the intranuclear cascade

[11] The cascade evaporation model is based on the assumption that the nuclear collision can be described simply as the superposition of nucleon-nucleon interactions. In the simplest version of the CEM, the nucleons are assumed to travel in straight trajectories between any two collisions.

model of Bertini [Betrini69] and the evaporation model of Dresner [Dresner61]. For the transport of low-energetic neutrons the program 05R, developed by Irving, was used [Irving65]. The program 05R became later the foundation for the well known neutron transport code MORSE [MORSE83]. The main similarity of the SHIELD and HETC was the exclusive approach for nuclear reaction modeling. Later on these codes were distributed over the scientific centers and depending on the physical task under investigation, certain parts of the codes were improved and new versions appeared. The following chapter describes the developments and improvements applied to the original code SHIELD and the features of the new versions (see Fig.10).

Further information about other hadron codes existing today is given in Appendix A.

Development of SHIELD; SHIELD-HIT v1

As already mentioned, the first version of the code SHIELD was developed in the late sixties [Sobol70]. Although the program preserved its name until today, it went through a number of mayor changes and improvements. The modern version is a completely new code in comparison with the first original version. The first version was rewritten in 1989-90 [Dement99, Sobol00] and has been constantly extended with additional features and improvements. In 1995 the European Atomic Energy Agency benchmarked all hadron codes existing at that time. SHIELD successfully passed this examination and yielded reasonable results which were close to those of HERMES and LAHET (see App.A) [Sobol96].

In 1997 the transport of atomic nuclei of different atomic mass was included. This improvement enabled the code to deal with any species of heavy ions and was a huge step towards its universality.

Hence, SHIELD became one of the most powerful programs in the list of Monte Carlo hadron transport codes. In its 1997 release it had the following capabilities:

- Transport of $N, \pi, K, \overline{M}, \mu$ up to 1TeV and arbitrary (A,Z)-nuclei
- 2- and 3-particle modes of meson decay
- Extended targets of arbitrary geometric configuration
- Exclusive simulations of nuclear reaction with a generator based on a Multi Stage Dynamic Model (MSDM)
- Complete storing of each cascade tree

- Transport of low energy neutrons on a basis of the 28-group ABBN data library[12]

Exclusive transport codes

NMTC(ORNL, 1971)→HETC(ORNL,1972)→

LAHET(LANL,1989)→MCNPX(LANL,1997)→…

HERMES(KFA,1989)

NMTC/JAERI(1997)→NMTC/JAM(2001)→PHITS(2002)→…

HETC-3STEP(1995)

HETC(PSI)

etc., up to 10 versions

SHIELD(JINR,1972)→SHIELD(INR,1989)→SHIELDHI(INR,1997) →

→SHIELD-HIT v1(INR,KI,2001)→SHIELD-HIT v2(INR,DKFZ,2006)

FLUKA(1974,CERN)→

FLUKA82(CERN)→ FLUKA87(CERN)

FLUKA92(INFN,CERN)→

Inclusive transport codes

CASIM(1975,FNAL)→|

MARS(IHEP,1974)→…→MASR10(IHEP,1985)→…→MARS13(FNAL,1995)→

MARS14(FNAL,1997-2002)

GEANT

GEANT(CERN, eγ-1976)→

GEANT3(CERN, hA-1980/GHEISHA, 1985/FLUKA) →|

Figure 10 Schematic overview of hadron transport codes.

[12] ABBN is multigroup constant set for calculation of neutron radiation fields and functionals.

For the simulation of inelastic nuclear interactions the Multi Stage Dynamical Model (MSDM) is used [Botvina97]. It consists of several physical models developed at the Institute for Nuclear Research of the Russian Academy of Science (INR RAS), Moscow, and in the Joint Institute for Nuclear Research (JINR), Dubna. MSDM considers in an exclusive approach all stages of a nuclear reaction:

- A fast, cascade stage, which brings the interaction between the projectile and target to a sequence of binary collisions between nuclear constituents and/or produced hadrons [Toneev83]
- Pre-equilibrium emission, when nuclei during thermalization can emit particles [Gudima83]
- Equilibrium de-excitation of residual nuclei, which includes three processes: Fermi break up of light nuclei, Evaporation/Fission competition and Multi-fragmentation of highly excited nuclei [Botvina87].

The code was successfully applied to many different physical problems like: calculation of radiation fluxes originating from cosmic rays behind the shielding of the MIR space station, radiation damage of the MIR structure materials, background conditions in underground experimental halls and many others.

With the fast development of ion therapy the urgent necessity of reliable calculation tools appeared. For radiation therapy purposes the original version of SHIELD was extended to the version SHIELD-HIT (Heavy Ion Transport) [Gudow04]. Since the features included in the new version were driven by applications in radiotherapy the most essential improvements were the inclusion of the straggling effect in energy loss (using Gaussian or Vavilov straggling distributions) and multiple Coulomb scattering (using a two-dimensional Gaussian distribution or so-called Fermi distribution). These processes are of major importance for the simulation of accurate particle path and dose distribution calculations.

2.5 Monte Carlo: Modifications of the SHIELD-HIT v1 for the application in heavy ion dosimetry; SHIELD-HIT v2

As mentioned in 2.4.2, a new version, SHIELD-HIT v1 (for Heavy Ion Therapy), was developed [Gudowska03] for medical purposes. The main modifications were the inclusion of energy straggling (using Gaussian or Vavilov straggling models), multiple Coulomb scattering (using a two-dimension Gaussian distribution) and ICRU-49 stopping power values for protons and alpha particles [ICRU93].

Although this version showed already quite good agreement with experimental data, there were still a number of limitations. The code systematically overestimated the attenuation of

primary particles by about 18% and the height of the Bragg peak was underestimated by a similar amount. Furthermore, the numerical accuracy of the energy loss calculation when transporting ions through thin layers of media like air turned out to be insufficient. Also a consistent calculation of stopping power values for all types of particles was not implemented. In order to allow for a more precise calculation of dosimetrical parameters in question, several modifications of SHIELD-HIT v1 were introduced in the present work [Geithner06].

2.5.1 Transport in low density medium

The problems concerning the ion transport in air were solved in several steps. The older releases of SHIELD and SHIELD-HIT v1 were written using 16-bit precision variables (single precision) in numerical calculations. This was sufficient for the transport of ions in dense media, where the energy loss per integration step is large. The energy loss in thin layers of media like air is very small. Test calculations which were performed in the context of the present work led to large fluctuations in the results. These numerical inaccuracies were traced back to insufficient numerical precision in the variables. In order to improve the accuracy of the calculations, the code SHIELD-HIT v1 was rewritten using 32-bit variables (double precision). Additionally, the energy grids for energy losses interpolation and track length registration were extended and the number of bins increased by a factor of 2. These modifications allowed simulating the energy loss in low density medium correctly.

2.5.2 Stopping power

External table data

The position of the Bragg peak depends on the numerical values of the stopping powers. These also define precisely the particle range, which is of high importance in light particle therapy. In SHIELD-HIT v1, the ICRU-49 recommended data for protons and alpha particles were already built in [Gudowska04]. For carbon ion dosimetry, however, other secondary light ions are also of importance and their stopping power values were calculated according to a simplified implementation of the Bethe-Bloch formula, strictly valid only for very high energies. At present two reliable sources of such data have become available: ICRU-73 [ICRU05] and MSTAR [Paul02]. The data table from these two sources were included into the code and a selection between the Bethe-Bloch formula or one of these data bases can be made for the calculations on user request.

Modification of Bethe-Bloch formula

SHIELD-HIT v1 was able to transport particles down to energies of 1MeV/u. For dosimetrical purposes this cut-off energy is too high, as ranges of particles that correspond

to the size of ionization chambers have to be dealt with. For the typical Roos or Markus plane-parallel ionization chambers the cavity height is 2 mm, which requires decreasing the cut-off energy down to 25keV/u approximately. ICRU-49, ICRU-73 and MSTAR provide the stopping power data for such low energies. Unfortunately, they are available only for a restricted set of media and ions. To be able to use any type of media and ion in the simulations and to make the cut-off energy lower, it was necessary to modify the default high-energy version of the Bethe-Bloch formula implemented in the code, which is applicable only to energies above 1-2MeV/u. Several corrections to the calculation of the stopping power were introduced in order to take into account the deviations from the Bethe-Bloch theory at low energies. First, the effect of electron capture and loss by the projectile at low energies due to interactions with target atoms was taken into account. An empirical expression for the so-called effective charge z_{eff} was introduced. It replaces the bare projectile charge in all relevant expressions by (Hubert et al 1989)

$$Z_1 \rightarrow Z_{eff} = \gamma Z_1(E) \qquad (2.5.2.1)$$

where γ is an energy-dependent parameter. For energies lower than 0.3MeV/u the Lindhard-Scharff model was used (Lindhard et al, 1963):

$$dE/dx = const\sqrt{E}\ . \qquad (2.5.2.2)$$

In order to describe the ionization loss of the charged particle over the total energy range, equation (2.5.2.2) and the Bethe-Bloch equation modified for the effective charge, equation (2.5.2.1), were combined. Their crossing point is where these two functions and their derivatives are equal. The constant in equation (2.5.2.2) is cancelled by equating the function with its derivative.

2.5.3 Fragment production

In order to improve the fragmentation model and consequently the agreement with measurements, some model parameters were adjusted. In the model for inelastic interaction in the stage of equilibrium de-excitation three processes are competing: Fermi break up of light nuclei, evaporation and multifragmentation of highly excited nuclei. For the range of ions under consideration for ion beam therapy (mostly carbon ions) the Fermi break up model is applied (by default up to the Atomic number A_0=16). The volume of decaying system can be calculated as follows:

$$V = 4\pi \cdot r_0^3 \cdot A/3 \qquad (2.5.3.1)$$

where r_0 = 1.4 fm is used. Thus, varying the limit of applicability of the model (i.e. the parameter A_0 which is parameter PARLEV(30) in the code), one influences the fragmentation process of the ion deexcitation[13].

During revision of the code, some other model parameters were introduced: ILEVRA, FKAP1, FKAP2 and PARLEV(39). Adjustment of the presented parameters allows varying and controlling the production of secondary particles [Botvina05]. The influence of PARLEV(39) parameter on the depth dose profile is shown in Appendix C. All other parameters were not varied in the framework of this thesis, but might be of interest for future work.

2.6 Monte Carlo: Validation of SHIELD-HIT v2 using experimental data

In order to carry out accurate theoretical calculations one has to validate and be sure that the computer code produces reliable data. For the validation of the new code version SHIELD-HIT v2 a number of comparisons with experimental data were performed. Several main aspects were checked: depth doses profiles, fragment production and spatial distribution of derived fragments.

Bragg curves

The calculation of depth dose profiles determines mainly the correctness of the stopping power data. As already mentioned above, the I-value in the Bethe-Bloch calculations influence the position of the Bragg peak quite much. As a new feature, SHIELD-HIT v2 has a data set for stopping powers for ions heavier then ^{4}He from ICRU-73 [ICRU05] and MSTAR [Paul02] for a restricted set of materials. Also, the modified Bethe-Bloch formula allows calculating the stopping power data down to 10keV/u in arbitrary media or chemical elements.

The measured depth dose profiles for the ^{12}C and ^{16}O were taken from the literature [Sihver98, Matsuf03]. The measurements were performed at GSI, Germany and RIKEN and HIMAC, Japan. Four curves were measured in the framework of the present project for ^{12}C and ^{3}He. Further measurements, described in paragraph 2.7, were performed in the framework of this thesis.

[13] This model parameter can be varied from A=17 down to 4.

Production of fragments

Even if the calculations show good agreement of Bragg peak position and height with the measured data, the code does not necessarily calculate the correct spectra. The physical models in the Monte Carlo code can overestimate or underestimate the amount of produced fragments and lead to the wrong attenuation of the primary particles. As the depth dose profile presents the superposition of dose deposited from primary particle generation plus secondary and further generations, it is important to check separately the production of fragments in different depths of penetration.

The attenuation of primary particles and the distribution of the fragments were measured for ^{12}C by Matsufuji at HIMAC, Japan [Matsuf03]. The particles were registered and separated in charge after the penetration of the PMMA phantom within an angle of 12°. The separation of different isotopes was not performed.

Spatial distribution of derived fragments

In order to analyze the performance of the exclusive approach and the dynamics of fragmentation process in the code, also angular distribution of the produced fragments were compared with measurements.

The spatial distribution of the fragments was measured by Gunzert-Marx at GSI [Gunzert04]. The isotopes of the fragments from ^{12}C were registered at different angles to the primary beam direction.

3D Dose distribution derived from the scanned carbon beam

For the irradiation of patients the carbon beam is scanned in X, Y and Z directions (explained in 2.7). As it is know, that the existing at GSI beam model shows deviation from the measurements at large depths in water, the code was checked as well by performing simulations of realistic scanning beams and spread-out Bragg peak at large depth. Measurements of such beam profiles and spread-out peaks were done also in the framework of this thesis. The full description of the experimental set-up and measurement procedure is presented below in paragraph 2.7.

2.7 Measurements performed at GSI for present thesis

For the validation of the SHIELD-HIT v2 code several measurements were done at the Gesellschaft für Schwerionenforschung (GSI), Darmstadt. For the patient irradiation with carbon ions within the pilot project at GSI, Cave M was equipped as a treatment room. The beam is delivered from the synchrotron and with the help of an active beam-delivery system. The synchrotron is able to change the delivered beam energy within several

seconds. The active beam-delivery system consists of two magnets and the monitor system. The magnets deflect the charged particles in horizontal and vertical direction and the monitor system detects the position of the beam. Hence, the 3D delivery technique at GSI is achieved using only active elements, which avoid the additional production of secondary particles (fragments) from a range shifter or bolus (see Fig.11). The technical aspects of the raster scanning beam delivery system are described in [Haber93].

In order to irradiate the volume of interest (VOI) homogeneously and to deliver the prescribed dose there, the following procedure is used:

- Definition of the VOI**.** In the case of real patient it is the tumor volume together with additional margins for uncertainties. For the present work the cubic volume (2.5x2.5x2.5) in the water phantom in the depth of 19cm was chosen with a prescribed dose of 1Gy.
- The treatment planning program TRiP, developed at GSI [Krämer00] optimizes the irradiation plan in order to get the number of particles need in every raster scan position. One should note that the active beam delivery system described already above and shown in Fig.11 delivers the beam in XY plane with 2mm step size (using scanning magnets) and in Z depth with 3mm by changing the initial energy from synchrotron. The monoenergetic beam is extended with the help of mini ripple filter[14] [Weber99].
- After optimization, a special scanner control file (so-called rst file) is created, which consists of the information about the position of beam in XY plane and the amount of particles to be delivered. Depending on the necessary depth, each XY-matrix corresponds to a single beam energy.

[14] This device (see Fig.11) is made from PMMA material and used to broaden the very sharp Bragg peaks of ions in order to facilitate the generation of a homogeneous dose distribution.

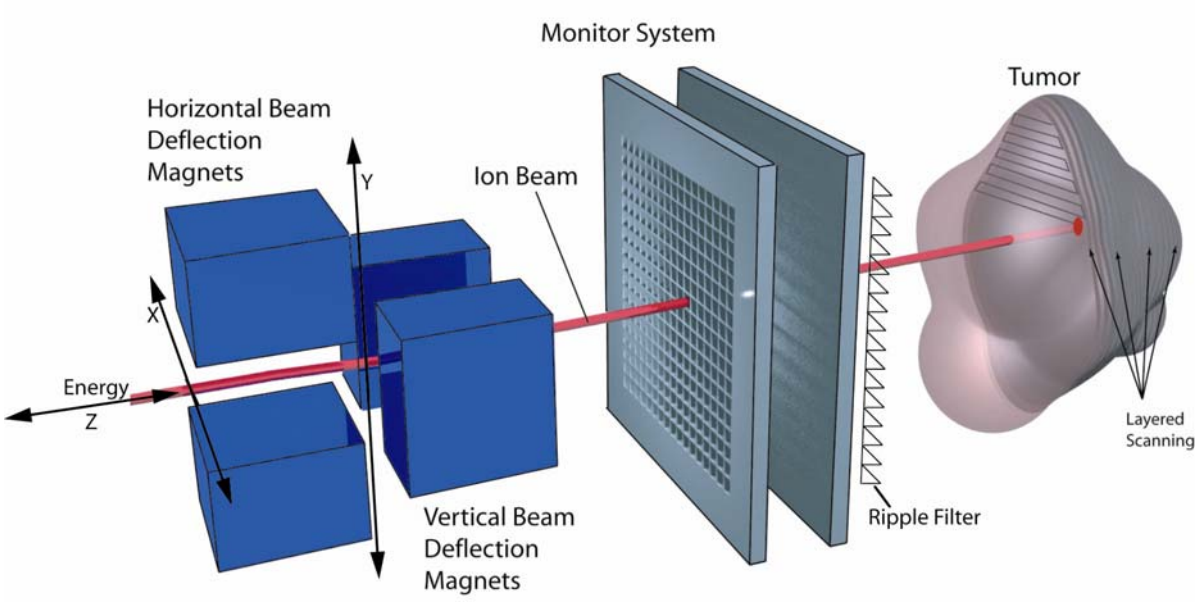

Figure 11 Schematic view of the active beam delivery system used at GSI. The pencil beam is scanned over the transversal area by the deflection magnets, while the penetration depth is modified by an active variation of the beam energy from synchrotron.

2.7.1 Monoenergetic Depth Dose profiles (Bragg curves) with ^{12}C and ^{3}He ion beams

For the measurements of the monoenergetic depth dose profiles a water phantom manufactured by PTW and MP3 control devices were used (see Fig.12). In both experiments with ^{12}C and ^{3}He ion beams an ionization chamber was fixed in a special plastic chamber holder in a water phantom.

The movement of the holder within the phantom was done automatically with the PTW MP3 control device, which provides a minimal step size of 0.1mm.

The energy deposition from a ^{3}He monoenergetic beam (FWHM=6mm) with energy of 168MeV/u was measured with a standard PTW Roos ionization chamber (radius of active volume R=1.2cm), which has a plane-parallel geometry. The experimental offset was 37 ± 0.3mm in water. The peak was measured with a step size of 0.5mm.

Three curves with energies of 195, 270 and 330MeV/u were measured with ^{12}C monoenergetic beam (FWHM=6mm) using the modified PTW Roos chamber[15]. The offset in water was 39.9 ± 0.3mm. The Brag peaks were measured with a step size of 1mm in water.

[15] Modified Roos chamber has four times larger radius of the sensitive volume (R=2.4cm).

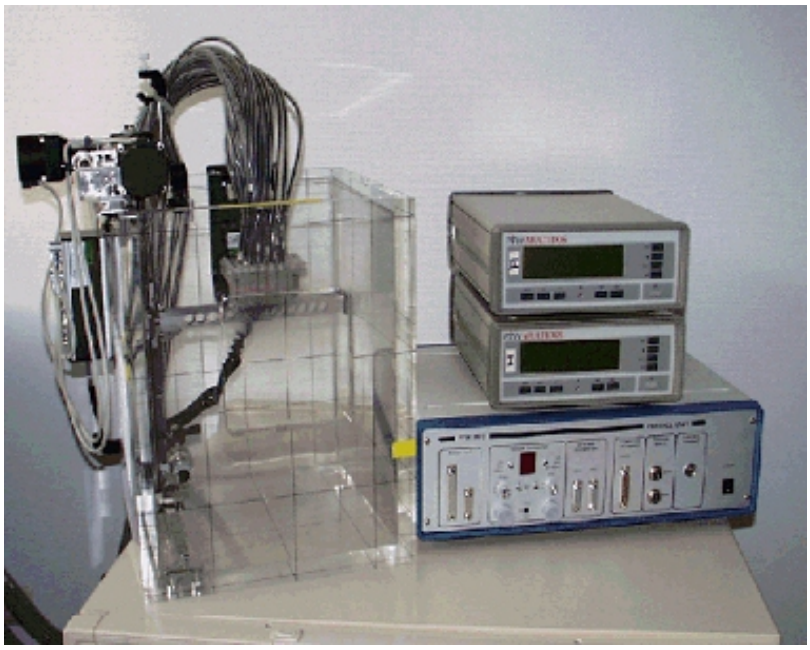

Figure 12 Set of devices used for the measurements. Left: PMMA phantom filled with water with array of pin-point ionization chambers. Right: 2 UNI-DOSE and MP3 control device for the ionization chambers operation.

2.7.2 Lateral profiles of the scanned cubic volume and Spread-Out Bragg Peak (SOBP)

For the irradiation the following VOI was chosen: a cubic volume with an edge length of 2.5cm. It was situated in the water phantom with following coordinates according to Fig.11:

- X[-1.25;1.25]cm
- Y[-1.25;1.25]cm
- Z[19;21.5]cm

Following the procedure of optimization described above, for the given volume an irradiation plan was calculated that contained 13 different energies as shown schematically in Fig.13. A homogeneous dose of 1Gy was chosen in the optimization using the treatment planning procedure.

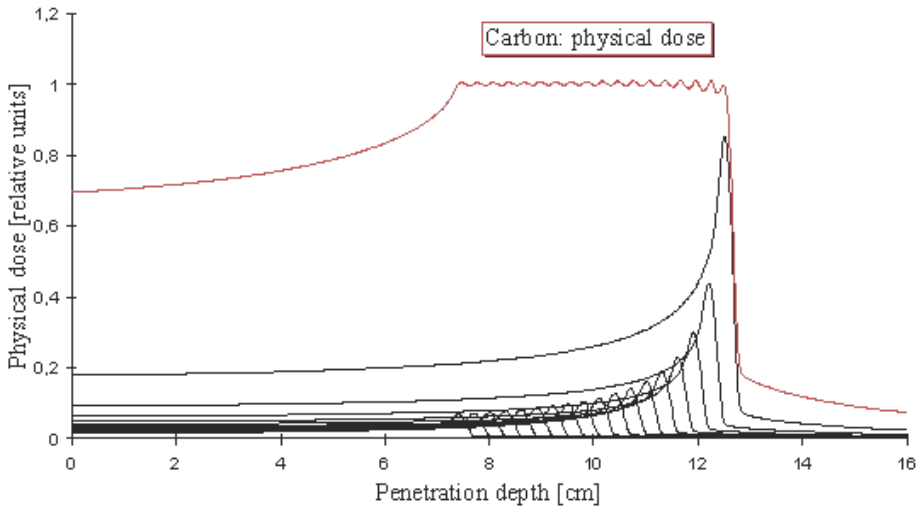

Figure 13 The superposition of the depth dose profiles with different beam energies issues a so-called spread-out Bragg peak (SOBP), which covers the tumor volume in depth.

The measurements of the lateral profiles of the scanned cubic volume were performed in the water phantom using pin-point ionization chambers with active volume of 0.03cm^3 [Jäkel06]. 24 chambers were placed into a special PMMA array in one line (see Fig.14). Such a linear array allows measuring of the whole lateral beam profile at one depth simultaneously.

Figure 14 Array of 24 pin-point ionization chambers in a PMMA holder.

As the distance between two neighboring ionization chambers is 8mm, the profile measurement in every depth was made two times in order to get more measurement points. One time with the middle of array positioned at (0, 0, Z) mm and another at (4, 0, Z) mm. To extract the depth dose profile of the irradiated cubic volume (so-called Spread-Out Bragg Peak), the measurement data of the two middle pin-point chambers were taken. The offset of the measurements was 10.5mm in water.

2.8 Simulation with SHIELD-HIT v2

This chapter describes the details of the simulations with SHIELD-HIT v2 together with the geometry used in the calculations, target material and initial beam parameters. For all calculations in present work with SHIELD-HIT v2 the following parameters of the fragmentation model were used:

PARLEV(30)=16

ILEVRA=1

FKAP1=1

FKAP2=1

PARLEV(39)=0.8

The stopping power data in water for protons and alpha particles were taken from ICRU-49 and from ICRU-73 for heavier ions. The stopping powers for alpha particles of energies from 250MeV/u up to 1000MeV/u were calculated from the modified Bethe-Bloch formula included in SHIELD-HIT v2.

2.8.1 Simulations for the validation of the code

For the validation of the modified version of the SHIELD-HIT v2 several comparisons of calculations with experimental data were done.

Bragg curves

The measurements of the depth dose depositions performed at GSI by Sihver [Sihver98] were performed with two large quadratic area ionization chambers (20x20cm), thus integrating over the whole lateral beam profile. Therefore, the simulation was performed in a water cylinder of 10cm radius and 30cm length. The cylinder was divided into 3000 identical slices of 0.01cm thickness. The pencil[16] beam used for the simulations had an energy spread of 0.2%.

[16] Pencil beam in paragraph 2.8 means that FWHM of the primary beam was 0.

For the simulations of the Bragg curves measured for the present work at GSI (described in 2.7.1) a water cylinder with a radius of 2.4cm (for ^{12}C) and 1.2cm (for ^{3}He) and a length of 30cm was used that corresponds to the geometry used in the measurements. It was divided into 3000 slices of 0.01cm thickness each. The beam parameters were the same as for the previous simulations.

Fragment production

For the simulations of the Bragg curve obtained at Chiba, Japan [Matsufuji03] the same geometry as for ^{3}He but with a radius of 2.5cm was used. The calculations of primary beam attenuation and fragments production were performed with selective condition: all particles were registered within an angle of 12°. The pencil beam had an energy spread of 0.15%.

Simulations of the attenuation of primary particles in water, which was measured at GSI [Shall96], were performed in water cylinder of 10cm radius and 30cm length. The energy spread of the primary pencil beam was 0.2%.

For the comparison of the simulations done with GEANT4 [Benitsch05], [Wilkens06], a cylindrical geometry with a radius of 10cm and a length of 30cm was used. The thickness of slices was 0.01cm. All calculations were done in water with the pencil beam with an energy spread of 0.445%. The energy spread was chosen to simulate the ripple filter used at GSI.

The spatial fragment distributions for the carbon ions were measured at GSI by Gunzert-Marx [Gunzert04]. The simulations were done using a water cylinder with a radius of 10cm and 12.78cm length. The particle spectra differential in energy and angle were registered in air after the penetration of the whole water depth. The registration was performed under different angles: 0°, 10° and 30° degrees.

3D Dose distributions

For the simulation of the lateral profiles, a special geometry was made [Jäkel06]. The detailed description of the experiment is given above in paragraph 2.7.2. For the simulation, a water cylinder of 10cm radius and 30cm length was divided into concentric cylinders with radii from 0.2cm up to 3cm in 0.2cm steps. The cylinders were divided as well along the length into equal slices of 0.1cm thickness. In order to simulate a ripple filter, used for the real measurements, a beam energy spread of 0.445% was applied in the simulations. In the experiment the carbon beam was scanned in X, Y and Z directions (see Fig.11). To simulate the “scanned beam” in **Y direction**, three parallel beams were calculated with different entrance coordinates (in cm) of X, Y: (0,-0.2), (0, 0) and (0, 0.2). After obtaining the results for the three individual beams, they were added together to receive the profile for the scanned beam. As the beam profile was measured in all depths with pin-point chambers, positioned at Y=0, these three beams were enough for the simulations of the

scanned beam in Y direction. After the superposition of the calculated three beams a beam profile in all water depths was received. This profile was fitted using a spline function in order to get more simulation points via the fit function. For the simulation of scanning in **X direction**, the final profile was generated by adding profiles in X direction from -1.6cm to 1.8cm in 0.2cm steps (in general 18 profiles). Finally, for the simulation of the beam scanning in **Z direction** 13 initial energies with different numbers of primary particles were used (see Table 2). The geometrical size (FWHM) of the primary beam was 8mm.

Table 2 List of the initial energies and corresponding number of primary particles, obtained from the optimization procedure for homogeneous irradiation of cubic volume with a length of 2.5cm situated in 19-21.5cm water depth (so-called CUB113).

Energy, MeV/u	Number of primary particles
321.12	60888.8
323.21	34743.4
325.30	47679.4
327.38	47648.4
329.44	51888.0
331.47	50017.6
332.98	37455.3
334.49	72302.4
337.50	109986.0
338.99	30872.3
340.49	129717.0
343.46	164771.0
344.94	392473.0

For the investigation of the fragment contribution to the total lateral deposited dose the same procedure as described above was used, besides the simulation of the beam scanning in Y direction: only one beam was calculated with entrance coordinates of X,Y(0,0).

For the simulations of the depth dose profiles of the spread-out Bragg peak it was enough to calculate the "scanned beam" only in Z direction. The water phantom model with radius of 2cm and 30cm length was divided into 3000 equal slices of 0.01cm thickness and irradiated with 13 carbon beams of different energy. The size of the beam was 8mm (FWHM) and the energy spread of 0.2%. To simulate the ripple filter, a special ripple filter transmission function developed at GSI was applied that describes the change of the Bragg peak position, width and height due to the filter.

2.8.2 Calculation of the STPR

Equation (2.3.2.1) for the stopping power ratio requires the particles spectra only in water, thus, all calculations of $s_{w,air}$ were performed modeling water.

The stopping power ratios for a carbon ion beam were calculated using a water cylinder with a radius of 10cm and 40cm length that was divided into 400 equal slices of 0.1cm thickness. The initial pencil beams of different energies were monoenergetic. The cut-off energy for the particle transport was Δ=25keV/u (the lowest energy, available from the ICRU-73 stopping power data set). The particles with energy less then Δ were stored in a special "stoppers" array and used to calculate the dose deposited from the stoppers.

The same procedure for the calculation of $s_{w,air}$ with the same geometry and beam parameters was done as well for ^{3}He and ^{4}He beams.

The influence of the fragments on the total stopping power ratio was calculated as follows: first just using the primary particle spectrum and then adding different fragment spectra separately.

The ratios of stopping powers water-to-air for different ions were calculated just using the data directly from ICRU tables (i.e. no Monte Carlo calculation involved).

The stopping power ratios for different ions were calculated in water cylinder with a radius of 10cm and 30cm length, which was divided into 3000 equal slices of 0.01cm width each. The beam parameters and cut-off energy were the same as described above.

For the calculation of stopping power ratios for carbon beams using stopping power data with different I-values BEST[17] data were used [Paul2006]. The calculations were done in a water cylinder (10x30) cm divided into 300 equal slices of 0.1cm thickness with a monoenergetic pencil beam of two initial energies: 50Mev/u and 400Mev/u.

[17] Bethe stopping power code including shell, Barkas, Bloch and density effect correction. This code has been used for the preparation of the high-energy part of the tables in ICRU-49.

2.8.3 Simulations for antiprotons

For the investigation of the biological effectiveness of antiprotons several experiments were carried out at CERN, Switzerland. The aim of experiments was to measure the absorbed dose deposited by antiprotons and their fragments in different depths. A more detailed description of the experimental set up is given in [Bassler06]. For the dose measurements a TLD 600 (with ^{6}Li) and TLD 700 (with ^{7}Li) and Alanine dosimeters ($C_3H_7NO_2$) were used. To calculate the efficiency of their response on irradiation the differential energy spectra of primary and secondary particles simulated by SHIELD-HIT v2 were used. The transport of antiprotons with energy of 47MeV was done in a polystyrene cylinder (C_8H_8). The radius of the cylinder was 2cm for TLD's, 1cm for Analine and 4.6cm length for both. Inside the cylinder along the central axis TLD or Analine tablets were build in at different depths. As the size and the energy spread of the primary beam in experiment were unknown, a monoenergetic pencil beam was assumed in the simulations.. The particle spectra were extracted from the TLD tablets zone and used for the evaluation of the signal. The dose deposition in the dosimeters was calculated in order to compare it with measured signal.

2.8.4 Calculations of the F-factor

To calculate the combined correction factors: stopping power ratio, perturbation factor and *W*-value as explained in paragraph 2.3.3, a realistic plane parallel ionization chamber was simulated (see Fig.7 and App.2). The dose deposition in the chamber was calculated at different depths in a water cylinder. The cavity of the Roos chamber has radius of 1.2cm and 0.2cm length. The irradiation was simulated with monoenergetic pencil beam of carbon ions with energy of 300MeV/u. The F-factor was defined from the dose ratio water/air as it is given in equation (2.3.3.1). The direct scoring of the energy deposited in the air cavity divided by its mass yielded the quantity $\overline{D_{air}}$ .For the calculation of the dose to water D_w the same geometry was simulated completely in water and the deposited dose was extracted from the thin water layer (0.01cm) at the effective point of measurements[18] (the point in depth to which the measured or calculated dose refers.).

The detailed description of the calculation of F-factor is given in [Semp04].

[18] For the Roos chamber the effective point is situated at the entrance of the sensitive volume.

3 Results

The following chapter is divided into three parts. In the first subchapter the verification of SHIELD-HIT v2 is presented. Calculations of stopping power ratios for different ion species are given in the second part. Additionally, the influences of the secondary particles as well as different I-values on the total stopping power ratios are elucidated. The results of the code application in the other physical tasks like transport of antiprotons or simulation of a realistic ionization chamber are presented in the last subchapter.

3.1 Verification of SHIELD-HIT v2

3.1.1 Stopping Power

In order to reduce the cut-off energy in the particle transport of SHIELD-HIT v1, several modifications of the Bethe-Bloch formula were introduced (see paragraph 2.5). The stopping powers calculated with the “old” and the “new” version of the Bethe-Bloch formula are shown in Fig.15 and Fig.16. The calculated data are compared with ICRU-73 [ICRU05], which is recognized as a standard.

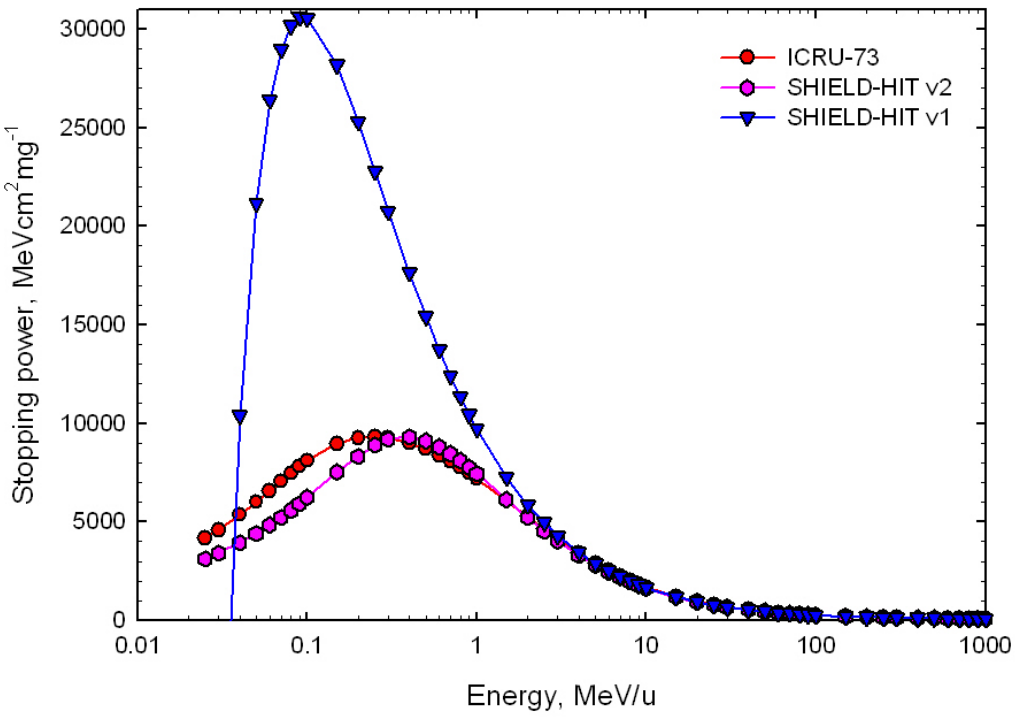

Figure 15 Comparison of the stopping power for carbon ions in water calculated with classical and modified Bethe-Bloch formula with data from ICRU-73 [ICRU05].

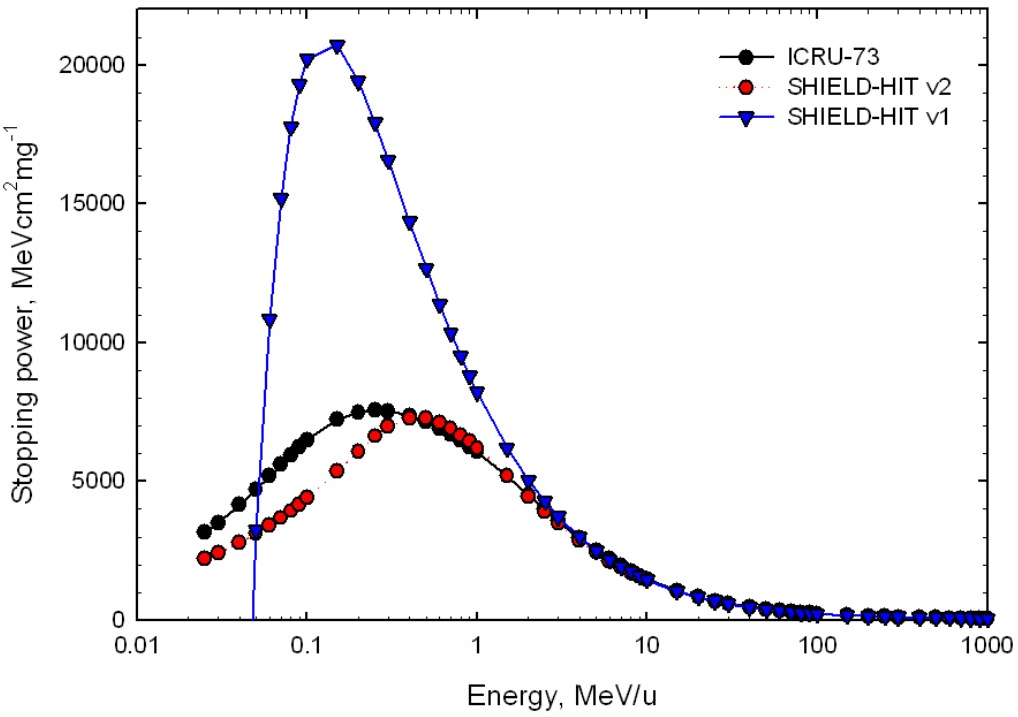

Figure 16 Comparison of the stopping power for carbon ions in cortical bone calculated with classical and modified Bethe-Bloch formula with data from ICRU-73 [ICRU05].

As most of the calculations in the present work were done for carbon ions in water, Fig.15 shows the stopping power for ^{12}C ions in water. As second check of the modified formula, a calculation was also done for a more complex medium. The corresponding results for the carbon ions in cortical bone are presented in Fig.16.

One can see from the comparison of both results for two different media that the modified Bethe-Bloch formula is able to reproduce the reference data given by ICRU-73 with good agreement. Quantitatively, for carbon ions in water (see Fig.15) at the energy of 0.1MeV/u the deviation from the ICRU-73 stopping power value was decreased from 275% down to 25%. Similar improvement is observed for the cortical bone in Fig.16.

3.1.2 Depth Dose Profiles

The depth dose distributions as a function of the depth in water for carbon ions beams with energy of 270MeV/u and 330MeV/u are shown in Fig.17. The results, obtained from SHIELD-HIT v1 and SHIELD-HIT v2 versions are compared with data measured at GSI [Sihver98].

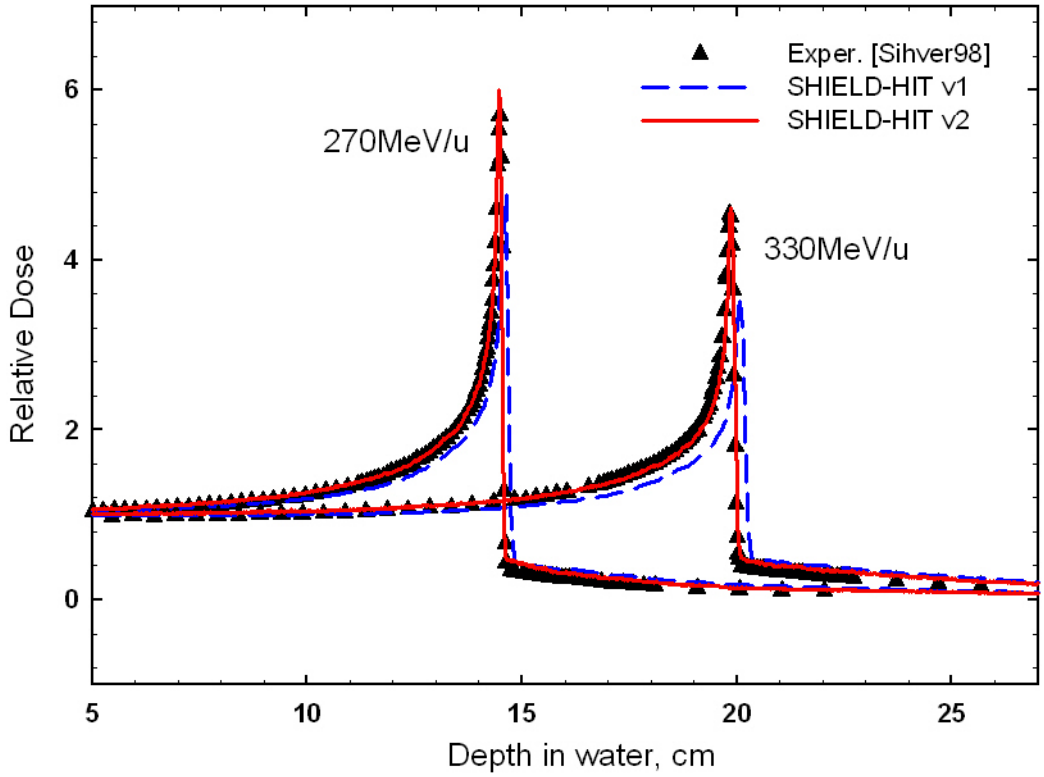

Figure 17 Comparison of the SHIELD-HIT calculations with measurements performed at GSI [Sihver98] for the distribution of energy deposition (normalized to the entrance dose value) as a function of depth in water. The measurements and simulations were done for a water phantom, irradiated with a carbon beam with initial energies of 270MeV/u and 330MeV/u.

The calculations of dose profiles in Fig.17, performed with SHIELD-HIT v1 yielded a shift of the peak position in comparison with measurements up to 2mm and an underestimation of the peak height up to 22%. SHIELD-HIT v2 reproduces the measured data very well. For the energy of 270MeV/u SHIELD-HIT 2 overestimates the measured at peak dose by 5%.

Another comparison of the depth dose deposition but at lower energies is illustrated in Fig.18. The measurements for a carbon beam in water of 135Mev/u were done at RIKEN, Japan. The curve with an energy 195MeV/u was measured at GSI, Germany. The calculation of both curves for comparison was performed using SHIELD-HIT v2. The code reproduced the peaks position correctly, though overestimated the peak height by 10% und 5.4% for the 135MeV/u and 195MeV/u correspondently.

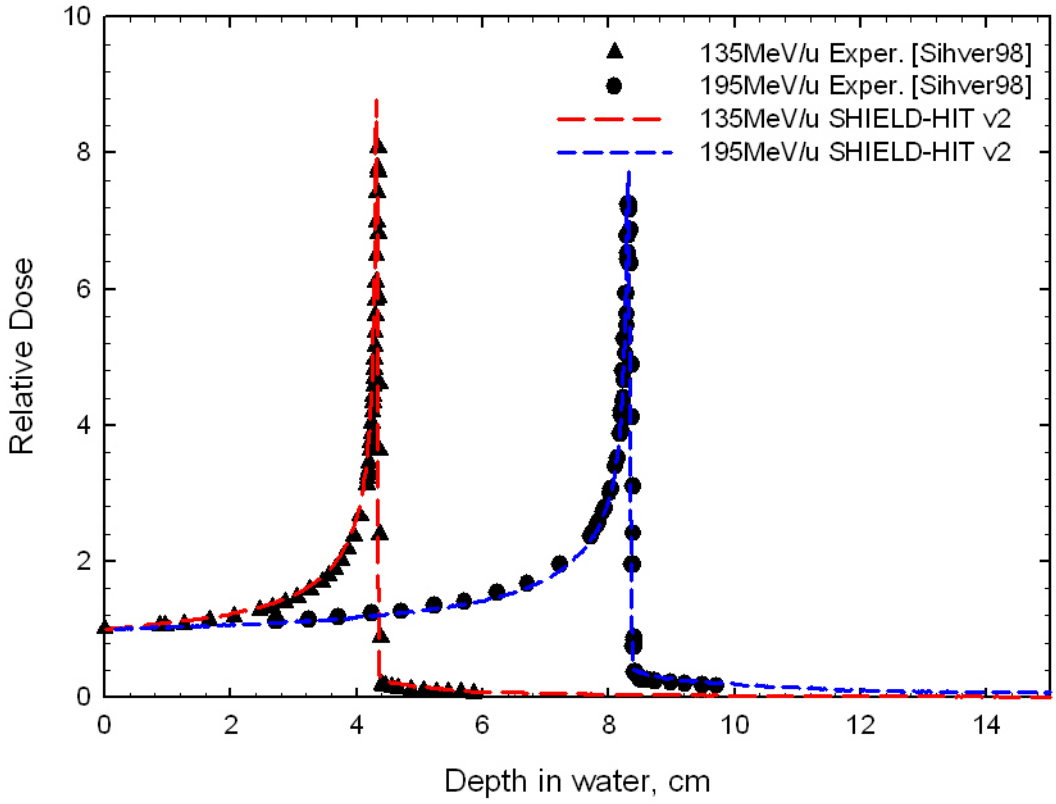

Figure 18 Comparison of the SHIELD-HIT calculations with measurements at GSI and RIKEN [Sihver98] for the distribution of energy deposition (normalized to the entrance dose value) as a function of depth in water. The measurements and simulations were done for a water phantom, irradiated with a carbon beam with initial energies of 135MeV/u and 195MeV/u.

Apart from the external experimental data, in the framework of the present project several own measurements of the depth dose depositions were performed at GSI. The detailed description of the corresponding experimental setup is given in paragraph 2.7. Three curves with ^{12}C ions with energies of 195, 270 and 330MeV/u are plotted in Fig.19. The difference in the peak heights between the curves measured in the present work and those from the external data for the energies of 195, 270 and 330MeV/u given in Fig.17 and 18 are 16.45%, 15% and 9.7% correspondingly. The accuracy of the performed measurements is influenced by the rather coarse steps of the measured points and an absence of repeated measurements to reduce the fluctuations.

In Fig.20 the depth dose deposition measured in water from ^{3}He beam of 168MeV/u is compared with simulated SHIELD-HIT v2 data. The code reproduced the peak position correctly, but overestimated the peak height by about 10%.

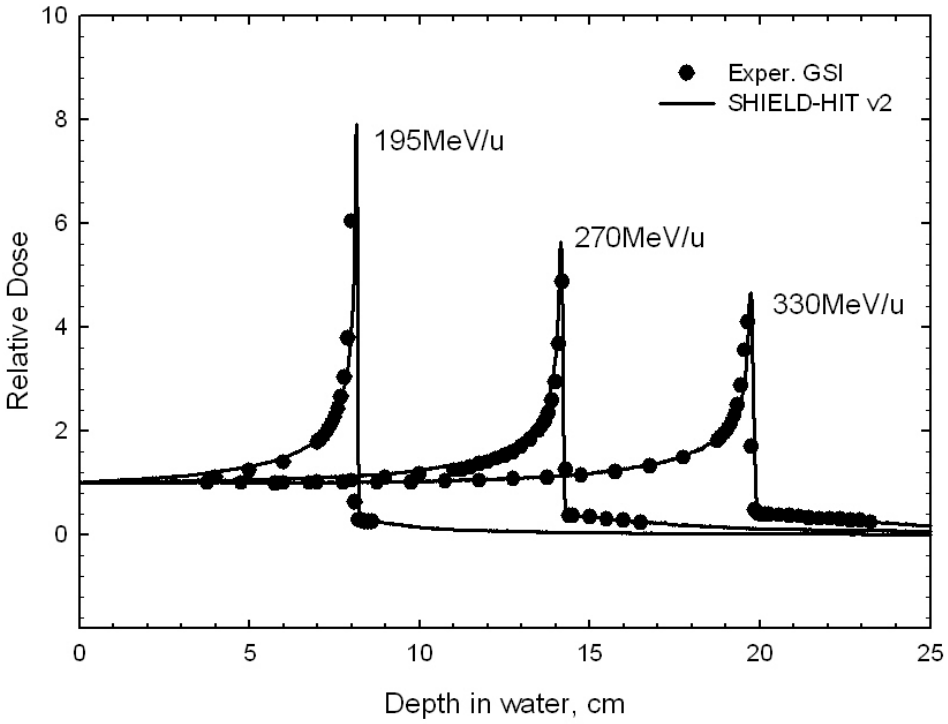

Figure 19 Comparison of the depth dose depositions from carbon beam with three different energies of 195, 270 and 330Mev/u measured at GSI and calculated with SHIELD-HIT v2.

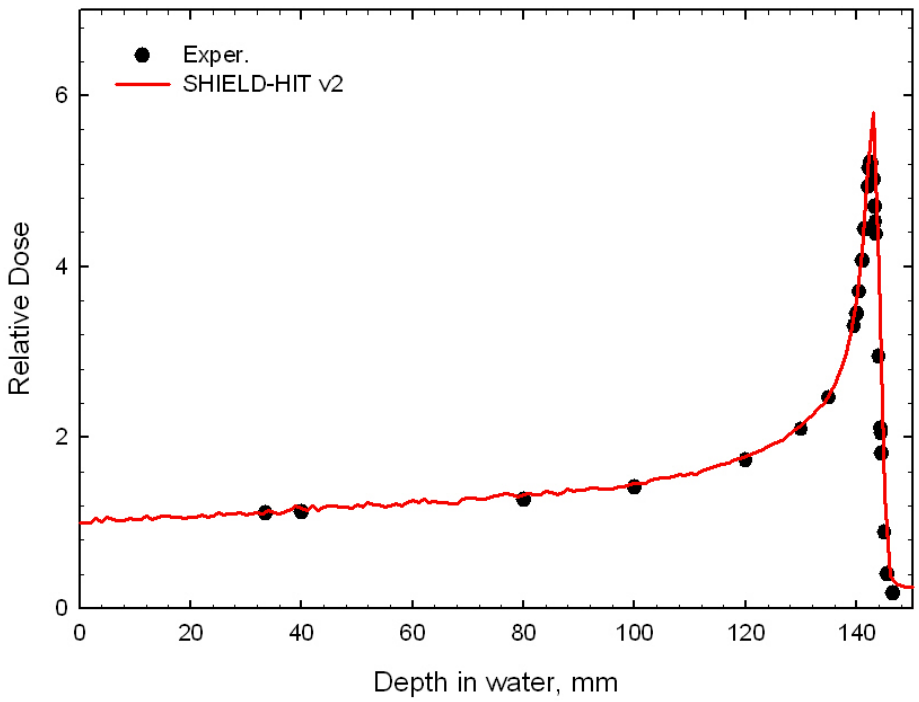

Figure 20 Bragg curve for a ^{3}He beam with the energy of 168MeV/u measured at GSI and compared with SHIELD-HIT v2 simulations.

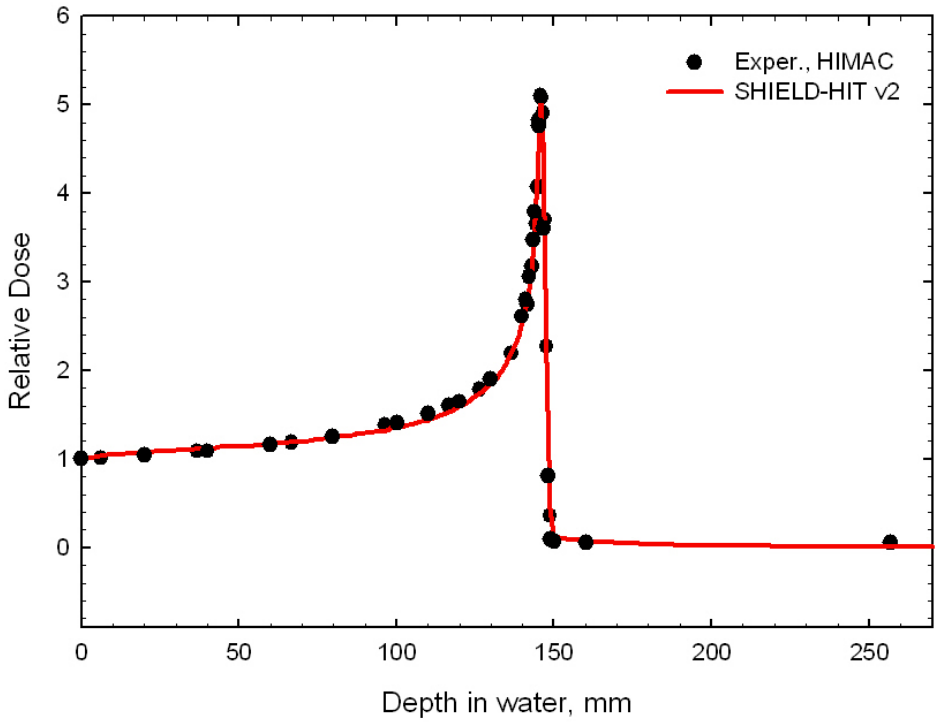

Figure 21 Distribution of the dose deposition from ^{4}He of 150MeV/u measured at HIMAC [Mastufuji03] compared with SHIELD-HIT v2 calculations.

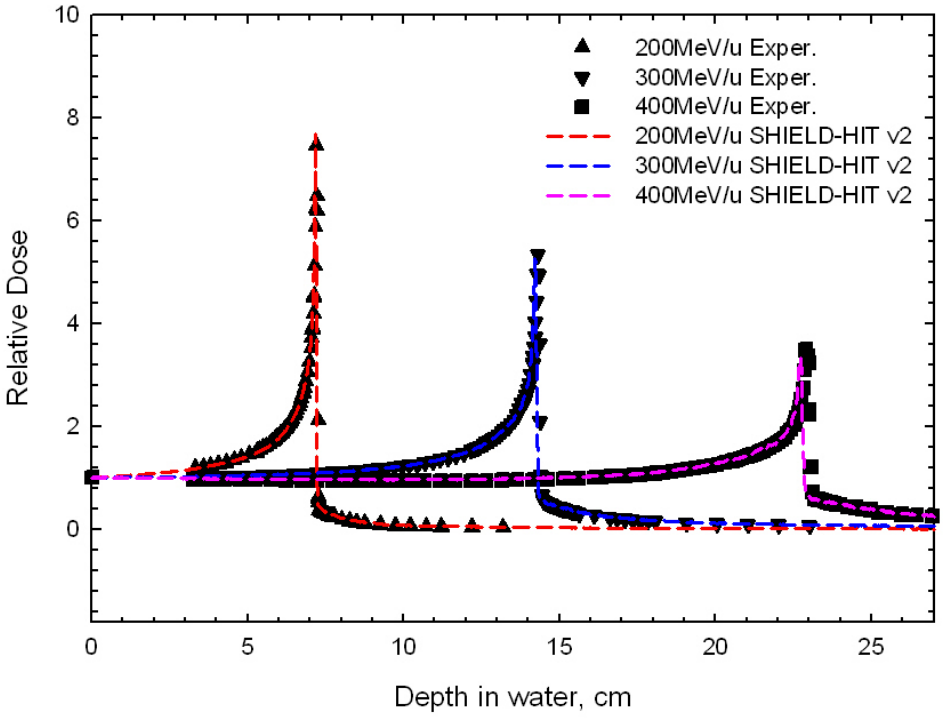

Figure 22 Comparison of the depth dose deposition from ^{18}O measured at GSI [Sihver98] with SHIELD-HIT v2 calculations.

The depth dose distribution obtained from another beam quality (^{4}He) and another accelerator (HIMAC, JAPAN) is compared with SHIELD-HIT v2 calculated data in Fig.21. The position and height of the measured and calculated peaks show a perfect match.

The comparison of the Bragg curves for an ^{18}O beam in water of three different initial energies measured at GSI [Sihver98] and calculated with SHIELD-HIT v2 is shown in Fig. 22. The code reproduces correctly the position and height of the peaks with beam energies of 200MeV/u and 300MeV/u. The calculated profile with highest energy (400MeV/u) is slightly shifted (1.5mm) and underestimated (5%).

3.1.3 Production of fragments

Figure 23 compares the particle fluence distributions, as a function of depth, calculated with SHIELD-HIT v2 and measured at HIMAC [Matsufuji03]. In Fig.23 (Top) the attenuation of primary carbon beam of an energy 290MeV/u is plotted together with proton and alpha particle fragments. In Fig 23 (Bottom) the distribution of secondary particles is shown (Li, Be, B). All data are normalized to the initial number of primary particles. SHIELD-HIT v2 reproduces an attenuation of primary particles and fragments production correctly besides alpha particles (-13%) and beryllium (+50%).

The attenuation of primary particles of different beam qualities is shown in Fig.24. The measurements were performed at GSI with different pencil beams of ^{12}C, ^{14}N and ^{16}O in water with energies of approximately 670MeV/u [Sihver98]. The experimental data are compared with Monte Carlo Calculations done with version v1 and v2 of the SHIELD-HIT code. SHIELD-HIT v1 overestimates regularly the attenuation of projectiles up to 29%. The measurements and SHIELD-HIT v2 calculations show perfect agreement.

The contribution of primary and secondary particles to the total dose deposition from a carbon beam of 391MeV/u in a water phantom (20x30) cm is presented in Table 3. The total energy deposition into the water cylinder is 4692 MeV (391 MeV/u x 12). As can be seen, only 63.02% of the whole energy is deposited in the target volume, the remaining fraction is taken away mostly by neutrons and protons. The primary ^{12}C particles contribute only by 43.2% to the total dose in the phantom. The leakage from the target makes up 31.27% of the dose. The remaining dose is spent for the binding energy and minor fragments, not shown in the Table. The following fragments are of highest importance in the energy contribution: protons (7.79%), ^{11}C (4.18%), ^{4}He (2.68%) and ^{11}B (2.54%).

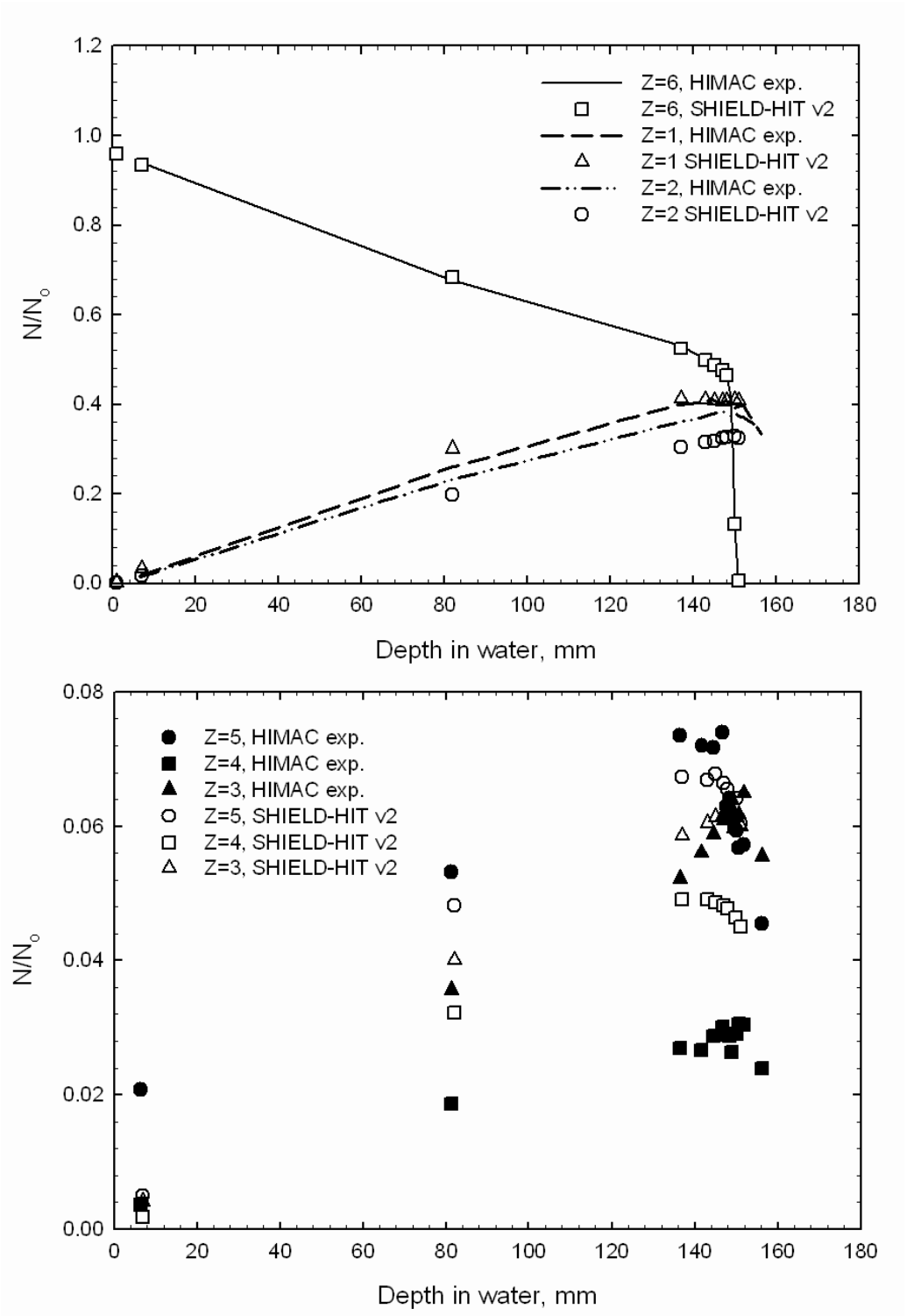

Figure 23 Top: Fluence of primary (Z=6) and light fragments (Z=1, 2) relative to the incident particle fluence, N_0, as a function of depth in water produced by an incident carbon beam of 290Mev/u. Bottom: Fluence of intermediate fragments (Z=3-5).The experimental data from HIMAC [Matsufuji03] are compared with the calculations from SHIELD-HIT v2 and YIELD.

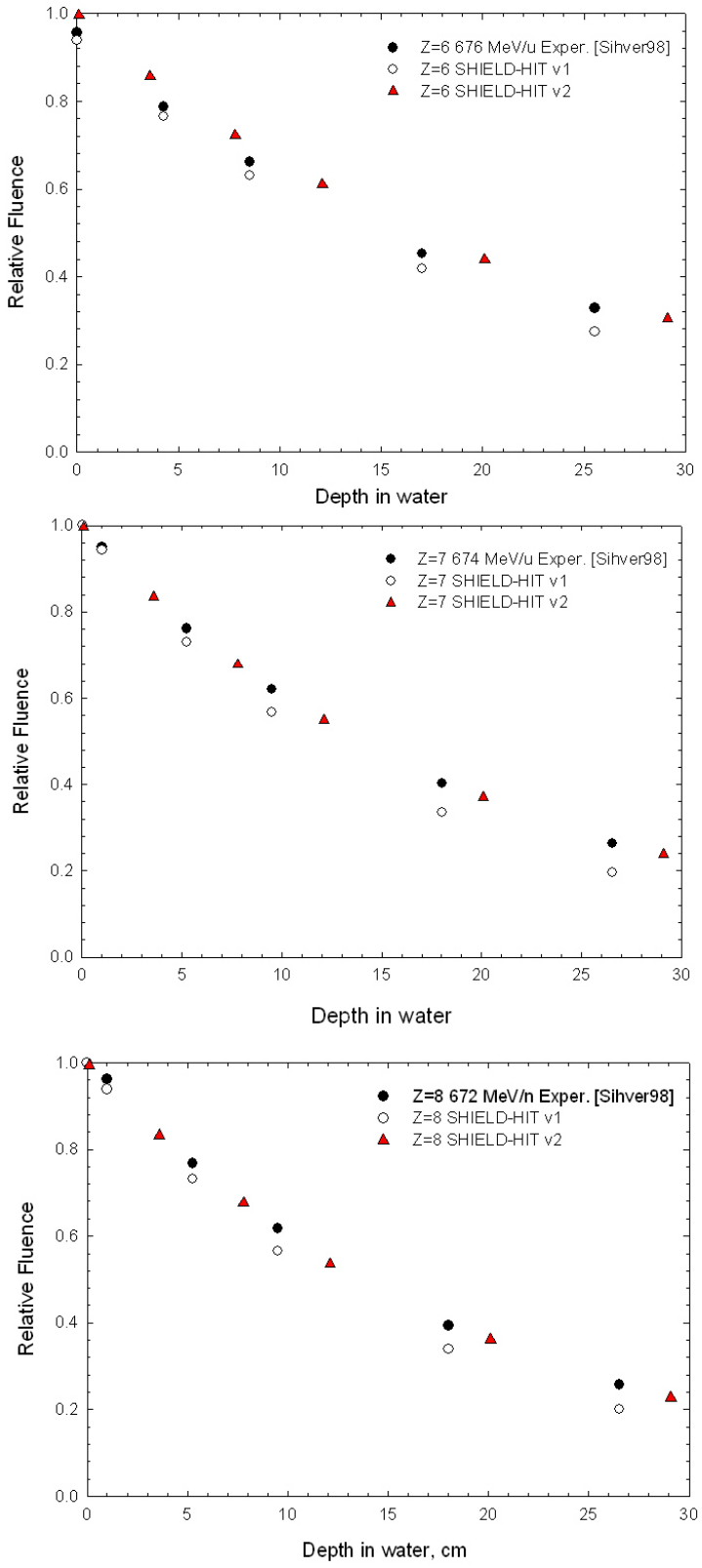

Figure 24 Attenuation in water for beams of ^{12}C, ^{14}N and ^{16}O with an initial energy of about 670MeV/u. Measured data [Schall96] are compared to those calculated with SHIELD-HIT v1 and SHIELD-HIT v2.

Table 3 Calculation of energy deposition from a carbon beam of 4692 MeV (391MeV/u) in a cylindrical water phantom (20x30 cm). The first two columns show the energy, deposited inside the phantom and the last three give the number per primary projectile and the energy, deposited outside the cylinder. Last row is the sum of the every column.

Particle/ Fragment	Energy Deposition within target		Leakage from Target		
	MeV/Proj	%	No/Proj	MeV/Proj	%
Neutrons	-	-	5.34	633	13.49
Protons	365.4	7.79	2.29	395	8.42
Deuterons	20.7	0.44	0.16	71.6	1.53
Tritium	7.5	0.16	0.07	46.1	0.98
^{3}He	44.1	0.94	0.10	53.4	1.14
^{4}He	125.6	2.68	0.30	217	4.62
^{7}Li	27.5	0.59	0.02	25.7	0.55
^{9}Be	21.3	0.45	0.01	8.61	0.18
^{11}B	119	2.54	0.01	12.3	0.26
^{12}C	2027	43.20	-	-	-
^{11}C	196.3	4.18	-	-	-
Pion	2.1	0.05	0.06	4.6	0.1
SUM	2956.5	63.02%	8.36	1467.3	31.27%

3.1.4 Comparison with GEANT4

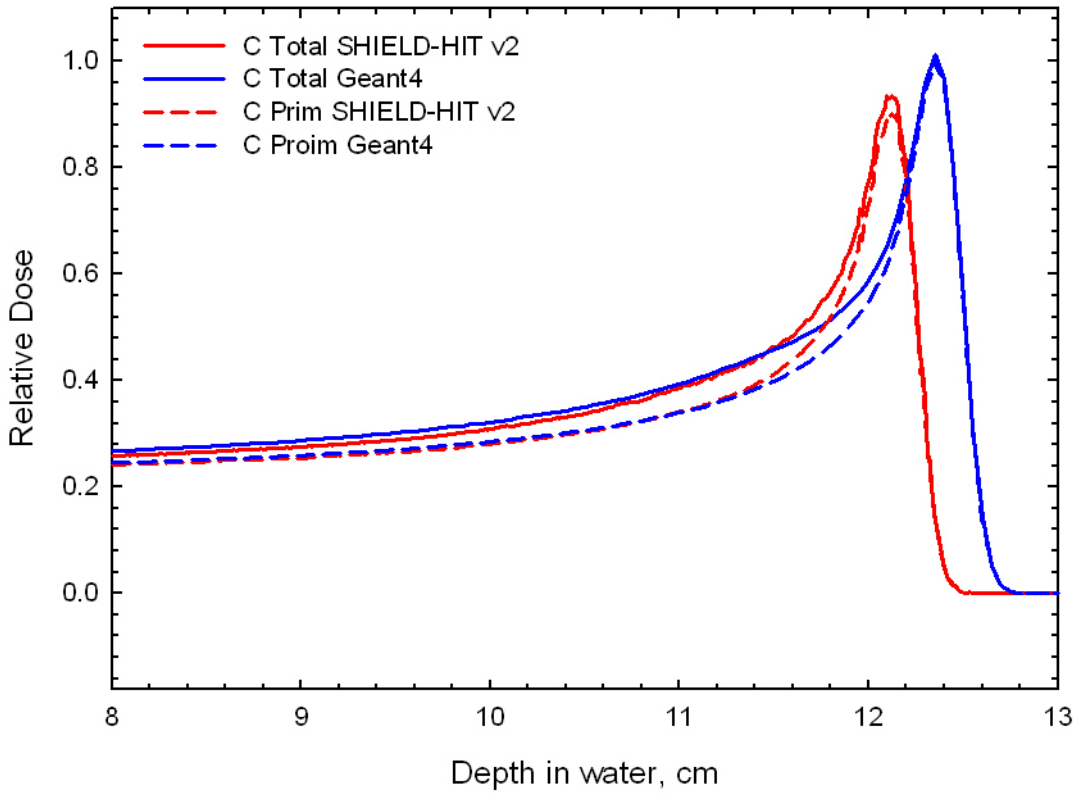

Figure 25 Comparison between calculated data from SHIELD-HIT v2 and Geant4 [Wilkens06] obtained for the carbon beam of 240MeV/u in water.

The comparison of the SHIELD-HIT v2 with the widely used Monte Carlo code GEANT4 is presented in Figures 25-28. The depth dose deposition of a ^{12}C beam with energy of 240MeV/u in water is shown in Fig. 25. The dose profiles obtained from the primary particles are compared with those from the total particle spectra. The position of the Bragg peaks obtained from the SHIELD-HIT v2 and GEANT 4 is shifted by 2.5mm and their height differs about 6.7%.

The contribution of the secondary particles to the total dose deposition is shown in Fig.26. The largest difference between the calculations with two codes shows up in the contribution of Li fragments (29%).

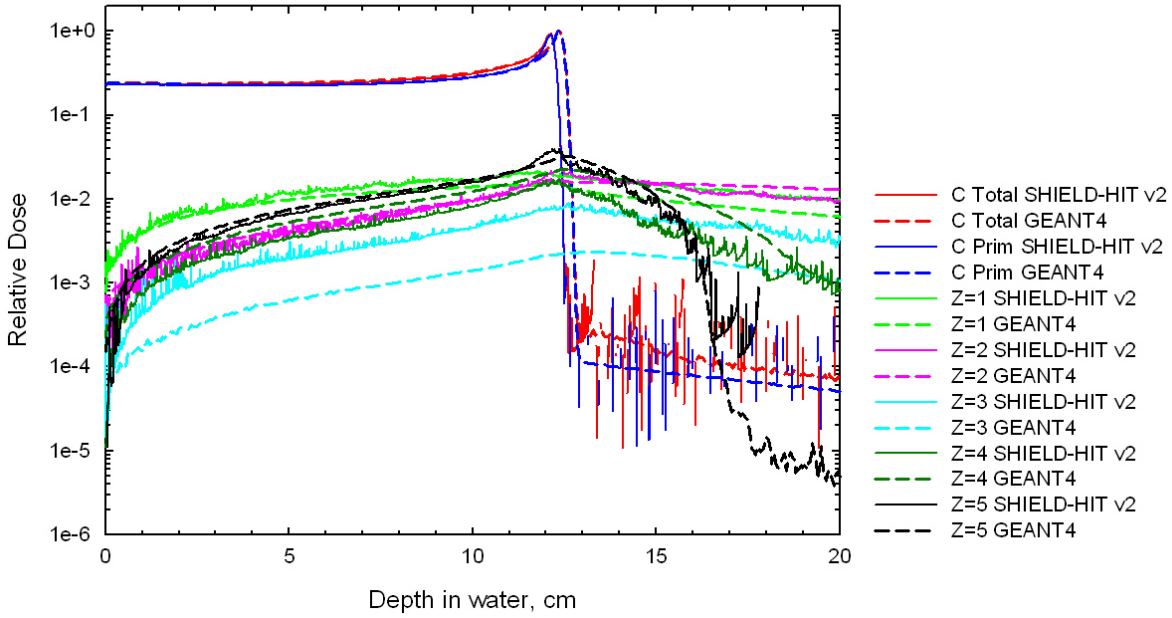

Figure 26 Contribution to the total dose deposition from secondary particles. Calculation was done for the carbon beam energy of 240MeV/u in water by SHIELD-HIT v2 and Geant4.

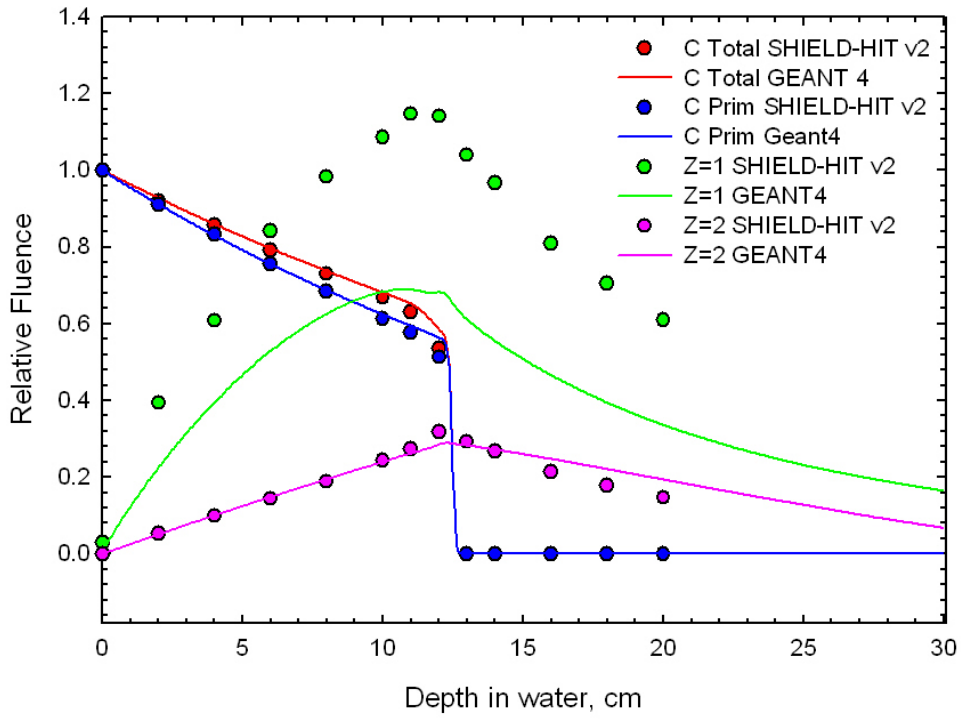

Figure 27 Fluence of primary (Z=6) and light fragments (Z=1, 2) relative to the incident particle fluence as a function of depth in water produced by an incident carbon beam of 240Mev/u.

Figures 27 and 28 compare spectra of primary and secondary particles calculated with SHIELD-HIT v2 and GEANT4 as a function of depth. All spectra are normalized to the statistics in Monte Carlo simulation (i.e. initial number of projectiles). In Figure 27 the attenuation of a primary carbon beam of energy 240MeV/u is plotted together with the fragment spectra of proton and alpha particles. The calculations from SHIELD-HIT v2 and GEANT4 coincide, only the proton production shows considerable differences: at the depth of 12cm SHIELD-HIT v2 yields 1.2 of the relative proton fluence while GEANT4 produces only 0.8 of normalized fluence. In Fig. 28 the distribution of heavier secondary particles is presented (Li, Be, B). The biggest difference appears for Li ions: at 12 cm depth SHIELD-HIT v2 yields fluence three times higher than GEANT4.

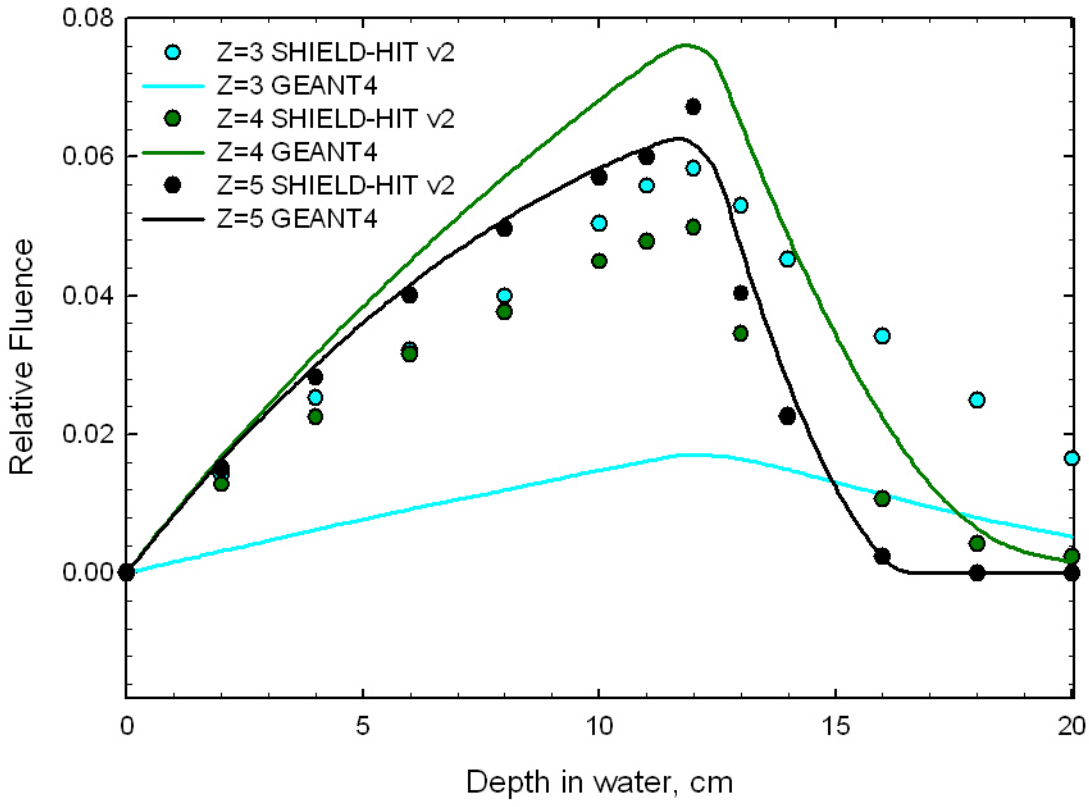

Figure 28 Fluence of intermediate fragments (Z=3-5) relative to the incident particle fluence as a function of depth in water produced by an incident carbon beam of 290Mev/u.

A number of angular distributions of fluences differential in energy of light fragments from a carbon beam of 200MeV/u in water are depicted in Fig.29 and Fig.30. The experimental data [Gunzert04] are compared with SHIELD-HIT v1 and SHIELD-HIT v2 simulations.

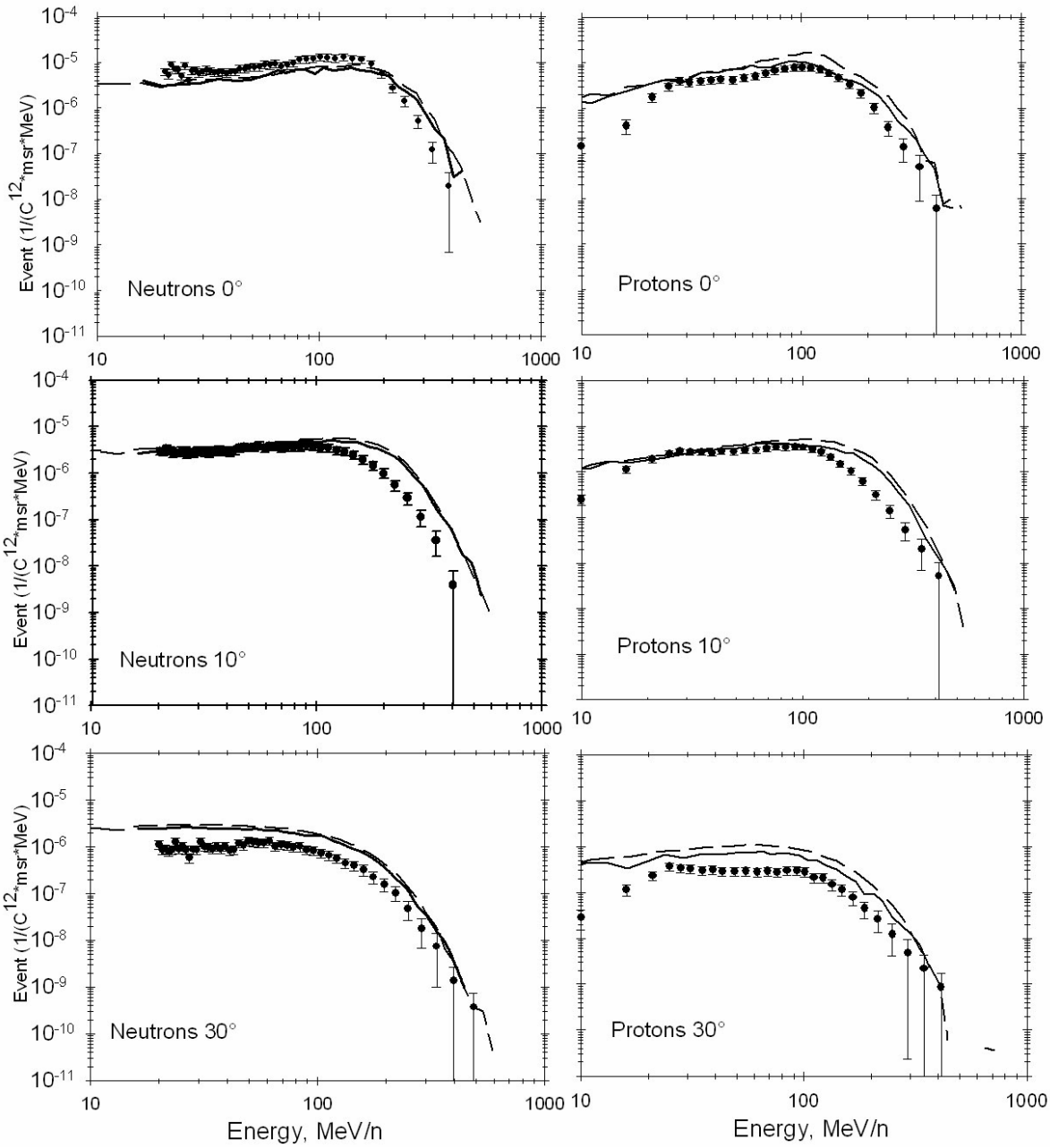

Figure 29 Fluence differential in energy of light fragments (neutrons and protons) for ^{12}C with initial energy of 200MeV/u after passing 12.78 cm of a water phantom. The angular distribution of secondary particles was measured at GSI [Gunzert04] (circles) and is compared with SHIELD-HIT v2 (solid line) and SHIELD-HIT v1 (long dash line) calculations.

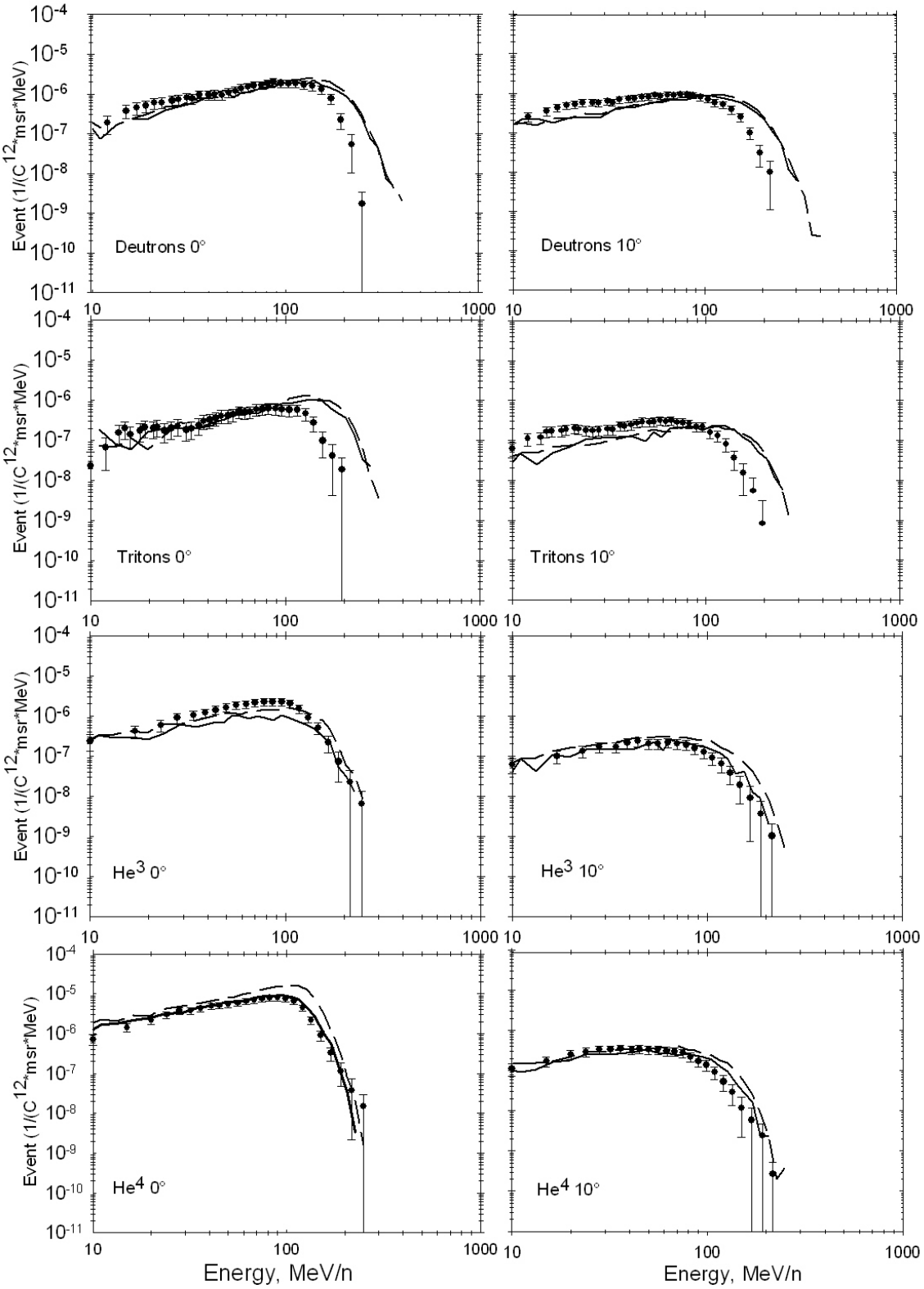

Figure 30 Fluence differential in energy of light fragments (deuterons, tritons and He ions) for ^{12}C with initial energy of 200MeV/u after passing 12.78 cm of a water phantom. The angular distribution of secondary particles was measured at GSI [Gunzert04] (circles) and is compared with SHIELD-HIT v2 (solid line) and SHIELD-HIT v1 (long dash line) calculations.

3.1.5 Lateral Profiles of a Scanning Beam; SOBP

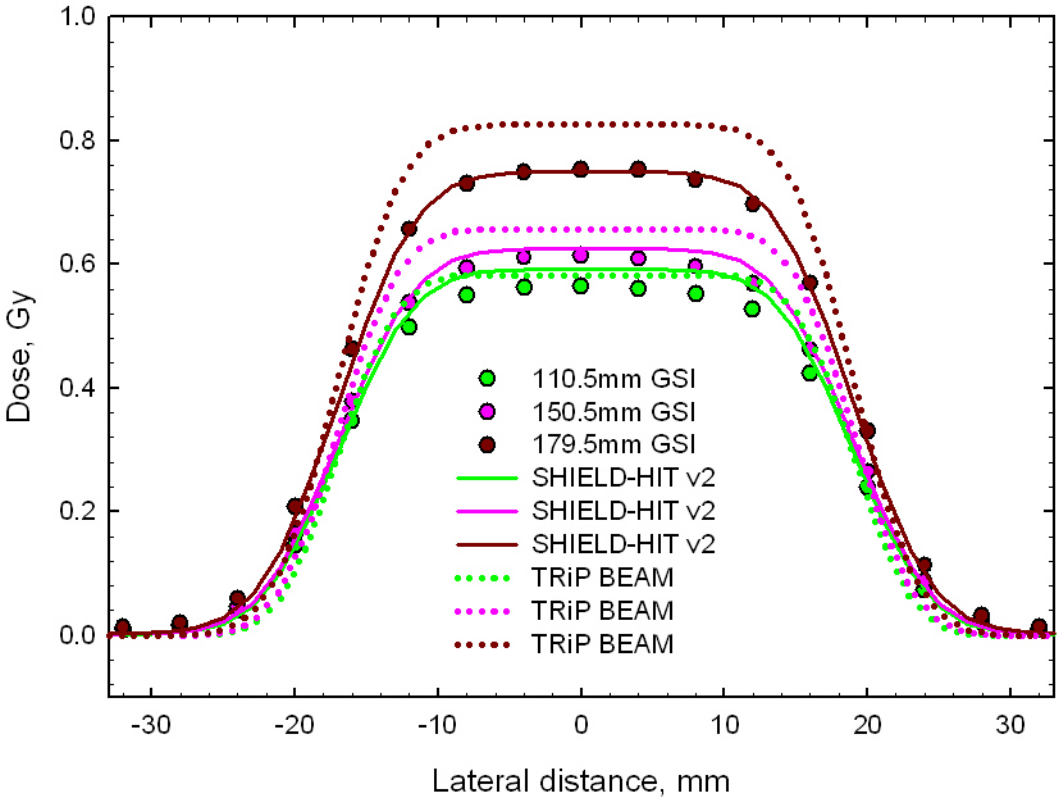

Figure 31 Lateral profiles of a scanning beam in plateau region. Measured spread-out peak from carbon beam is compared with calculations done with SHIELD-HIT v2 and TRiP BEAM.

Figures 31-33 present the measurements carried out at GSI with a scanning carbon ion beam in water and simulations made with SHIELD-HIT v2 [Jäkel06] and TRiP BEAM[19] [Krämer06]. The detailed description of the experiment and the experimental setup is given in paragraph 2.7.

Figures 31, 32 and 33 show the lateral profiles at the plateau (110.5mm, 150.5mm and 179.5mm), peak (190.4mm, 200.4mm and 205.4mm) and tail (220.4mm, 230.4mm and 240.4mm) regions respectively. In the plateau region (Fig.31) the maximum deviation is observed for TRiP BEAM calculations and exceeding the experimental data by up to 10%. At the spread-out peak position or so-called target region (Fig.32), SHIELD-HIT v2 reproduces the profiles very well while TRiP BEAM overestimates the deposited dose up to 16.6%. At the fragments' tail region TRiP BEAM reproduces the measurements better,

[19] TRiP BEAM is a modified version of treatment planning program TRiP developed at GSI, which includes angular scattering and improved fragmentation model.

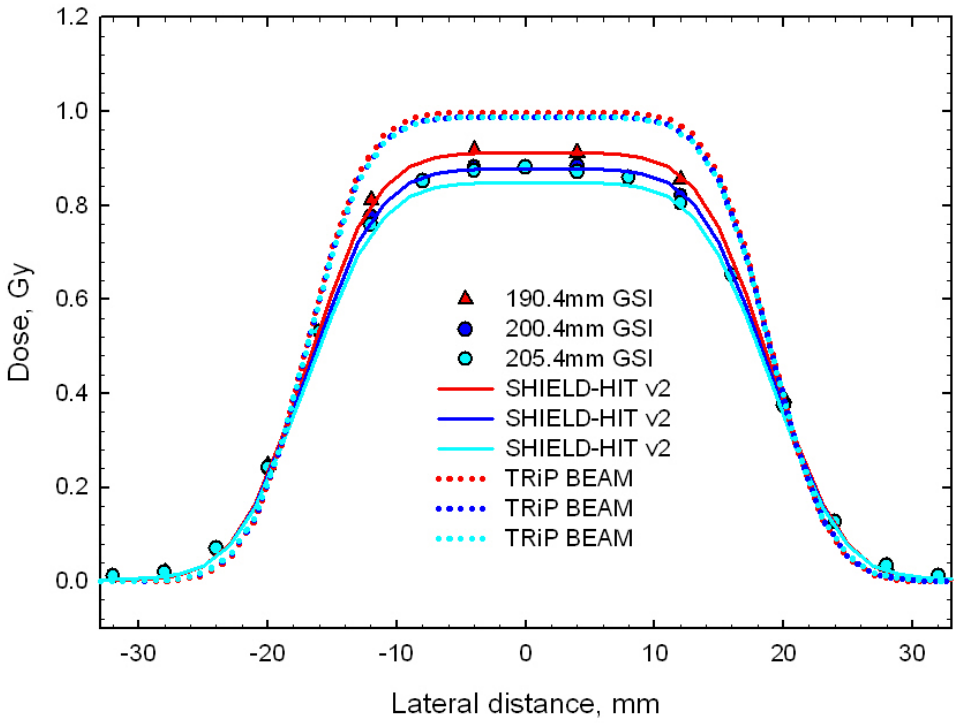

Figure 32 Lateral profiles of the scanning beam in Bragg peak region. Measured spread-out peak from carbon beam is compared with calculations done with SHIELD-HIT v2 and TRiP BEAM.

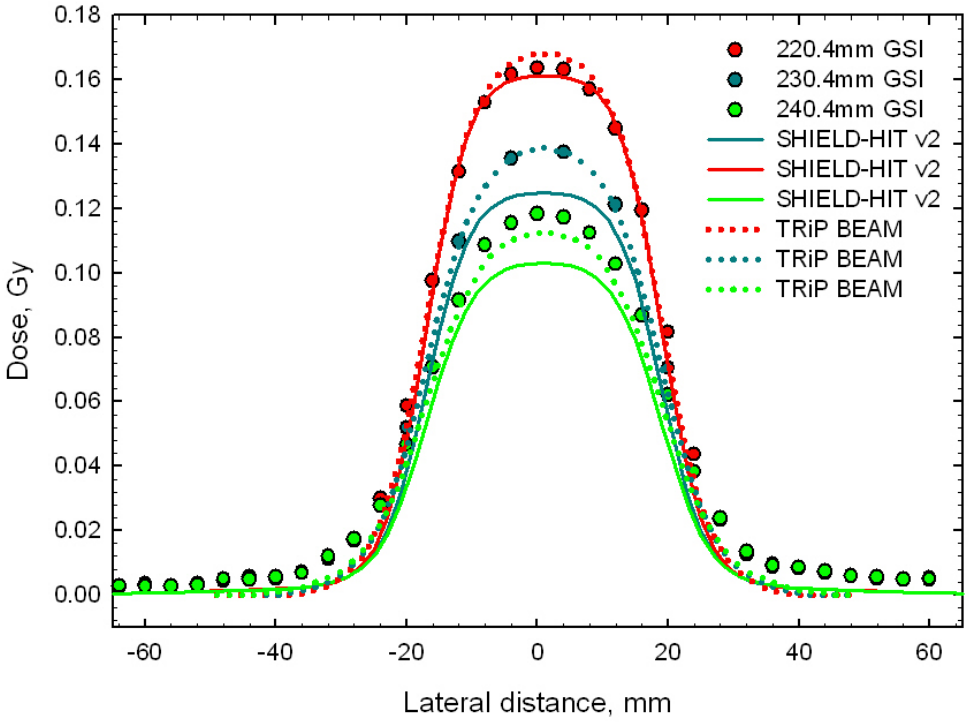

Figure 33 Lateral profiles of the scanning beam in fragments tail region. Measured spread-out peak from a carbon beam is compared with calculations done with SHIELD-HIT v2 and TRiP BEAM.

while SHIELD-HIT v2 underestimates the dose deposition (Fig.33). Thus, at the last point of measurements (240.4mm depth in water) TRiP BEAM calculates 4.5% less dose while SHIELD-HIT underestimates the deposited dose by up to 12.7%.

The contribution of the secondary particles to the total dose deposition in the lateral beam profiles is plotted in Figures 34-36. The importance of carbon, helium, boron and protons is analyzed in plateau, peak and tails regions. In order to see better the influence of the fragments, the dose axis in every chosen depth of interest is plotted 2 times: in linear (Top) and logarithmic scale (Bottom). In the plateau region (see Fig.34) more then 84% of the deposited dose is contributed by carbon ions[20], boron contributes up to 6.8% and about 4% comes from protons and alpha particles. In the spread-out Bragg peak, (see Fig.35) the contribution of carbon ions to the total dose yields 84%. Boron contributes 9%, He 4.3% and protons contribute 2.2%. In the fragments' tail, there is no projectile left any more and the main contribution to the dose comes from boron (35%) and helium (26%) (see Fig.36).

[20] The contribution in % is calculated for the lateral distance of 0mm.

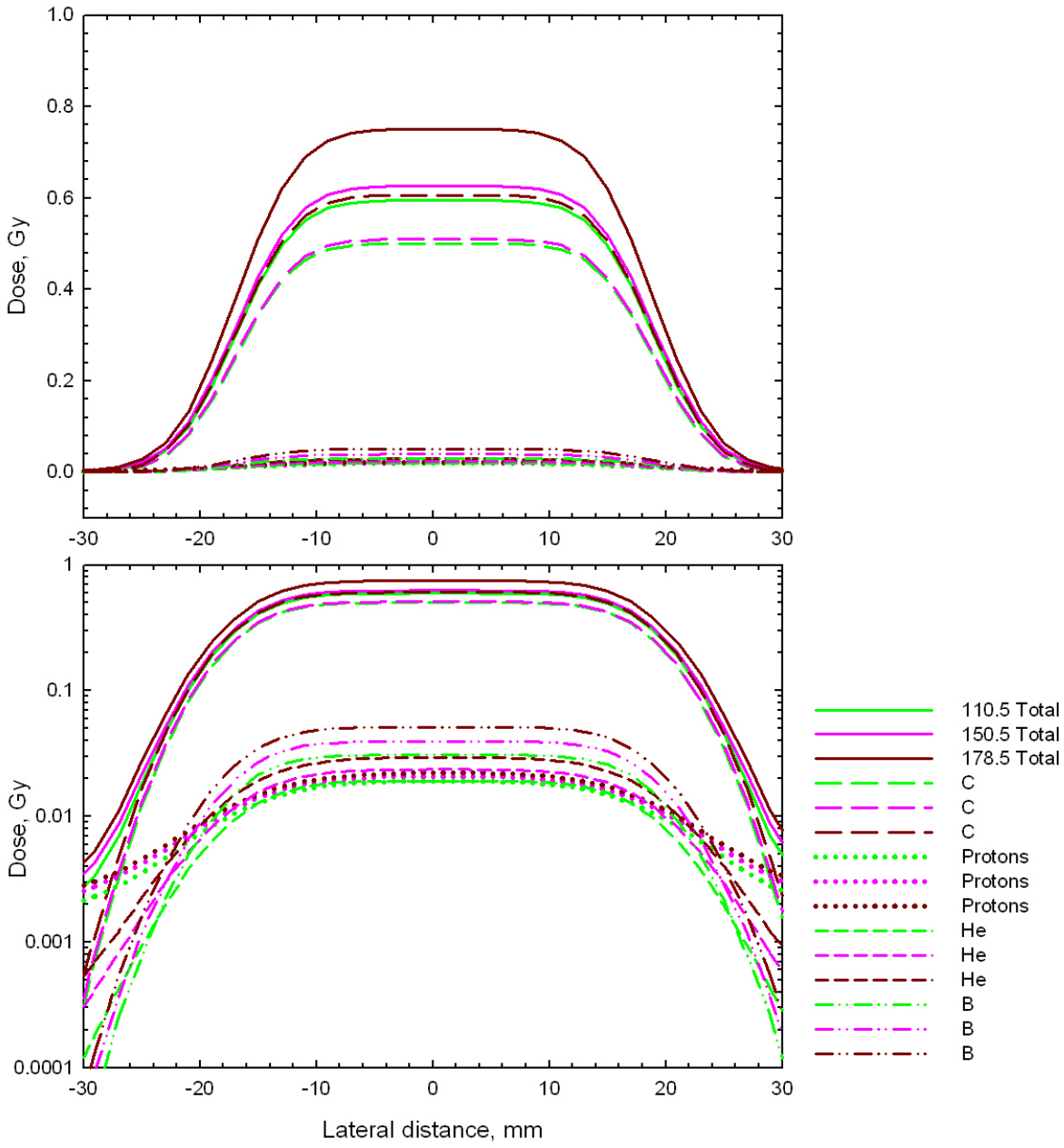

Figure 34 Contribution of carbon ions and secondary particles to the total dose deposition in the plateau region. The lateral profiles of the carbon beam in water are calculated with SHIELD-HIT v2.

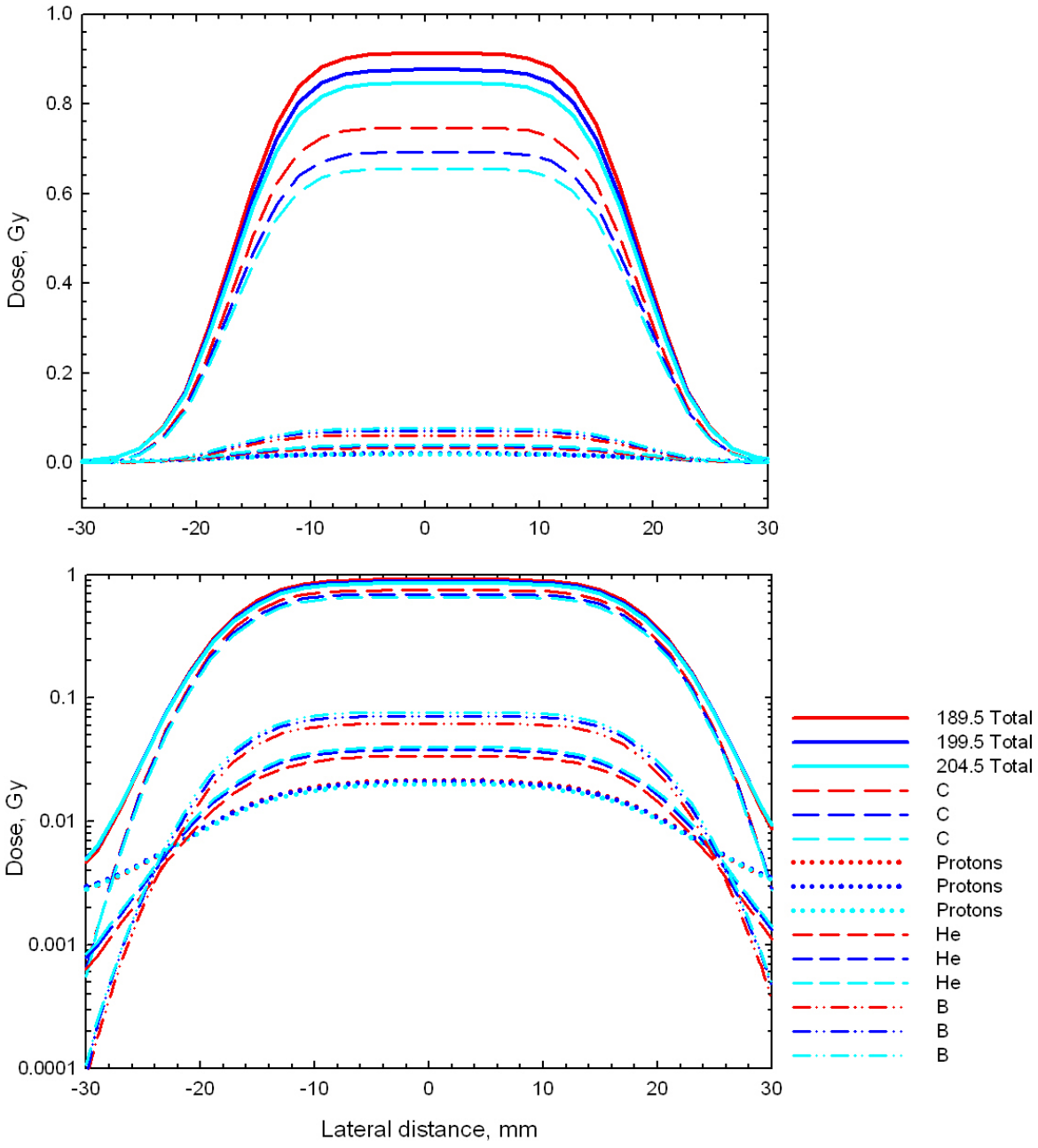

Figure 35 Contribution of carbon ions and secondary particles to the total dose deposition in the Bragg peak region. The lateral profiles of the carbon beam in water are calculated with SHIELD-HIT v2.

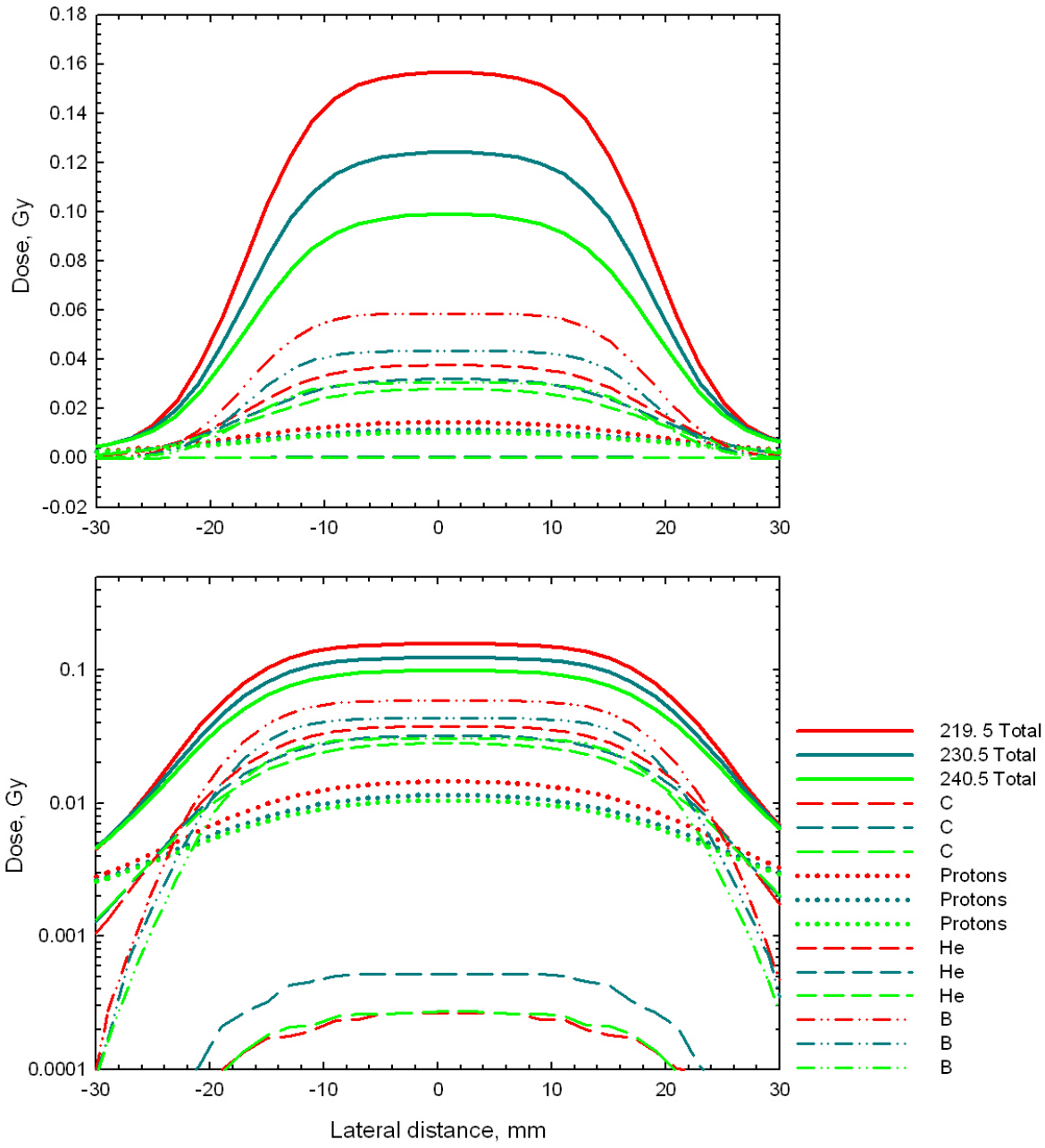

Figure 36 Contribution of carbon ions and secondary particles to the total dose deposition in the fragments' tail region. The lateral profiles of the carbon beam in water are calculated with SHIELD-HIT v2.

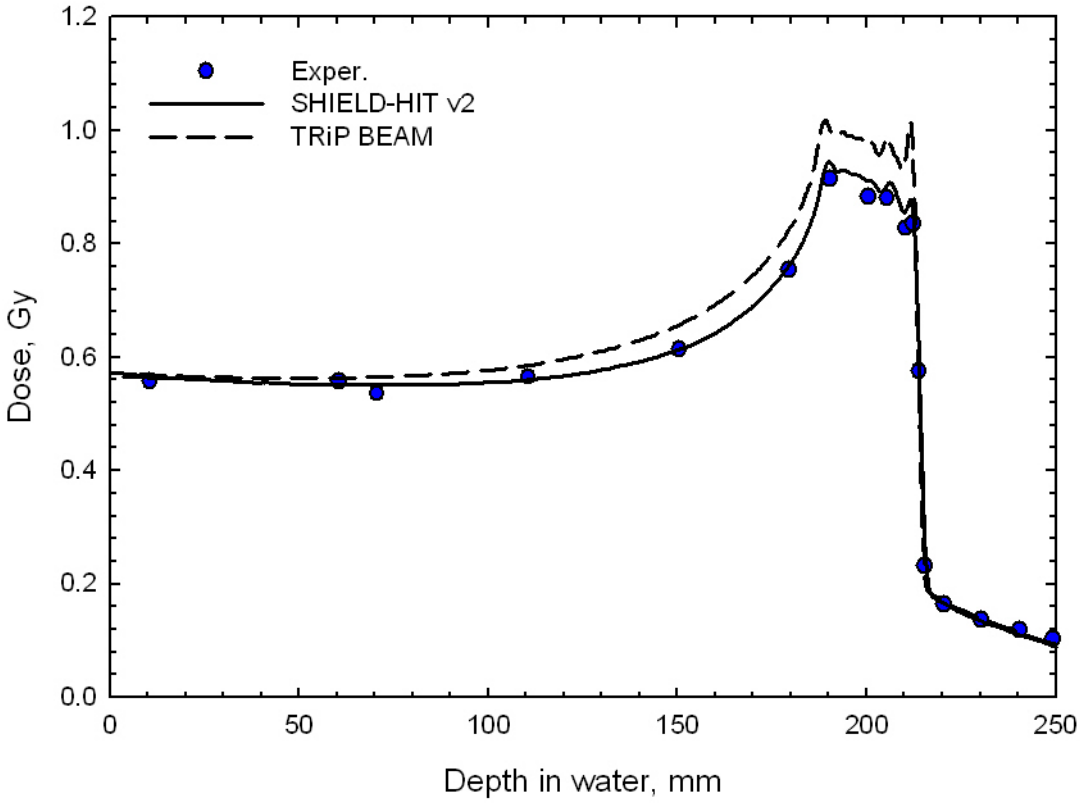

Figure 37 Comparison of a spread-out Bragg peak measured at GSI with calculations done by SHIELD-HIT v2 and TRiP BEAM [Krämer06].

The comparison of a spread-out Bragg peak measured at GSI (see paragraph 2.7) and calculated with SHIELD-HIT v2 and TRiP BEAM [Krämer06] is plotted in Fig.37. The TRiP BEAM code overestimates the deposited dose on 10% in plateau and 16% in target region.

3.2 Calculation of Stopping Power Ratios for Heavy Ions dosimetry

3.2.1 Calculation of STPR using Stopping Power Data from ICRU reports

Figure 38 shows the ratio of stopping power data for carbon ions in water as a function of energy. The data are taken from different sources and divided by those from ICRU-73. At the energy of 1Mev/u the unmodified Bethe-Bloch equation (in SHIELD-HIT v1) yielded a result, which deviates 40% from the state-of-the-art ICRU data, while the modified version of the formula reproduces the data with deviation from the ICRU-73 reference data of only 2%. MSTAR and SHIELD-HIT v2 reproduce the stopping power data at low energy of 60keV/u with a deviation of 25% from the standard data.

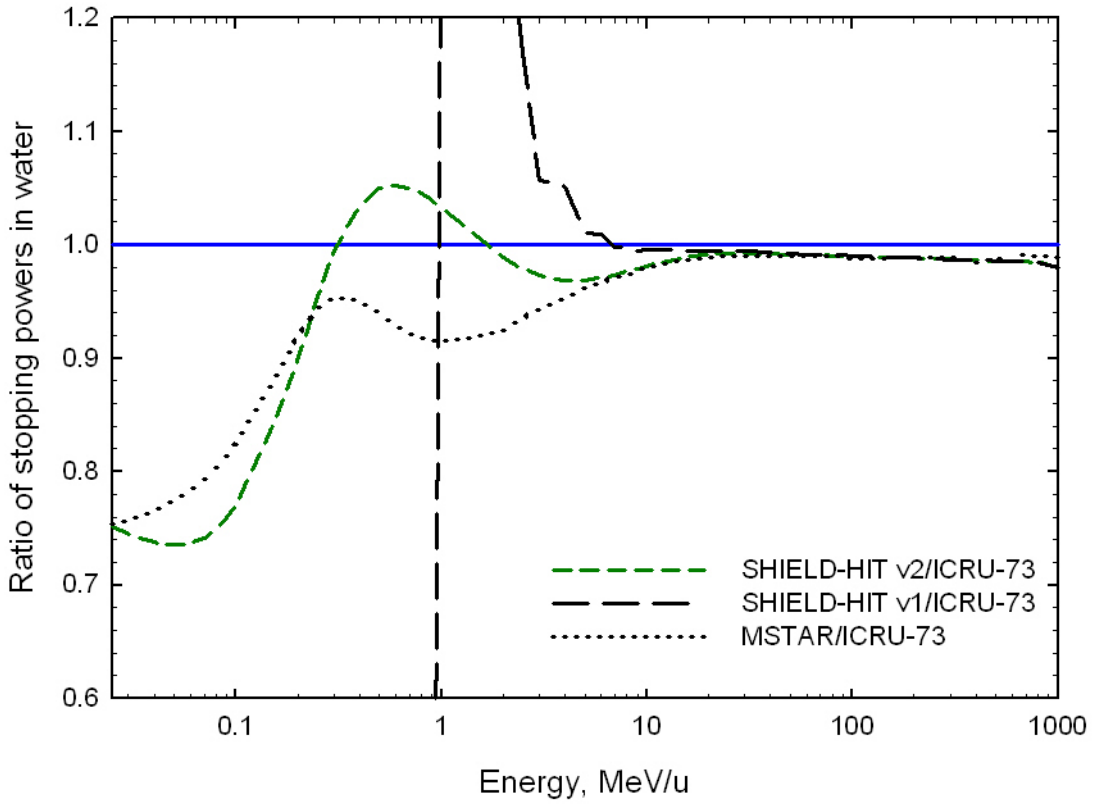

Figure 38 Ratio of stopping power values from different sources to those from ICRU-73 [ICRU05] for carbon in water, as a function of the energy. The dotted line is for MSTAR [Paul02] data; dashed lines are for SHIELD-HIT v1 (long dash) and v2 (short dash) using the original and the modified Bethe-Bloch formula respectively.

Subsequent to the fluence distributions and the dose deposition by track-ends derived from the Monte Carlo simulations, calculations of the stopping power ratios $s_{w,air}$ as a function of depth in water were carried out using equation (2.3.2.1). The corresponding results are shown in Fig.39. Nine different initial beam energies between 50 and 450 MeV/u were considered, which are compared with the IAEA TRS-398 recommended constant value of 1.130. The obtained stopping power ratios for the plateau region differ by approximately 0.5%-1%, respectively for 400 MeV/u and 50 MeV/u beams. The distributions show a maximum for all initial energies, which is situated at the distal fall-off of the Bragg peak for the corresponding energy (see Fig.42). In the investigated energy range, the maximum difference of 2.35% in the peak to the recommended value of 1.13 appears for an initial energy of 50MeV/u.

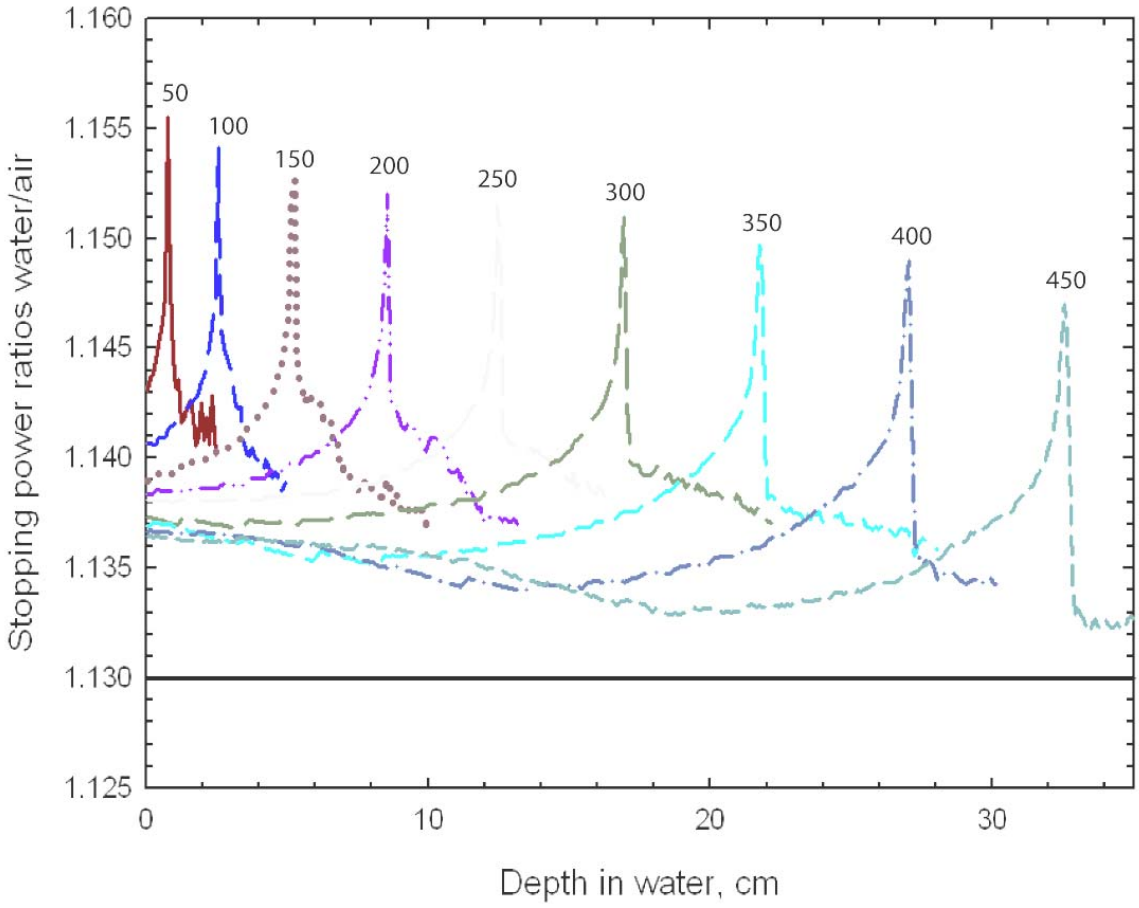

Figure 39 Monte Carlo calculated values of the water/air stopping power ratio for a carbon beam as a function of the depth in water for carbon beams with initial energies between 50MeV/u and 450MeV/u. The solid line at 1.130 corresponds to the constant $s_{w,air}$ value recommended by IAEA TRS-398.

The influence of the produced fragments on the stopping power ratio, calculated using primary particles ^{12}C only is presented in Fig.40. In order to investigate the role of the secondary particles in total stopping power ratio, the highest beam energy (450MeV/u), relevant for the medical application was chosen, where the most fragments are produced. The biggest deviation is caused by ^{4}He (up to 4.2%) and ^{3}He (up to 0.8%) particles.

A comparison between the stopping power ratio calculated using only primary ^{12}C particles and the whole particle spectra for a primary beam energy of 450MeV/u is presented in Fig.41. Fragments decrease the stopping power for primary particles by 0.5% in the plateau and by 0.9% in the peak region.

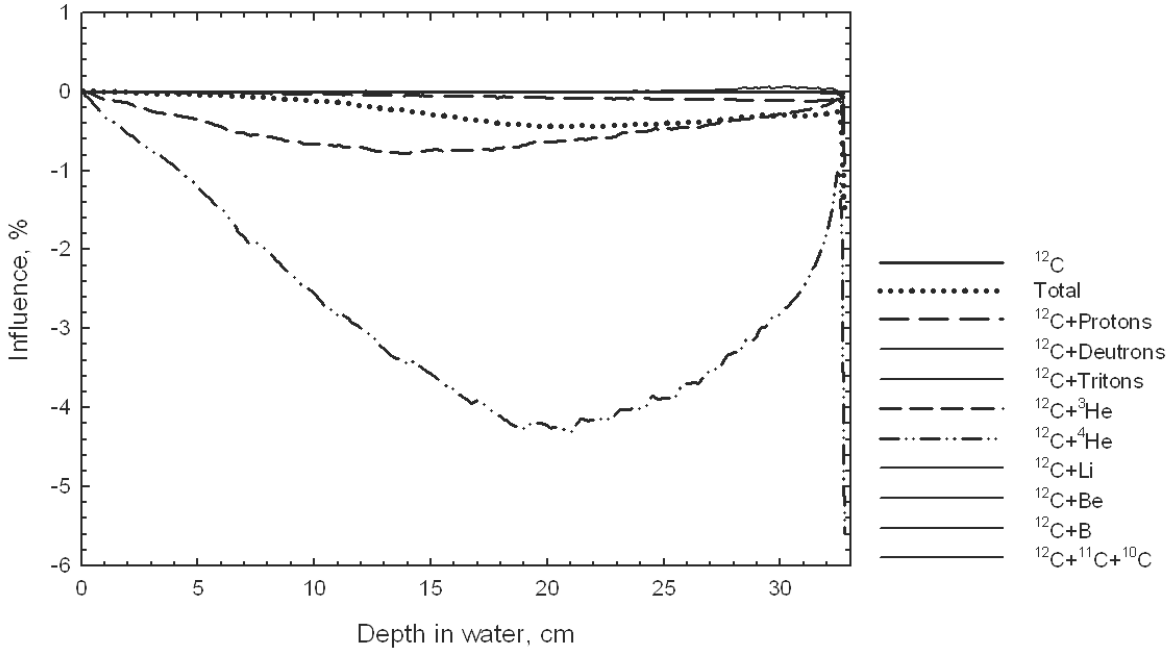

Figure 40 Deviation of $s_{w,air}$ for the produced fragments from the value for ^{12}C alone with initial energy of 450MeV/u.

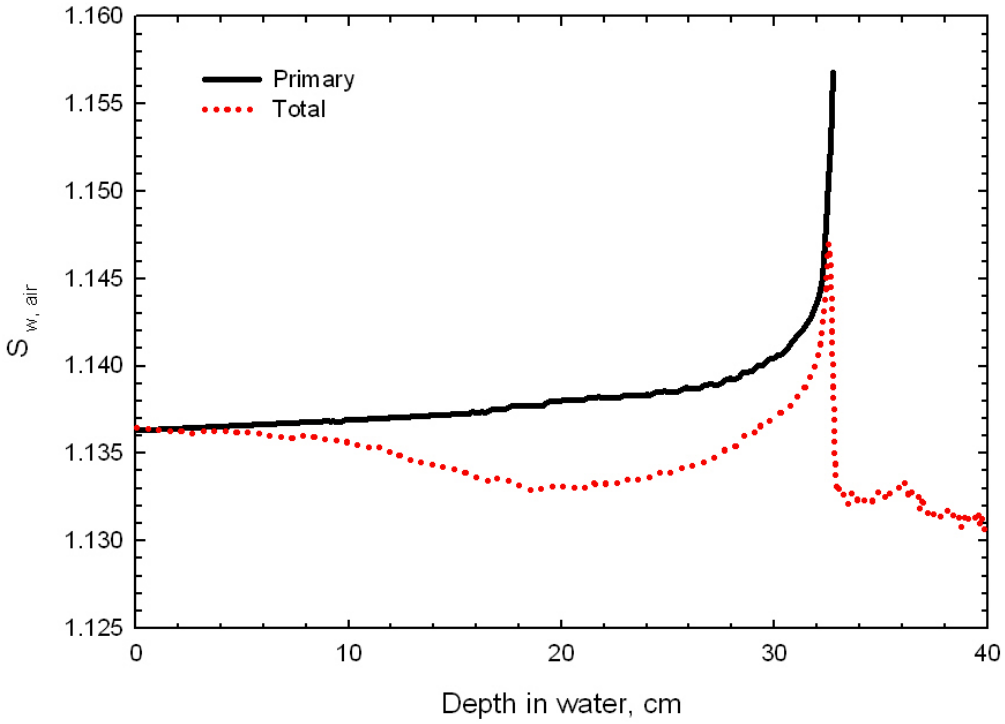

Figure 41 Comparison of the stopping power ratio calculated just for primary ^{12}C ions with a calculation for the whole spectrum of primary and secondary particles. The calculation is done with SHIELD-HIT v2.

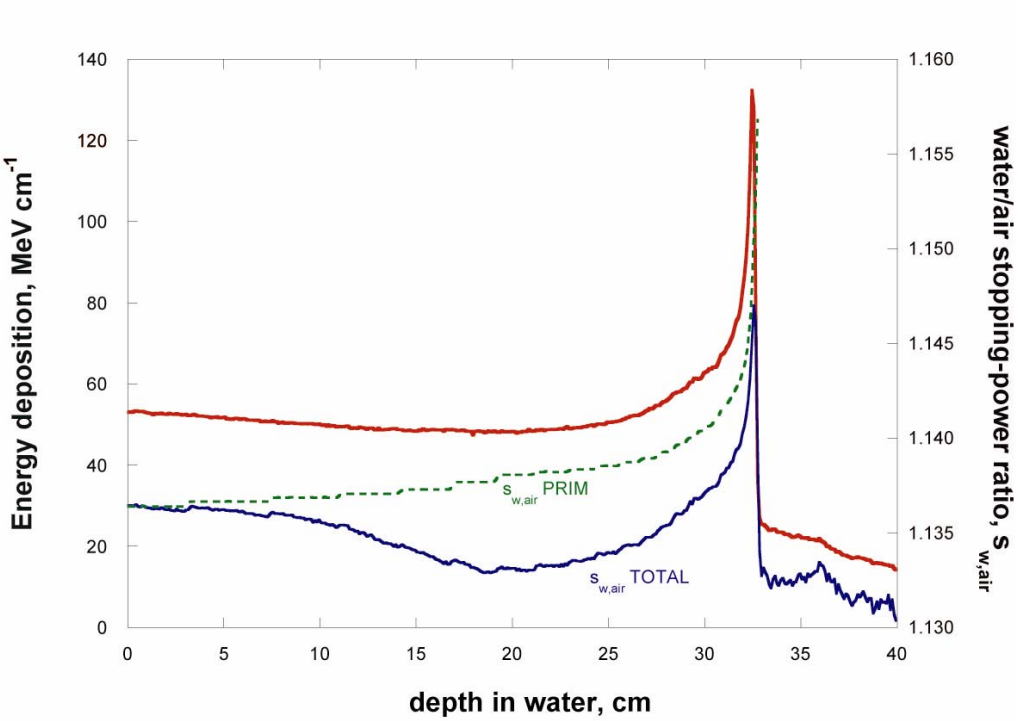

Figure 42 Peak position of the stopping power ratio (blue solid line) relative to the position of the Bragg peak of corresponding primary energy of 450MeV/u (red solid line).

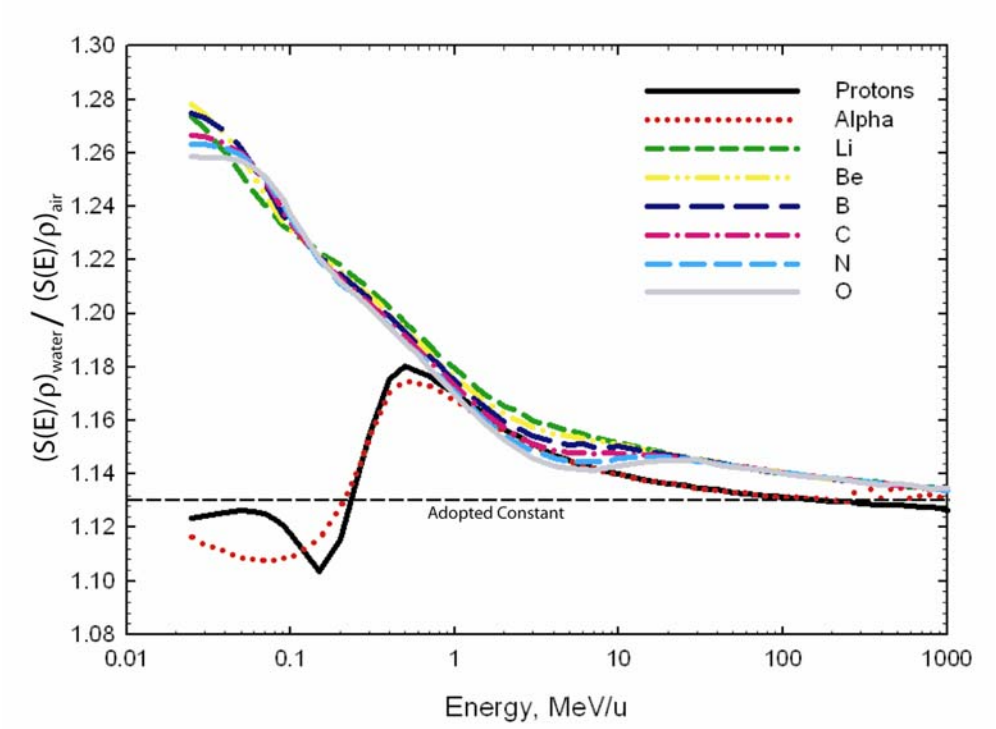

Figure 43 Ratio of the stopping powers water to air from ICRU-49 [ICRU93] for protons and alpha particles and ICRU-73 for heavier ions [ICRU05].

Figure 42 depicts the position of the peak in the stopping power ratio for ^{12}C of 450MeV/u relative to the Bragg peak of corresponding energy. It should be noted, that the left and right Y axes have a different scale.

The ratios of stopping powers[21] (not to confuse with direct stopping power ratio) for all particles from protons up to carbon ions are plotted in Fig.43. The data for the stopping power for protons and alpha particles are taken from the ICRU-49 report [ICRU93] and for heavier ions from ICRU-73 report [ICRU05]. One can see that for the energy range from 10MeV/u up to 1000MeV/u the difference between the values for protons, He ions and heavier ion makes up 0.9%. The difference becomes bigger for the energy from 1Mev/u and below. At 25keV/u the deviation between the ratios of stopping powers for protons, alpha particles and heavier ions put together add up to 14%.

The total stopping power ratios of different ions are presented in Fig. 44. All calculations were done using ICRU stopping power data. The chosen maximum energy for every type of particles corresponds to the maximal depth of penetration (25cm), relevant for the medical application. All calculated stopping power ratios are compared to the adopted constant 1.13 recommended by TRS-398 [IAEA00]. The maximum deviation (up to 4.6%) from the adopted constant for an initial energy of 50MeV/u is caused by following projectiles: ^{7}Li, ^{11}Be and ^{14}N. The influence of fragments can be followed well for the light (^{7}Li) and heavier (^{16}O) projectiles. As it was already shown in Fig.41, the fragments influence the stopping power ratio the most in the peak region, lowering its value. Thus, for the highest energy for ^{7}Li the maximum deviation of the $s_{w,air}$ from the adopted constant makes up 2.3% while for the ^{16}O of highest energy it is just 1.5%.

[21] A ratio of stopping powers is a direct ratio of mass stopping power data water/air: $\frac{(S(E)/\rho)_{water}}{(S(E)/\rho)_{air}}$

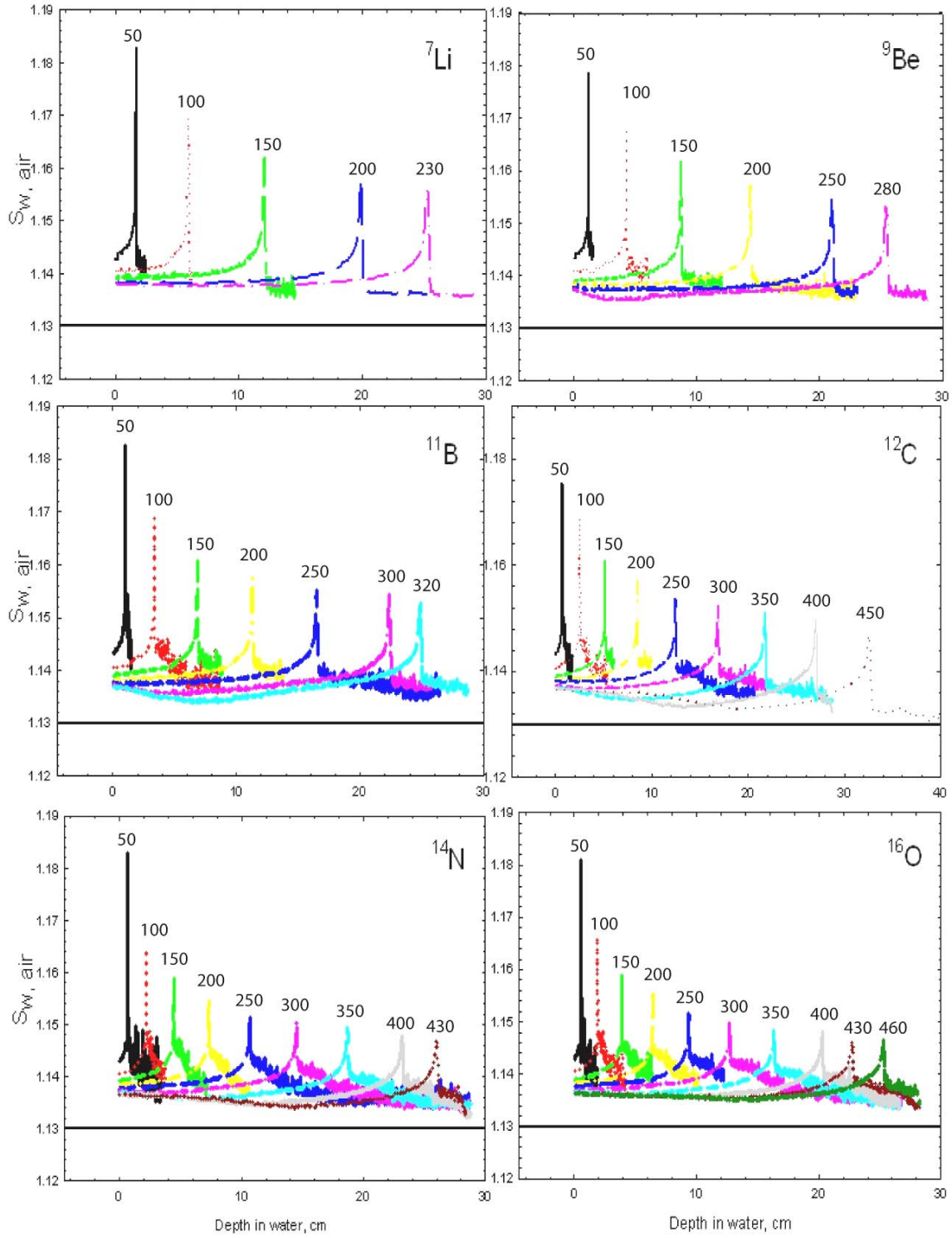

Figure 44 Monte Carlo calculated values of the water/air stopping power ratio for different ion beams as a function of the depth in water. The solid line at 1.130 corresponds to the constant $s_{w,air}$ value recommended by IAEA TRS-398.

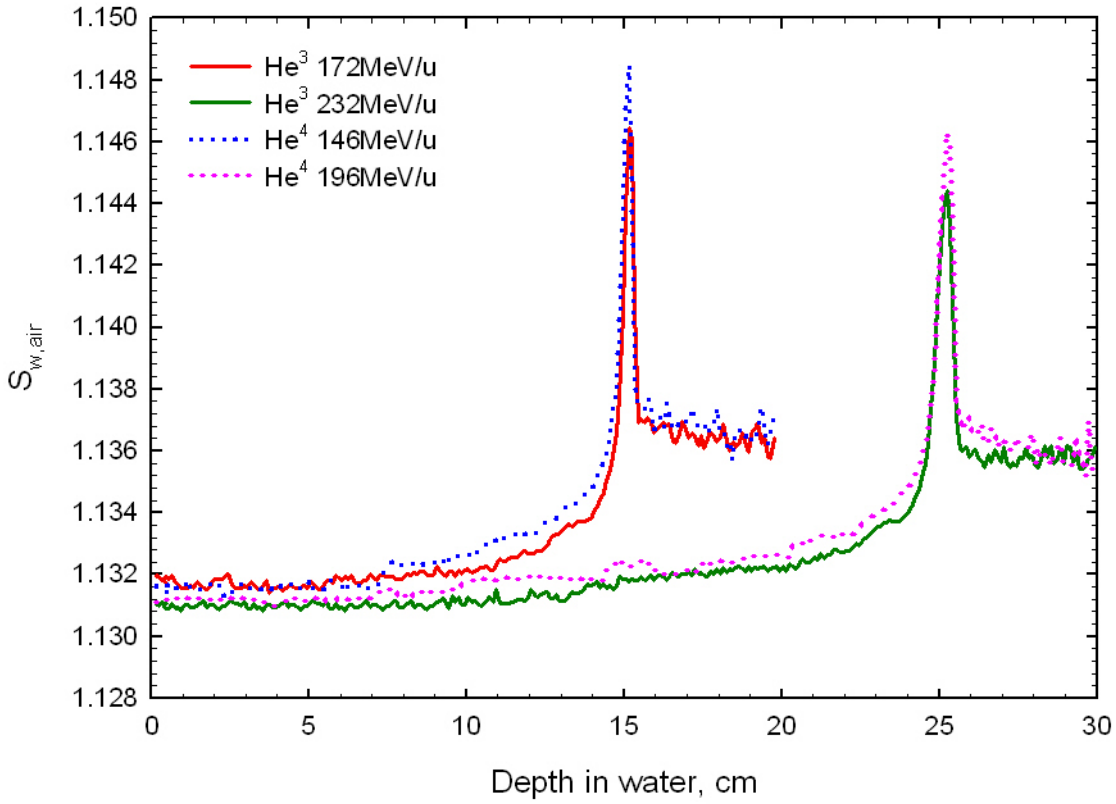

Figure 45 Comparison of Monte Carlo calculated stopping power ratios for ^{3}He and ^{4}He.

As ^{3}He and ^{4}He ions are considered as future promising candidates for hadron therapy, calculations of the corresponding stopping power ratios and comparisons were done. The results are presented in Fig.45. The energies for both isotopes were chosen to obtain a peak maximum at 15 and 25cm depth in water. The difference in the height of the stopping power ratio peaks makes up 0.2%

3.2.2 Calculation of STPR using BEST stopping power data with different I-values

The last aspect in the calculations of different stopping power ratios was to investigate the influence of the I-value on the results [Paul06]. The ratios of stopping powers water/air are plotted in Fig.46. The data for stopping powers with different I-values were taken from different sources and compared with the adopted constant of 1.13, recommended by TRS-398. The maximum deviation from the adopted constant for all values appears at low energies (corresponds to the Bragg peak). For the higher energies the ratio of stopping powers taken from SRIM differs the most (1.2%).

Table 4 presents the I-values used in the stopping power data for water and air in different sources. Though the I-value is material dependent, one can see that within ICRU reports for different ions for water and air it is not consistent. Thus, for the air from ICRU-49 and

ICRU-73 it deviates on 3eV while for the water from the same reports the deviation makes up 8eV.

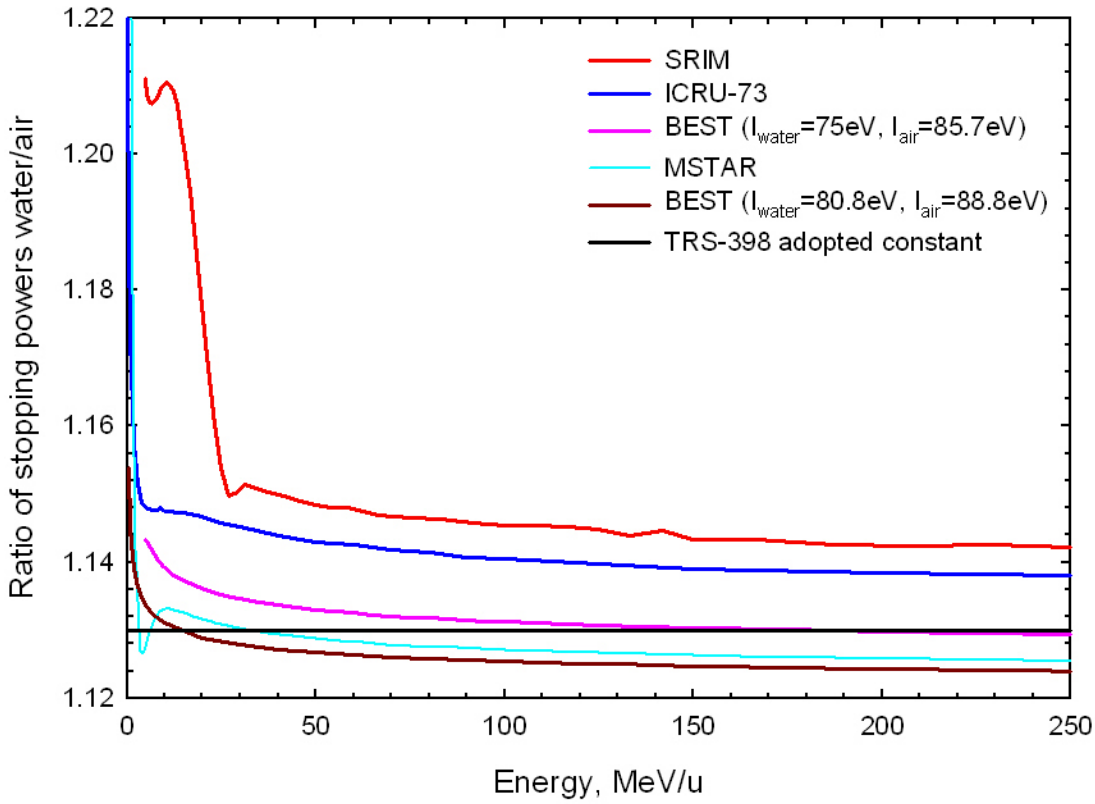

Figure 46 The ratio of the stopping powers water to air for carbon ions using different data for stopping powers versus the adopted constant proposed by TRS-398 [IAEA00].

Table 4 *I*-values for water and air, obtained from the values for constitutes (see equation (2.3.2.4)), from different sources.

Reference	*I-value* for water, (eV)	*I-value* for air (eV)
ICRU-37, ICRU-49	75.0 ± 3	85.7
ICRU-73	67.2	82.8
[Paul06B]	80.8 ± 2	88.8 ± 3

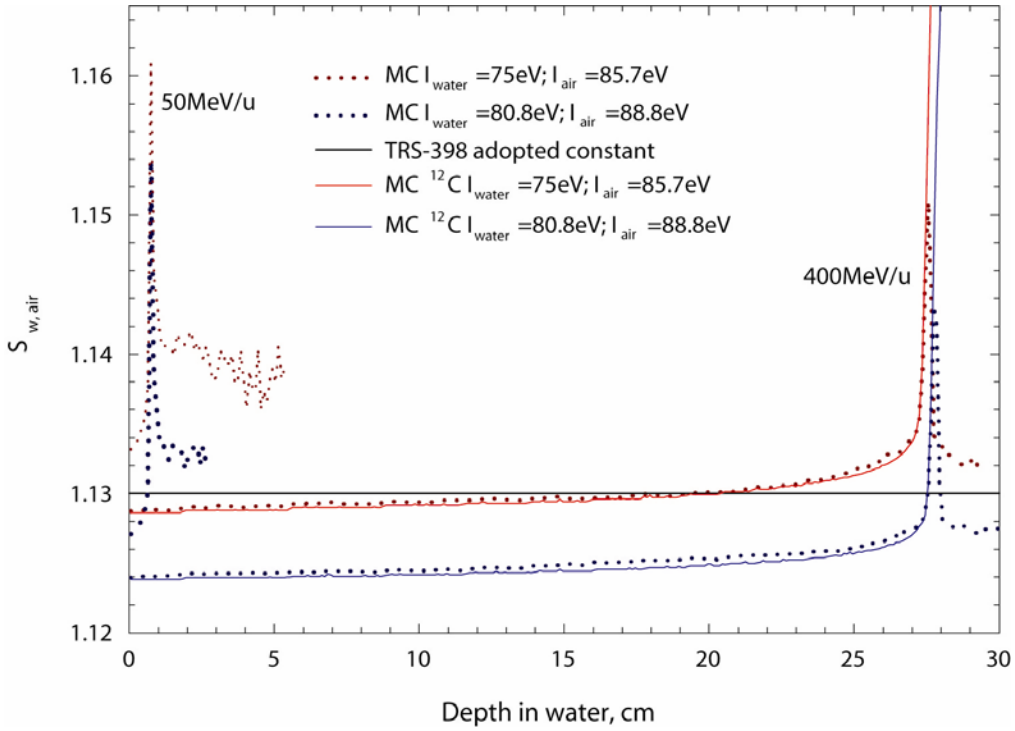

Figure 47 The stopping power ratio for ^{12}C of 400MeV/u calculated with SHIELD-HIT v2 using different I-values in stopping power data from BEST. The stopping power ratios calculated for the primary particles only (solid line) are compared with those calculated for the whole spectrum (dotted line) and TRS-398 adopted constant.

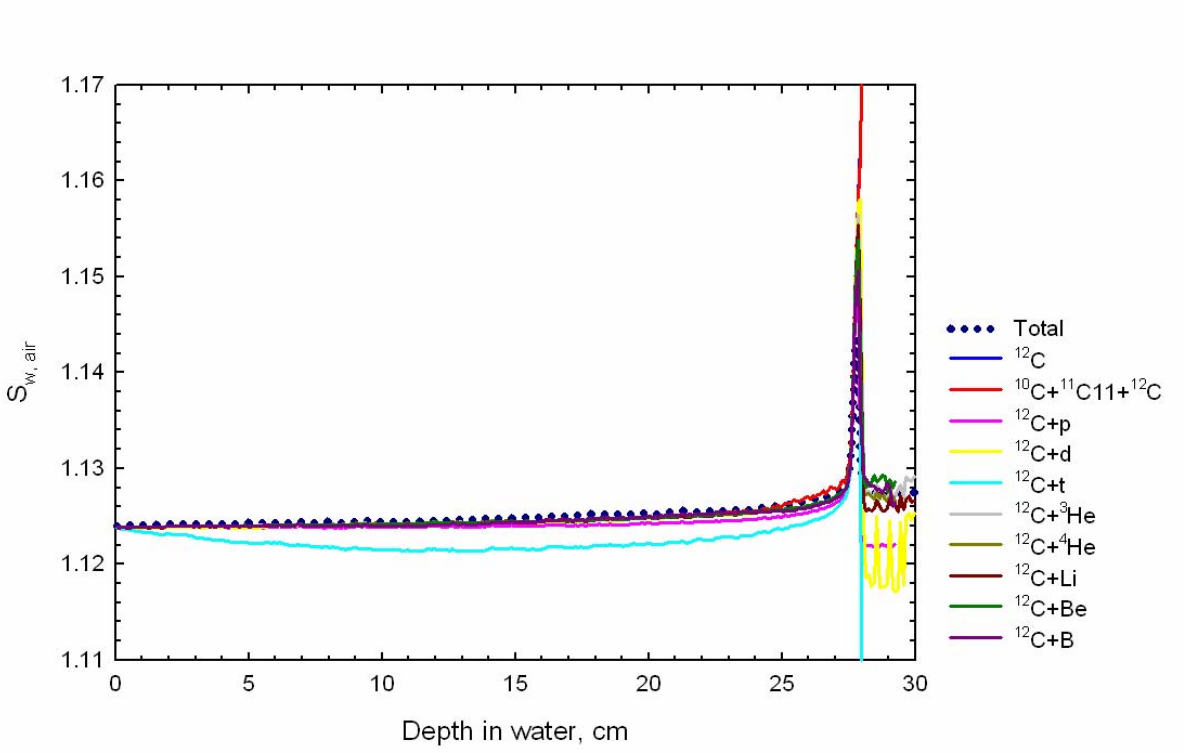

Figure 48 Contribution of the fragments to the stopping power ratio calculated with SHIELD-HIT v2 for a primary ^{12}C beam of 300MeV/u.

The stopping power ratios calculated with SHIELD-HIT v2 for a carbon beam of 400MeV/u only for primary particles and for the whole particle spectra are plotted in Fig.47. The stopping power data used for the calculation were taken from BEST and had different I-values for water and air. In one case the I-value for water was 75eV and for air 85.7eV and in another for water was 80.8eV and for the air 88.8eV. It can be seen that for the higher initial energy (400MeV/u) the maximum deviation in the peak from the adopted constant makes up 1.8% for ionization potential I_{water}=75eV and 1.2% for I_{water}=80.88eV. In the case of lowest clinical energy (50MeV/u) it becomes more critical: 2.7% for I_{water} 75eV and 2.1% for I_{water}=80.88eV.

The contribution of the secondary particles to the stopping power ratio calculated just for primary carbon ions of 400Mev/u is shown in Fig.48. For the calculation BEST stopping power data were taken with following I-values: I_{water}=80.8eV and I_{air}=88.8eV. Tritium caused the maximum deviation (up to 10%) at the tail region.

3.3 Other Applications

3.3.1 Antiprotons

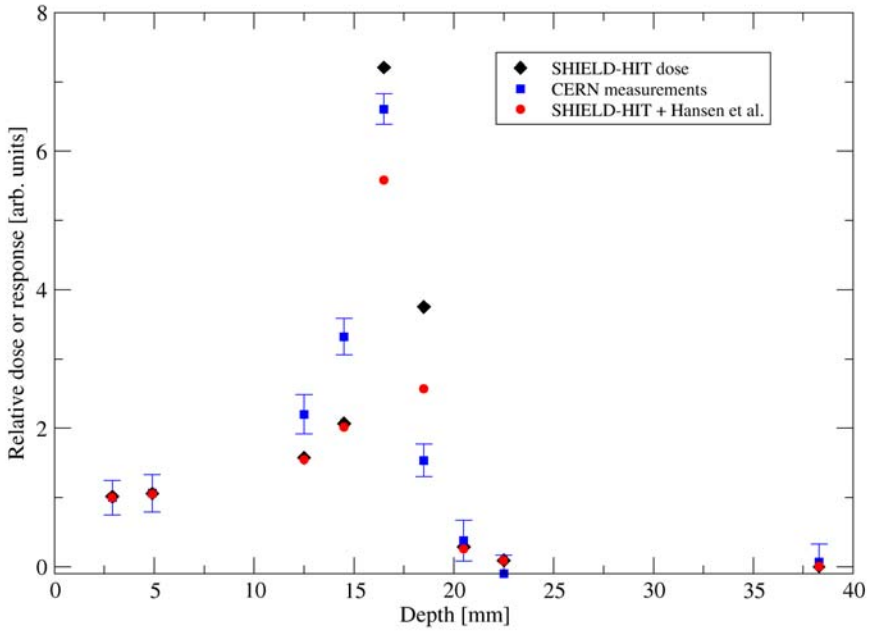

Figure 49 Depth dose deposition from the antiprotons of 47MeV in polystyrene cylinder measured with Alanine detectors and calculated with SHIELD-HIT v2.

The depth dose profiles for antiprotons with an energy of 47MeV are presented in Fig.49 and Fig.50. The measurements, done with Alanine detectors, are shown in Fig.49 and with TLD in Fig.50 [Bassler06]. The experimental data are compared with direct simulations performed with SHIELD-HIT v2 and model calculations, where SHIELD-HIT particle spectra were used. The measurements and calculations presented in the Figures are normalized on the entrance value. The simulations of the Alanine detector underestimate the measured dose in the plateau region (27%) and show contradictory results in the peak: SHIELD-HIT v2 overestimates the dose by 10.6% and the Hansel model underestimates by 17%.

The comparisons made for TLD in Fig.50 show good agreement for the MECLaT model calculations, while the SHIELD-HIT v2 calculated dose profile in the peak is three times in excess of the measured one.

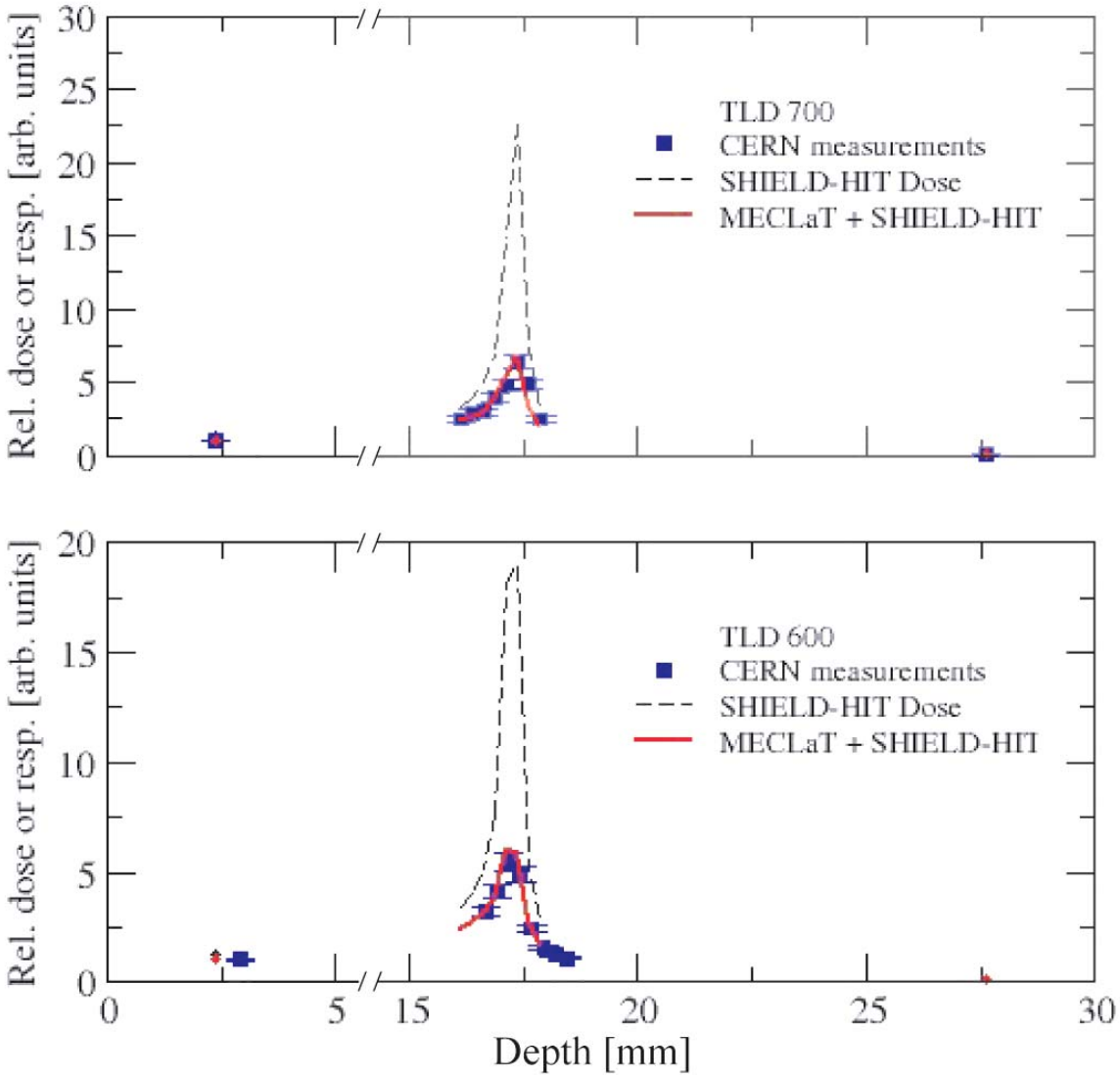

Figure 50 Depth dose deposition from the antiprotons of 47MeV in polystyrene cylinder measured with TLD700 and TLD600 and calculated with SHIELD-HIT v2.

3.3.2 Particle Transport in Low Density Medium; F-factor

To calculate the combined correction factor (F-factor), a realistic ionization chamber was simulated (see App.B). For this purpose a more accurate particle transport in air (cavity of the chamber) was necessary.

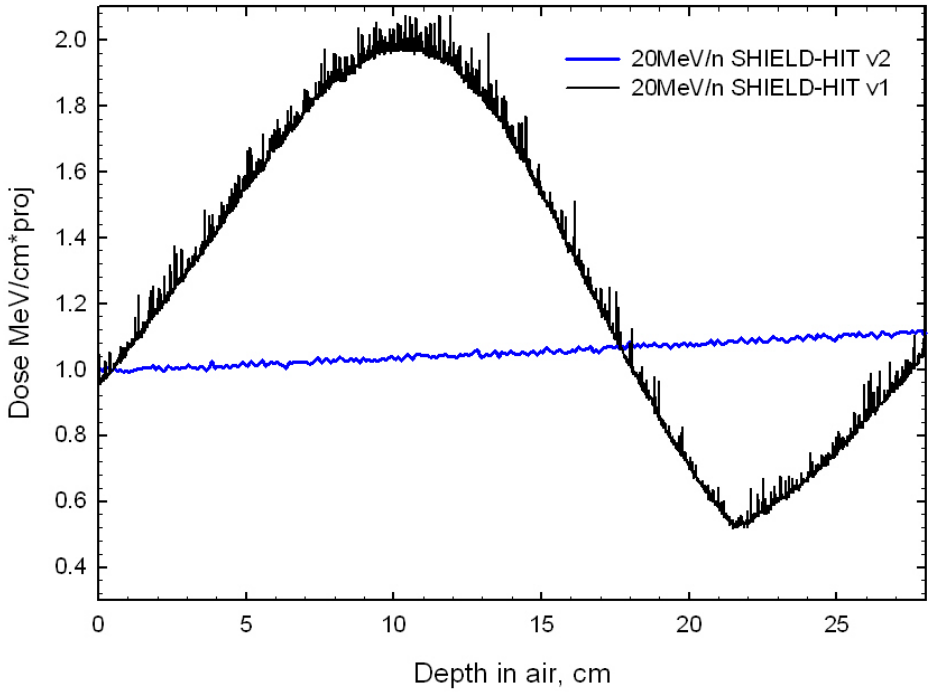

Figure 51 Comparison of the depth dose deposition in air of carbon ions with an energy of 20MeV/n calculated with different versions of the SHIELD-HIT code.

These calculations were performed to validate the code before the simulation of ionization chamber. The dose deposition of the carbon ions with energy of 20Mev/u in air is plotted in Fig.51. The calculations made with the single precision version of SHIELD-HIT (v1) are compared with those made with the modified double precision version SHIELD-HIT v2. From Fig.51 the precision effect is drastically evident. While the single precision version of SHIELD-HIT yields dramatic short and long-range fluctuations of the data, which obviously are not physical, the revised code shows behaviour that is more reasonable.

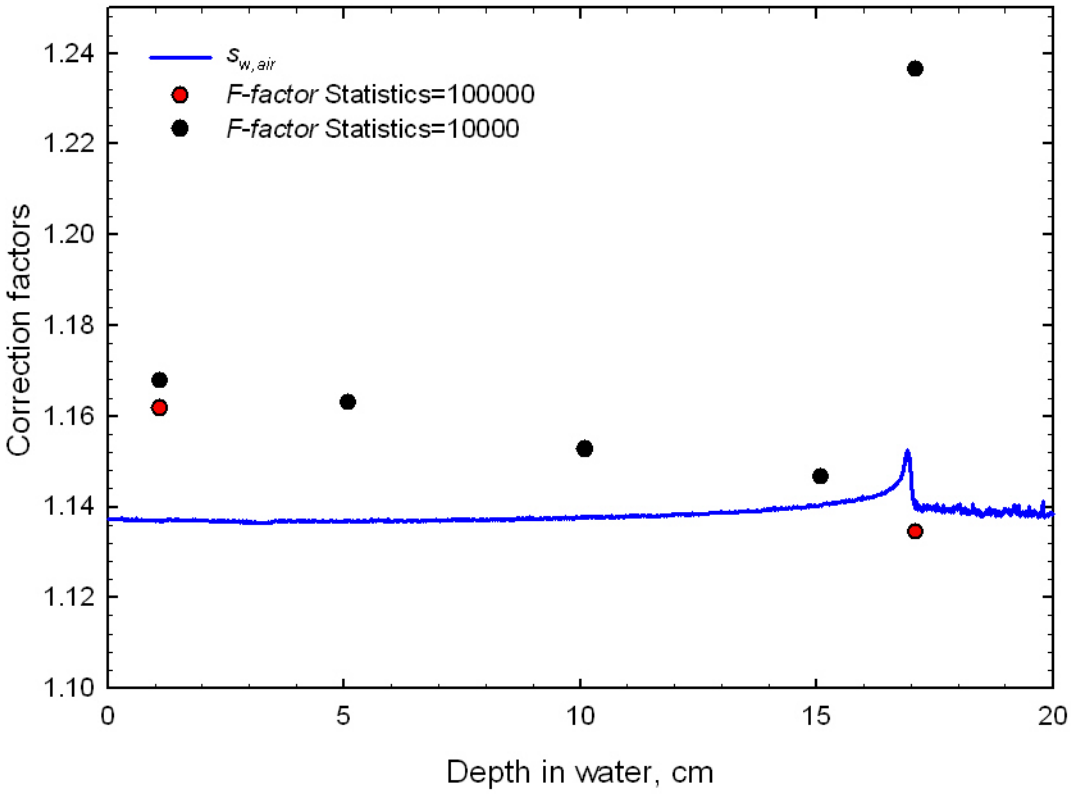

Figure 52 The stopping power ratio and *F-factor* calculated with SHIELD-HIT v2 for a Roos chamber irradiated with carbon beam of 300MeV/u with different calculation statistics.

The combined correction factor (F-factor), calculated for the Roos ionization chamber, is plotted in Fig.51. The simulations were done with a different statistics for a carbon beam with energy of 300MeV/u. The F-factor is compared with the stopping power ratio calculated for ^{12}C of the same energy. Both data show qualitatively the same behaviour: a plateau region and a peak at the depth of 17cm. The maximum deviation between the data shows up in the peak and amounts 3%.

4 Discussion

The following chapter is divided into three subsections. The first section discusses the results of the code validation, its comparison with experimental data and another Monte Carlo code. The second section reviews all calculations of stopping power ratios performed for carbon beams and other ions of interest for particle therapy. It analyzes the contribution of the secondary particles on the total stopping power ratio as well as the influence of other factors like geometry of the calculation, different beam parameters and *I-values* used to calculate the stopping power data. The third section presents the discussion of different other applications calculated with SHIELD-HIT v2.

4.1 The code validation

In the framework of the present thesis a series of code modifications were introduced to SHIELD-HIT. One of the main tasks among the series of improvements was to decrease the lower cut-off energy of the particle transport. The first version of the SHIELD-HIT was able to transport particles only down to 1MeV. For this purpose a modification of the Bethe-Bloch formula for stopping power calculations was introduced (see paragraph 2.5). One can see from the comparison of the results obtained with the different formulas used in SHIELD-HIT with ICRU reference data, that the unmodified Bethe-Bloch equation is able to reproduce reliable data for carbon ions in water (Fig.15) and in complex media like cortical bone (Fig.16) down to 3MeV/u. By taking into account the changes of an effective ion charge during the penetration and inclusion of the Lindhard-Scharff model, the calculations with the Bethe-Bloch formula improved considerably for the low energy region. This improvement allows decreasing the cut-off energy down to 10keV/u with a reasonable agreement with the ICRU data.

The comparison of the calculated depth dose profiles with experimental data plotted in Figures 17-22 shows very good agreement between the present SHIELD-HIT v2 simulations and measurements by different authors. The comparison of the Bragg curves obtained for different primary ions from different accelerators and experiments confirms the overall good performance of the code. The inclusion of the standard stopping power data from ICRU-73 and as additional choice MSTAR data in the code allows now to reproduce accurately the position of the peaks.

In Fig.17 one can see that the previously observed difference in the height and position of the Bragg peak [Gudow04] is eliminated. The differences in peak heights for the depth dose profiles with the energies of 195, 270 and 330MeV/u measured within the present work

(Fig.19) and by [Sihver98] (Fig.17, 18) can be explained by several differences in the experiments. First of all, a different step size of the depths of the measurements was used (0.1mm used by [Sihver98] and 1mm in this work). For the lowest initial energy (195MeV/u) the peak is very narrow and may reach its maximum in between two data points when using a 1mm step size. Consequently the maximum deviation (16%) appears in this case.

Another important difference is the size of the ionization chambers. Bragg curves plotted in Fig.19 were measured with chambers of a radius (R=2.4cm) five times smaller than used by Sihver (R=10cm). This difference may become more critical for higher energies and larger penetration depths, where the effects of multiple scattering are most important. In case of the small cavity chambers, there may be some scattered particles which were not measured. Therefore, two SHIELD-HIT v2 simulations of the curve for 330Mev/u were performed using the same step size of 1mm but a different radius of the scoring cylinder of 2.4cm and 10cm. The two calculations differ by 1.3% in the peak. The varying chamber sizes thus don't seem to introduce a significantly large effect.

Rather, it is concluded, that the difference between the measured and calculated peak heights shown in Fig.19 can be explained by the coarser grid of measurement depths (1mm) used in the experiment.

There are two more factors which may have an influence on the measured data in both experiments. The ionization chambers used in both experiments were operated with a different gas in the cavity. Measurements presented in Fig.19 were carried out with air filled ionization chamber while Shiver used chambers filled with a mixture of Ar and CO_2 (ratio 80:20). The different gases may exhibit a different behavior of the W-value and the stopping power as a function of energy, which would be included in the measured relative doses of both experiments. Due to a lack of data, the size of this effect, however, can currently not be evaluated.

Concerning the fragmentation model, SHIELD-HIT v1 overestimated the attenuation of the primary particles as can be seen in Fig.24. By adjusting the parameters of the Fermi break-up model, the attenuation of the projectile and the production of the light fragments were corrected and a better agreement with experimental data was obtained. Thus, the spectra of primary and secondary particles as a function of depth in water in Fig.23 show good agreement between the measurements made at HIMAC and SHIELD-HIT v2 calculations.

One of the main issues in ion transport is the production of fragments. The presence of secondary particles leads to an unwanted dose deposition behind the peak and hence to the irradiation of healthy tissue. This effect cannot be avoided, but precise knowledge of the type of secondary particles and their energetic distribution allows predicting the biological

effects and allows a theoretical calculation of dosimetrical parameters. The values given in Table 3 give an impression of how the primary particles and their fragments contribute to the whole dose deposition. As can be seen, only 63.02% of the whole energy is deposited in the large scoring volume, the remaining fraction is taken away mostly by neutrons and protons. The primary ^{12}C particles contribute only with 43.2% to the total dose in the phantom. The following fragments are of highest importance in the energy contribution: protons (7.79%), ^{11}C (4.18%), ^{4}He (2.68%) and ^{11}B (2.54%).

Light ions produced by a carbon beam undergo Coulomb scattering and cause spatial spreading of the primary beam. Hence, it is important to know the angular spectra of the secondary particles. Corresponding measurements were done at GSI by Gunzert-Marx [Gunzert04]. The comparison of the experimental data with calculations using SHIELD-HIT v1 and v2 (see Fig.29, 30) shows reasonably good agreement for all available data. The obvious increase of the influence of the scattering on the light fragments with decreasing fragments mass is demonstrated. For instance, the fluence of protons at 10^o degree compared to those at 0^o decreases only by 56% (at a corresponding energy of the primary beam of 100MeV/u) while the fluence of alpha particles for the same parameters decreases by 98%. This finding is of a special importance for the treatment of deep-seated tumours in the trunk of the body. Though carbon ions beams suffer less from scattering than proton beams, the light fragments produced at large depths can scatter significantly and thus cause an unwanted dose deposition to the surrounding healthy tissue lateral to the primary beam.

The comparison of the lateral profiles obtained from a scanned carbon beam in a water phantom shows a very good agreement between the experimental data and SHIELD-HIT v2 calculations (see Fig.31-33). SHIELD-HIT v2 reproduces the lateral profiles in plateau and peak regions correctly but underestimates the dose in the tail. This difference can be explained by the following: for the simulation of the scanning beam in Y direction only three beams were calculated, while in reality the beam was scanned over 12 positions. Although for the measurements the pin-point ionization chambers were positioned along the central beam, scattered light fragments from all positions contribute to the total dose deposition. This effect is mostly pronounced behind the Bragg peak, where no more primary ions are present. This finding is confirmed by the measurements and simulation of the spatial fragments distribution discussed in Figures 29 and 30).

The contribution of secondary particles to the total dose deposition in lateral beam profiles was analyzed in detail (see Fig.34-36). Though the contribution of different fragments was already investigated (see Table 3) to define the importance of every fragment type, the estimation was made for the integral dose in the whole water cylinder. The present

investigation made for lateral profiles allows analyzing the influence of the fragmentation on the scattering. One can see that the carbon ions are the main dose contributors in the plateau and peak regions. Boron ions form the main contribution to the dose in the central region in comparison to other fragments. It is interesting to notice (Figure 34), that already in the plateau the light fragments are scattered significantly. This may be not only due to the Coulomb scattering, but also due to the lateral momentum transfer that contributes to the deflection of the produced fragment during reaction [Matsuf05]. In the fragment tail, where no primary ^{12}C ions are left (only a minor fraction of carbon isotopes), boron and helium fragments play the dominant role at the central position of the lateral profile (0mm) (see Fig.36). Protons suffer most from scattering and hence are carrying a significant dose outside the irradiated field. Thus, in the tail region, protons contribute only with 9% to the total dose in the centre, but become the dominant particles at a lateral distance of 24mm and further away from the centre.

The calculation of a spread-out Bragg peak done with SHIELD-HIT v2 is in perfect agreement with experimental data (see Fig.37). TRiP BEAM strongly overestimates the deposited dose in plateau and in target region. As it is demonstrated in Fig.34 and Fig.35, carbon ions contribute the most to the total dose in these regions. One can see from the comparison of the attenuation of projectiles (Fig. 23) that TRiP BEAM overestimates the amount of primary particles with greater depth. This may explain the overestimation of the deposited dose by TRiP BEAM in the plateau and peak regions.

The difference in simulation data from SHIELD-HIT v2 in the fragment tail region between Fig.33 and Fig.37 could be caused by the different geometry and beam parameters for the simulations. Different geometries were used because of the restricted possibilities of the SHIELD-HIT code. Thus, in one case (Fig.33) the simulation was done for the cylinder slices of thickness 0.1mm and energy spread of 0.445% (to simulate the Ripple-filter). In the other case (Fig.37) the calculation was done for a cylinder with 0.01cm slices thickness and normalization function was applied to simulate the ripple filter. Moreover, for the lateral profiles the simulation of the beam scanning in X and Y direction was done (see paragraph 2.8.1) while for the depth dose profile only a single beam was transported. This does not influence the plateau and peak regions, but in the fragment tail, where scattered fragments play a major role, this difference in simulations can become an important issue.

The calculations done with SHIELD-HIT v2 were also compared with the hadron transport code GEANT4 (see Fig.25). One dominant feature of the data presented in Fig.35 is the difference in the peak positions. The explanation of the shift between the peaks position could be the use of different physical models in the codes and, even more important, differing stopping power data. For the present calculations, SHIELD-HIT v2 uses ICRU

stopping power data while GEANT4 calculates the stopping powers just for protons and then for the other ions uses scaling z^2. The contribution of the primary and secondary particles to the total dose deposition looks quite similar (see Fig.26). The attenuation of primary particles and the production of the secondaries as a function of the depth in water show relatively good agreement (see Fig.27, 28). The biggest difference between the fragment calculations appears in the production of protons and Li ions. As the numerical comparison of SHIELD-HIT v2 calculations with different experimental data yielded excellent agreement, it is concluded that GEANT4 does not reproduce the peak position correctly and underestimates the production of protons and Li fragments.

From the overall good agreement of the SHIELD-HIT v2 and experimental data for all available clinically relevant ions, it can be concluded, that the code is also applicable for the primary ions like He, Li, Be etc., which is of importance for the calculations of the dosimetrical parameters for these ions.

4.2 Stopping power ratios

4.2.1 Calculation with ICRU stopping power data

The value of the stopping power ratio is influenced according to the equation (2.3.2.1) by the particle spectra and stopping power data. As one can see from the comparison, SHIELD-HIT v2 reproduces data that are in perfect agreement with different measurements. Hence, one can trust the simulated particle spectra differential in energy at different depths. Concerning the stopping power data, the modified Bethe-Bloch formula produces now reasonable results at low energies in comparison with the old version. This was verified by calculating the ratio to the “reference” ICRU-73 data (see Fig.37). For the calculation of the stopping power ratio, the ion transport in water only was necessary. As the corresponding standard stopping power data from ICRU-49 and ICRU-73 are available for this case, these were used for all calculations presented in Fig.38-44.

The Monte Carlo calculated water/air stopping power ratios shown in Figure 38 exceed the recommended constant value (1.130) over the whole particle range. This fact can be explained by Fig.42. In Figure 42, ratios of stopping powers water-to-air for carbon ions, where the data are taken directly from ICRU-49 and ICRU-73 tables (i.e. no Monte Carlo calculation involved), are plotted as a function of energy. As it can be seen, the values from ICRU-73 (from Li up to O) are systematically larger than the TRS-398 recommended value of 1.13 over the whole energy range. Thus, parts of the differences discussed in relation with Fig 38 for the plateau region are exclusively due to the new set of ICRU-73 stopping-powers. The low energy part in Fig. 42 corresponds to the low energies found in the vicinity

of the Bragg peak at therapeutic energies. There is an interesting point to be noticed: TRS-398 does not recommend using the constant value at such low energies; this is confirmed by the figure, which indicates a large uncertainty if the value 1.13 is applied in conditions, which are not uncommon in certain radiobiological experiments performed at low energies.

The calculations for the present work were done for cylindrical slices of 1 mm thickness. As the height of the Bragg peak depends on the geometrical resolution (especially for low initial energies), the stopping power ratio maximum does too. For finer slices (0.1 mm) the difference in $s_{w,air}$ for 50MeV/u to the constant value of 1.130 reaches up to 4%; when the resolution is changed to 2 mm it is 2%. This behaviour of $s_{w,air}$ points at the necessity of performing individual calculations for every type of ionization chamber with different air cavity sizes, especially at low energies. Depending on the chamber geometry, the height of the stopping power ratio peak will be different. Thus, for a well-defined geometry (plane-parallel ionization chambers) the dose measurement corresponds to a very thins “slice” in water while cylindrical chambers integrate the deposited dose over the cavity in different depths (thicker “slice”), which decreases the peak height.

For the present work the calculation of stopping power ratios was done with a cut-off energy of 25keV/u, which is the lowest value in ICRU-73 stopping power data. However, the corresponding range of carbon ions in air for this energy is 2.7 mm. In order to investigate the influence of the cut-off energy value, several calculations using different Δ (from 10keV/u up to 1MeV/u) were done. The difference in the results was not larger than 0.1%.

The contribution of “track-ends” to the total dose deposition and to the corresponding stopping power ratio is very low (0.4% and 0.1% respectively). As it seems, they don’t play a big role for light ion dosimetry as they do for electrons, where the contribution to the total deposited dose can be between 6% and 8% [ICRU84]. For the case of electrons, the secondary particles are also electrons and the number of secondaries per primary particle is huge, while their range is relatively small. This explains the relative big contribution of the track ends to the total deposited dose. For the case of heavy ions, the secondaries are few ions with relative high energy that are able to penetrate further without direct absorption. Hence, there are very few track-ends in the track of primary ions.

The influence of the produced fragments on the stopping power ratio from the primary ions was investigated. In the case for the highest clinically relevant beam energy (450MeV/u), ^{4}He and ^{3}He fragments decrease the stopping power ratio.

The stopping power ratio for ^{12}C alone is decreased by inclusion of all fragments by 0.5% in the plateau and 0.9% in the peak region (Fig.40).

The calculation of the stopping power ratios with SHIELD-HIT v2 for all clinically relevant ions was carried out (see Fig.43). As for the simulations ICRU stopping power tables were used, all obtained data are higher then the recommended by TRS-398 constant over the whole depth of penetration. The maximum deviation from 1.13 makes up 4.6% for the initial energy of 50MeV/u. It is interesting to notice the influence of the fragments: at the same depth of approximately 25cm in water, heavier ions like ^{14}N or ^{16}O produce more secondary particles than ^{7}Li or ^{9}Be and the increase of $s_{w,air}$ at the distal fall-off is lower due to the influence of fragments.

Nowadays, the suitability of ^{3}He and ^{4}He ions for radiotherapy is discussed. Advantages or disadvantages of both isotopes for the clinical application are still not clear. The calculation of the stopping power ratios at 15 and 25cm water depth showed a negligible difference of 0.2% at the peak. The investigation of the dose deposition from ^{3}He and ^{4}He with 15cm range showed that ^{3}He contributes 84.79% and the main fragment proton contributes 13.74% to the total dose deposition. The projectile ^{4}He contributes 83.24% to the total dose and has three important fragments: protons (12.5%), ^{3}He (2.53%) and tritium (1.14%). From this comparison the difference between ^{3}He and ^{4}He seems to be negligible. One interesting fact was revealed by the analysis of neutron production from the He isotopes: every primary ^{4}He ion produces one neutron while every three primary ^{3}He ions produce only two neutrons. Hence, the use of ^{3}He could be more reasonable from radiation protection considerations. The spatial distribution of the particles spectrum form ^{3}He and ^{4}He was not investigated. But as ^{4}He ions are heavier then ^{3}He ions, they will be scattered less than ^{3}He, thus leading to a larger lateral dose gradient in the treatment field.

4.2.2 Calculation with BEST data using different I-values

For the present work all calculations of stopping power ratios for different ions (see Fig.39-45) were performed using ICRU-49 and ICRU-73 stopping power data. The ICRU data are considered as a “gold standard”. A more detailed investigation has raised some doubts. As one can see from the Table 4, I-values for water or air medium for protons, alpha particles (ICRU-49) and for heavier ions (ICRU-73) are not consistent, which is not obvious from the ICRU data. The topic is discussed in detail in [Paul06B]. As it was already shown above in equation (2.3.4.3) [Paul06A], the ratio of stopping powers is directly dependent on the I-values. Fig.46 confirms this statement presenting the ratio of stopping powers water/air for carbon ions obtained from different sources of data. Though the I-values in MSTAR and SRIM stopping power data are not well known, it is obvious from the ICRU-73 or BEST data, that a higher ionization potential yields a lower ratio of stopping powers.

The ionization potential is depending on the material, but not on the projectile. Hence, the calculation of stopping power ratios for heavy ions like carbon or oxygen, where a whole spectrum of fragments is present, implies a set of stopping power data with consistent I-values. As this was not the case for the ICRU data, this fact could also explain the influence of He ions on the stopping power ratio for carbon ions. As helium in ICRU-49 has a higher ionization potential for water (75eV) than the heavier ions in ICRU-73 (67.2eV), it has lower ratio of stopping powers, which reduces the total stopping power ratio.

In the mentioned paper [Paul06B], the choice of a new set of consistent values for the ionization potential for water and air is justified by experimental data. The calculation of stopping power ratios (see Fig.47) using different sets of I-values deviates slightly from the previous results as shown in Fig.39. First of all the new stopping power ratio is slightly lower over the whole particle range (due to the higher I-values as nothing else in code was changed). Even more important is the near equivalence of the stopping power ratio and the ratio of stopping powers, except for the peak region. Figure 48 confirms this statement. The influence of the fragments on the total stopping power ratio (see Fig.47) is negligible over the large range of energies if the stopping power data used for the calculations have a consistent ionization potential for water and air for all ions.

The peak height for 400MeV/u stopping power ratios for different I-values does not exceed a deviation of $s_{w,air}$ of 2% from the adopted constant predicted by TRS-398. For the lowest clinical energy (50MeV/u) the deviation becomes more critical (using also the calculations with ICRU) and increases up to 3% in the stopping region. There is one more important issue to be noticed: changes of the ionization potential for water shift the position of Bragg peak and so the peak of stopping power ratio. Thus, for the 400MeV/u curve the change of I-value by 5eV (from 75eV to 80.88eV) shifts the peak on 2mm. This does not happen for low energy, which allows to consider this effect as a function of initial energy. This fact was already noticed earlier by [Krämer00], who increased the I_{water} from 75eV up to 77eV in the stopping power data in order to better reproduce the position of Bragg peak.

4.3 Other applications of the SHIELD-HIT v2

In the present thesis two additional applications of the SHIELD-HIT v2 were presented, besides the comparison with experimental data or calculation of the stopping power ratios.

The new version with double precision variables and extended energy grid allows transporting particles in low-density materials (see Fig.51). Though the simulations in air show reasonable output now, the calculations of the *F*-factor (see Fig.52) did not yield reliable results. The deviation of the f-factor from the data for the stopping power ratio in the

plateau region does not seem to be relevant. The reason may be in the small statistical fluctuations of the deposited dose to air (see Fig.51). These are not relevant for the dose profile over the whole depth, but for the simulation of the tiny cavity (2mm thick) this deviation becomes important. The increase of the simulation statistics by a factor of ten decreases the deviation. Hence, the resulting value in the peak region can not be trusted, even with the large statistics. Further investigations with higher Monte Carlo statistics are necessary in this type of calculations.

To simulate the response of the TLD and Alanine detectors on irradiation with antiprotons calculations with SHIELD-HIT v2 were performed. The calculated mixed-particle spectra from the antiprotons annihilation was used as an input parameter for the model calculations. The results of comparisons between the measurements and calculations presented in Figures 49-50 are contradictory. On the one hand the fact of nonlinear response of this type of dosimeters in high LET[22] regions (Bragg peak) is well known. There may still be a problem with the experimental data in the peak region. On the other hand SHIELD-HIT v2 has never been validated with experimental data for antiprotons and it cannot be assumed that the predicted values are of similarly good quality as for ions. Finally, the calculation of the dosimeter response could be inaccurate due to the uncertainty of the underlying models.

[22] Linear Energy Transfer (LET) is the energy lost dE by a charged particle traversing a distance dl.

5 Conclusions and Outlook

For the present work substantial modifications to the Monte Carlo code SHIELD-HIT v1 [Gudowska04] were introduced and a new version SHIELD-HIT v2 was developed. All variables within the code were converted to double precision. The lowest particle transport energy was decreased from 1MeV/u down to 10keV/u by modifying the implementation of the Bethe-Bloch stopping-power formula and extending the energy grids. Additionally, optional MSTAR and ICRU-73 stopping power data were included, and the fragmentation model was modified. The new code is able to reproduce practically all available data, which are relevant for ion therapy, with reasonable accuracy and with considerable improvements as compared to the older version.

The simulations for the lateral profile of the scanned beam confirmed, that carbon ions suffer very little from lateral scattering. It was also shown, however, that the light fragments like protons and helium ions do suffer significantly from lateral scattering and thus generate a halo of light ions around the central carbon beam. Thus, a substantial lateral penumbra in the dose distribution appears already in the plateau region.

The accurate calculation of stopping power ratios for ionization chamber dosimetry with SHIELD-HIT v2 and ICRU-73 data for carbon ions, including the production of all possible fragments, shows a dependence of $s_{w,air}$ on the initial particle energy, depth in water and geometry which has not been available before. The use of state-of-the-art stopping power data ICRU-73 results in values that on the average differ between 0.5-1% from the IAEA TRS-398 recommended constant value of 1.130 over a large range of depths with the exception of the region close to the Bragg peak. It has been found that the newly calculated $s_{w,air}$ deviates as much as 2.3% at the Bragg peak from the recommended constant value for an energy of 50MeV/u (using slices of 1mm thickness). The fragments decrease the stopping power ratio for primary particles by 0.5% in the plateau and 0.9% in the peak region. The deviations found in the Bragg peak region may be included in future, more detailed recommendations for plane-parallel ionization chambers. In general, the uncertainty of the stopping power ratio for ions and thus for the absorbed dose can be reduced significantly, at least by a factor of 2.

The investigation of the influence of I-values on the stopping power ratio showed the importance of this parameter. The revealed inconsistency of the ionization potential values in ICRU-49 and ICRU-73 shows the need for better data for the I-values. The stopping power ratios for carbon ions calculated with stopping power data from BEST showed again

a maximum deviation from the adopted constant (up to 3%) and the influence of the fragments in the peak region. In the plateau region a near identity of the total stopping power ratio and the ratio of stopping powers was found (i.e. secondaries do not influence this region). Thus, the use of consistent stopping power data for the whole particle spectra simplifies the calculations. Now the calculation of stopping power ratios can be replaced by a simple ratio of stopping powers in the plateau region as a good approximation. In the Bragg peak region, however, the detailed knowledge on the fragment spectra should be taken into account. Furthermore, at low initial energies (50-150MeV/u) the deviation from the recommended adopted constant (1.130) becomes critical. The choice of the ionization potential value for water and air still has to be discussed, as it influences not only the values of stopping power, but also the position of the Bragg peak, which is of highest priority for the particle therapy.

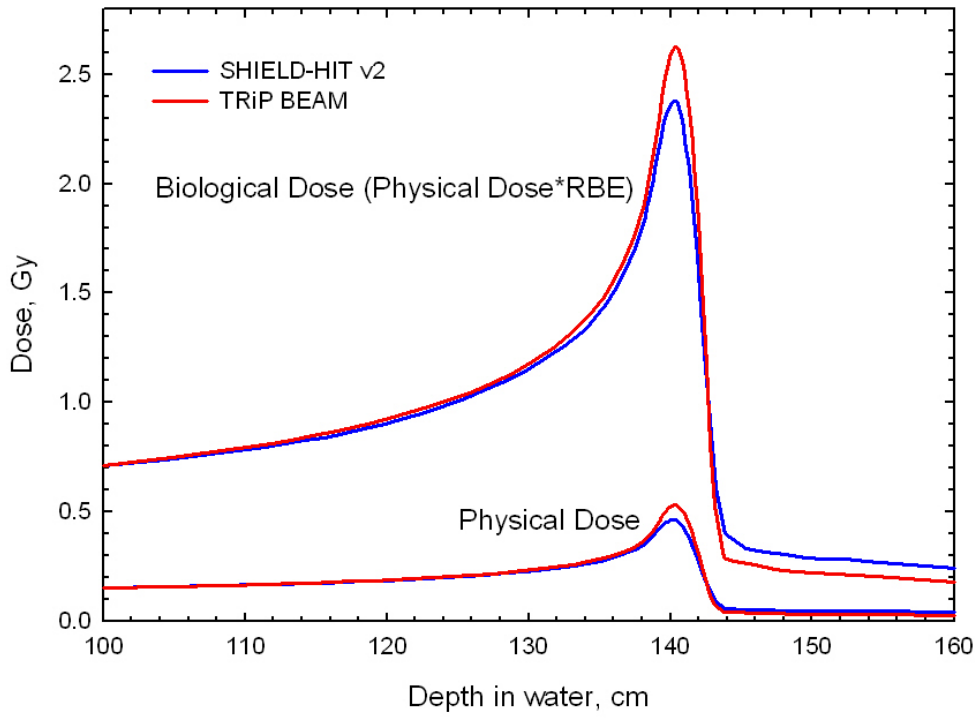

Figure 53 Comparison of the physical and biological doses of carbon beam with energy of 270MeV/u calculated with SHIELD-HIT v2 and TRiP BEAM.

The field of the further application of the SHIELD-HIT v2 in medical physics is very broad. The calculated particle spectrum can be used as an input data base for the calculations of biological effects, like in the LEM model [Scholz97], which is used to calculate the Relative Biological Effectiveness (RBE) of a mixed particle beam. Such calculations are used routinely in the treatment planning procedure for the evaluation of the biological dose. As an

example, some first results are presented in Fig.53, where the calculations of physical dose and RBE were performed using with the particle spectra obtained from the SHIELD-HIT v2 and TRiP BEAM, respectively. The physical and biological doses deviate in the peak region by 14% and 10.3% correspondingly. The fragment production and dose profiles were already compared within the present thesis, and TRiP BEAM showed an overestimation of the physical dose. This relatively small deviation for the biological effective dose might indicate a rather weak dependence of the biological effectiveness from the detailed underlying particle spectrum (which was considerably different in this case). Further comparison for the spread-out Bragg peaks and deeper investigation of the importance of different fragments for the biological dose are necessary, however, to come to a final conclusion.

A further application of SHIELD-HIT v2 may be the calculation of ion ranges in different biological tissues for the treatment planning with heavy ions. The information on the composition and spatial distribution of produced secondary particles can also be applied in the in-beam Positron Emission Tomography (PET) research. For the purpose of radiation protection the simulation of neutron production can be used to optimize the shielding.

Appendix A

An overview of Monte Carlo hadron codes existing today

NMTC

The original code NMTC gave the base for many different hadron transport codes which are well established today. Figure 10 shows the main stages of development and the publication years of the new version.

This overview is not complete. There are many more successors to the original version, only the most important versions are mentioned. A short description of every version will be presented in the following passage.

The code **LAHET** (Los Alamos High Energy Transport) was developed in 1989 in the Los Alamos National Laboratory [Prael89]. It was based on the Los Alamos version of HETC. The generator of inelastic interactions includes several nuclear models [Prael94]. Besides the intranuclear cascade model of Bertini [Bertin69], the additional program ISABEL INC [Yariv79] was included. The pre-equilibrium de-excitation of the nucleon is simulated with the MPM (Multistep Pre-equilibrium Exciton Model) model [Prael88]. At the stage of equilibrium de-excitation two competing processes are taken into account: evaporation and fission; for fission, two alternative models were included: ORNL [Barish81] and RAL [Atchis80]. The de-excitation of light ions ($A \leq 17$) is calculated with the Fermi break-up model [Bren81]. The program PHT [Prael89] was included for the modeling of the cascade of γ-transitions for the nuclear de-excitation. The main application field of LAHET is the nucleon-pion cascade in a target with complex geometry for energies up to 10 GeV. Included is the optional program ISABEI INC allows modeling nuclear-nuclear interactions and transporting only lightest ions with $A \leq 4$ with energies up to 1 GeV [Preal94].

A relatively new code **MCNPX** has been developed as well in the Los Alamos NL [Hughes97]. MCNPX includes the same physical models like LAHET and the generator of hadron-nucleus (hA) interactions from FLUKA87 (see below). But in comparison to LAHET, the list of transported particles is extended: besides nuclei, pions, electrons, γ-quanta, anti-nuclei and kaons are included. The applicability of MCNPX for light ion transport in radiation therapy is still limited and enhancements for this purpose are in the development phase. At present MCNPX does not include the transport of ions with A>4. MCNPX as well as MCNP is not freely available but is distributed only with permission of the American Department of Energy (DOE).

HERMES (High Energy Radiation Monte Carlo Elaborate System) includes a complex of several programs that work independently and exchange data via external files [Cloth88]. Besides the code HETC, this program complex includes:

- Multigroup neutron code MORSE-CG [Emmet75] that allows to transport neutrons and γ-quanta below 20MeV
- Program EGS4 [Nelson85], that models electromagnetic showers
- Program PHT [Prael89] that uses a database for nuclear levels to simulate the cascades of γ-transitions during de-excitation of residual nuclei

All transport codes in the HERMES complex support geometrical module CG [Emmet75]. Also as LAHET, HERMES allows modeling nucleon-pion cascades up to 15-20 GeV. The main fields of application of this code are spallation processes.

NMTC/JAERI simulates high energy nuclear reactions and nucleon-meson transport processes. NMTC/JAERI97 is an upgraded version of the code system NMTC/JAERI. It implements an intra-nuclear cascade model [Bertin69] taking into account the in-medium nuclear effects. For dealing with the nucleon transport process, the nucleon-nucleus cross sections are revised to those derived by the systematic of Pearlstein. Moreover, the level density parameter derived by Ignatyuk is included as a new option for particle evaporation calculations. The geometry package CG [Emmet75] with a multi-array system and the importance sampling technique is implemented in the code. The Tally function is also employed for obtaining physical quantities like neutron energy spectra, heat deposition and nuclide yield. The code can simulate two processes: the primary spallation reaction and the secondary particle transport in the intermediate energy region from 20 MeV to 3.5 GeV. The code has been employed in combination with the neutron-photon transport codes available to the energy region below 20 MeV for the calculation of neutrons behavior in accelerator-based sub-critical reactors, analyses of thick spallation targets in experiments and so on.

PHITS (Particle and Heavy Ion Transport code System) code [Iwase02] is based on the NMTC/JAM [Niita01]. It enables the user to simulate hadron-nucleus reactions with energies up to 200 GeV, nucleus-nucleus collisions up to several GeV/n and the transport of heavy ions, all hadrons including low energy neutrons and leptons.

In the PHITS calculation, the cross sections of high energy hadron-nucleus reaction products are calculated by the hadronic cascade model JAM (Jet AA Microscopic Transport Model) [Nara01], which explicitly treats all known hadronic states and resonances. Each hadron-hadron cross section used in JAM was parameterized to reproduce available experimental data. The JQMD (JAERI Quantum Molecular Dynamics) model [Niita95] was

integrated in the code to simulate nuclear-nuclear collisions. In the particle transport simulation, the SPAR code [Armstr73] is adopted for calculating the stopping powers of charged particles. PHITS transports also low energy neutrons, photons and electrons using evaluated nuclear data libraries.

As mentioned before, the Monte Carlo codes based on original codes NMTC and SHIELD use an exclusive approach for simulating the nuclear reactions. There is one more group of codes based on the program FLUKA which was developed at the European particle laboratory CERN. FLUKA calculates the individual (exclusive) characteristics for all nuclear reactions occurred.

FLUKA

The first version of FLUKA was released in 1964 [Ranft74]. This version was used for simulating in an inclusive approach the radiation shielding for accelerators for high energies. The low energetic component of cascade was ignored.

Later the code was improved and reoriented on exclusive simulations via the program DPMJET [Ranft97]. Until the beginning of 1990 code FLUKA was used rather for high energy projects (FLUKA82, FLUKA87). The range of applicable energies reached from several GeV up to 20 TeV. The low energy part of the hadron cascade still was ignored, because the model DPM used in FLUKA is not valid for low energies.

Fasso and Ferrari [Fasso93] extended the applicable range of FLUKA to lower energies [Fasso93]. For that purpose the generator of hA interactions was supplemented by corresponding physical models [Fasso94], including the intra-nuclear cascade model PEANUT, a pre-equilibrium emission model [Blann83] and an evaporation model EVAP-5, which is used in HERMES. Fission competes with evaporation according to the RAL model [Atchis80, Atchis94]. Multifragmentation of highly excited residual nuclei is not taken into account.

The modern version of FLUKA transports nucleons, pions, kaons, antinucleons and muons in complex targets with energies up to 20 TeV and also $\gamma\, e^{-}$ showers. At present, the work on including a QMD (Quantum Dynamic Model) model is in progress [Andrers02]. The inclusion of this model will allow simulating the interaction of heavy ions with range energies lower than several GeV.

For the transport of low energy neutrons the user needs external neutron transport code. For instance, in the TRAC project [TRAC99] FLUKA is used together with the neutron transport code EET. Using this set of codes, authors simulated long term proton irradiation

of complex targets in order to investigate the possibilities of transmuting nuclear waste stemming from nuclear power plants.

Today at least four modern versions of FLUKA exist with different sets of physics models.

The different versions of the original codes SHIELD, HETC and FLUKA discussed in the previous paragraphs represent almost all independent stages of development of the exclusive transport codes for accelerator energies. As was already mentioned, the simulation using the exclusive approach has certain advantages. The exclusive generator yields all reaction products with their individual parameters, including the residual nucleus. The conservation laws of energy-impulse, baryon number, charge, etc are preserved in every event. This type of simulation considers cascade fluctuation and any correlation between cascades. One of the main conveniences of this method is the possibility of direct calculation of the residual nucleus which was created in the hadron showers, i.e. target activation is calculated automatically.

On the other hand, the inclusive approach has its own advantages. Although the conservation laws are averaged over the whole event and the fluctuation parameters of the hadron cascade are set aside the calculation time in comparison to the exclusive generator is considerably lower. Moreover, it is technically easier to modify the parametrization of differential cross-sections to extend the energy range.

MARS is the code known best amongst inclusive transport codes.

MARS

Mohov released the primary version of the MARS code in 1974 [Mohov74]. Inclusive differential cross-sections are introduced in MARS by approximations elaborated in works of Kalinovksiy [Kalin85] and Sychov [Sych79, Sych86]. In the version MARS13 [Mohov98] a cascade-exciton model was included, which extended the energy range down to 3-5GeV. The inclusion of the exclusive model DPMJET [Ranft97] made MARS partly exclusive. The version MARS14 could already transport nucleons, pions, kaons, antinucleons , muons, electrons, photons, neutrino and atomic nuclei with $A \leq 4$. Further developments of the code concentrated on transport and interaction of heavy ions. Hence, in the latest version MARS15 several important upgrades were introduced, namely LAQGSM (Los Alamos Quark-Gluon String Model), and JINR model for elastic cross-sections. Further upgrades of this package are underway.

GEANT

The program package Geant was released in 1976-78 at CERN for modeling high energy experiments [Brun78]. The first version was purely electro-magnetic, i.e. without nuclear

interactions. In its next generation, GEANT3, straggling, multiple scattering and other electromagnetic processes were included. One special feature of the code is that the user can include any hA-generator for simulations. The generators FLUKA and GHEISHA are most commonly used for this purpose. GHEISHA [Fesef85] was developed especially for the use together with GEANT and allows simulating hA-interactions with energies up to 0.5TeV in a quasi-exclusive approach. The code uses an empirical approximation to determine cross-sections. GEANT4 was completely redesigned and rewritten based on the Geant3 simulation package using C++ and the object oriented paradigm. The project (RD44) was initiated in 1994 by the Simulation team at CERN led by Simone Giani and has been realized by an international collaboration of over 100 physicists representing the majority of major current and upcoming HEP experiments [SOURCE]. The idea was to collect all existing physical models for corresponding simulations and to include them into the code. The user decides which processes are relevant for his problem and which models to be applied. GEANT4's application areas include high energy physics and nuclear experiments, medical, accelerator and space physics studies.

Appendix B

A detailed scheme of Roos ionization chamber, simulated to derive *F-factor*

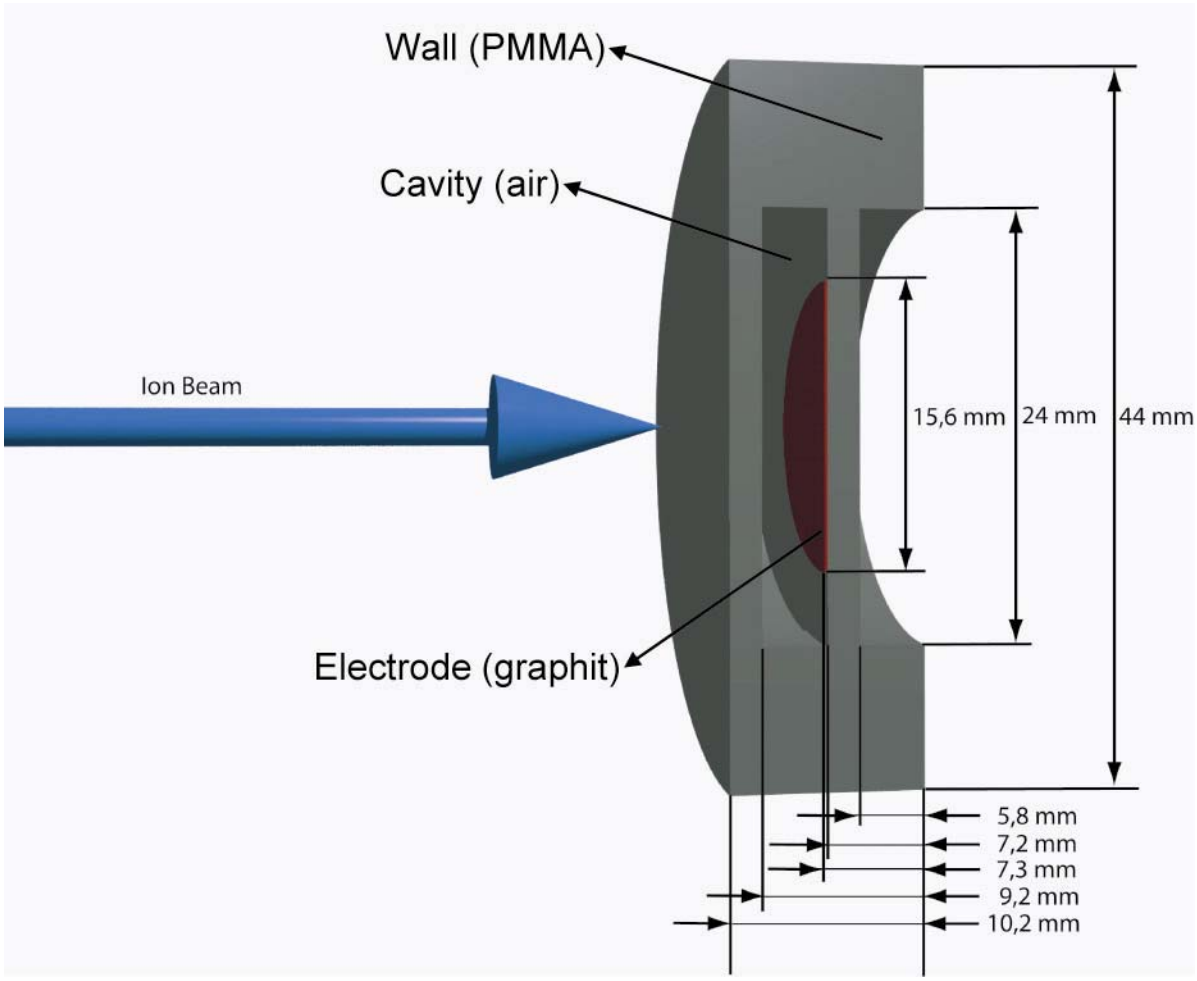

Figure 54

Appendix C

The influence of the PARLEV(39) parameter on the depth dose profile calculated for the carbon ion beam of 270MeV/u in water.

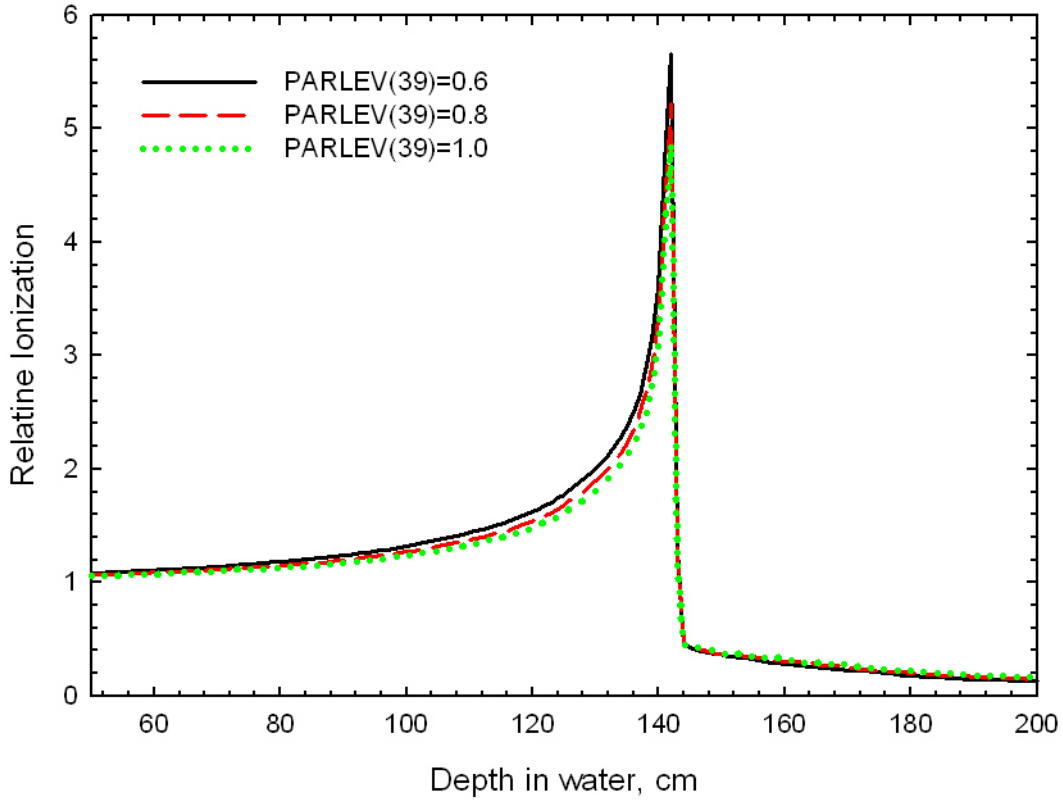

Figure 55

An empirical parameter ILEVRA determines the fragment production either in the exited (ILEVRA=0.2) or in main state (ILEVRA=1) of a nucleus. The parameter FKAP affects the number and composition of fragments. Default option is FKAP=1. FKAP was divided on two parameters: FKAP1 and FKAP2 (default: FKAP1=FKAP2=1). By decreasing FKAP1 to 0 and varying FKAP2 one influences the number and composition of produced fragments. Parameter PARLEV(39) renormalizes the cross-section of inelastic interaction of ions, thus influencing the attenuation of projectile and the number of produced fragments. Default option PARLEV(39)=1 can be decreased down to PARLEV(39)=0.5. The influence of this parameter on the depth dose profile is shown in Fig.55. All other parameters were not varied in the framework of this thesis, but might be of interest for future work.

List of Publications and Conference Contributions

C.1 Publications

- Jäkel O and Geithner O 2006 The lateral penumbra of carbon ion beams in large depths in water *In progress*
- Paul H, Geithner O and Jäkel O 2006 The influence of Stopping Powers upon Dosimetry for Radiation Therapy with energetic Ions *In progress*
- Geithner O, Andreo P, Sobolevsky N, Hartmann G and Jäkel O 2006 Calculation of stopping power ratios for carbon ion dosimetry *Phys Med Biol* **51** 2279-2292
- Filipenko (Geithner) O., Jäkel O., Andreo P., Sobolevsky N., Hartmann G.H.: Monte Carlo simulations for heavy ion dosimetry. In: E-Verhandlungen 2004. Abstracts der Frühjahrstagung in München. München: Deutsche Physikalische Gesellschaft (DPG) (2004) ST 6.2.
- Filipenko (Geithner), O., Jäkel, O., Andreo, P., Sobolevsky, N, Hartmann, G.: Monte Carlo simulations for heavy ion dosimetry. In: Programme and Abstracts of the 40th PTCOG Meeting, Paris, CPO and Institut Curie (16-18 June) (2004) 104.
- Filipenko (Geithner) O., Jäkel O., Andreo P., Sobolevsky N, Hartmann G.: Monte Carlo simulations for heavy ion dosimetry. In: Programme and Abstracts of the 23th ESTRO Meeting, Amsterdam, (25-28 October) (2004)
- Filipenko (Geithner) O; Jäkel O; Hartmann G; Andreo P; Sobolevsky N: Monte Carlo Simulations for Heavy Ion Dosimetry. In: Biomedizinische Technik, 50 (Suppl.1, Part 1). Hrsg.: U. Boenick u.a.. Berlin: Fachverlag Schiele & Schön GmbH, (2005) 348-349.
- Geithner O., Jäkel O., Andreo P., Sobolevsky N., Hartmann G.H.: Monte Carlo simulations for heavy ion dosimetry. In: Abstracts of the 43rd PTCOG Meeting, Munich 10-14 December (2005).
- Geithner O., Jäkel O., Andreo P., Sobolevsky N., Hartmann G.H.: Monte Carlo simulations for heavy ion dosimetry. In:. Abstracts der Frühjahrstagung in Heidelberg: Deutsche Physikalische Gesellschaft (DPG) (2006)

- Geithner O., Jäkel O., Andreo P., Sobolevsky N., Hartmann G.H.: Monte Carlo simulations for heavy ion dosimetry. In:. Abstracts In: Abstracts of the 44rd PTCOG Meeting, Zurich 14-16 June (2006)

C.2 Conference Contributions

Talk: Filipenko (Geithner) O., Jäkel O., Andreo P., Sobolevsky N., Hartmann G.H.: Monte Carlo simulations for heavy ion dosimetry. In: E-Verhandlungen 2004. Abstracts der Frühjahrstagung in München. München: Deutsche Physikalische Gesellschaft (DPG) (2004) ST 6.2.

Talk: Filipenko (Geithner), O., Jäkel, O., Andreo, P., Sobolevsky, N, Hartmann, G.: Monte Carlo simulations for heavy ion dosimetry. In: Programme and Abstracts of the 40th PTCOG Meeting, Paris, CPO and Institut Curie (16-18 June) (2004) 104.

Talk: Filipenko (Geithner) O., Jäkel O., Andreo P., Sobolevsky N, Hartmann G.: Monte Carlo simulations for heavy ion dosimetry. In: Programme and Abstracts of the 23th ESTRO Meeting, Amsterdam, (25-28 October) (2004)

Talk: Filipenko (Geithner) O; Jäkel O; Hartmann G; Andreo P; Sobolevsky N: Monte Carlo Simulations for Heavy Ion Dosimetry. In: Biomedizinische Technik, 50 (Suppl.1, Part 1). Hrsg.: U. Boenick u.a.. Berlin: Fachverlag Schiele & Schön GmbH, (2005) 348-349.

Poster: Geithner O., Jäkel O., Andreo P., Sobolevsky N., Hartmann G.H.: Monte Carlo simulations for heavy ion dosimetry. In: Abstracts of the 43rd PTCOG Meeting, Munich 10-14 December (2005).

Talk: Geithner O., Jäkel O., Andreo P., Sobolevsky N., Hartmann G.H.: Monte Carlo simulations for heavy ion dosimetry. In:. Abstracts der Frühjahrstagung in Heidelberg: Deutsche Physikalische Gesellschaft (DPG) (2006)

Talk: Geithner O., Jäkel O., Andreo P., Sobolevsky N., Hartmann G.H.: Monte Carlo simulations for heavy ion dosimetry. In:. Abstracts In: Abstracts of the 44rd PTCOG Meeting, Zurich 14-16 June (2006)

Bibliography

[AAPM86] AAPM 1986 Task Group 20: protocol for heavy charged particle therapy beam dosimetry *AAPM Report* 16 (New York: AAPM)

[Abag64] Abagyan L R et al 1964 Group constants for nuclear reactor calculations *Атомиздат (Atomedit), Moscow* (In Russian)

[Anders02] Anderson V, Ballarini F, Battistoni G et al 2002 The FLUKA Code for Space Applications: Recent Developments *COSAR,* f2.1-0007-02

[Andreo92] Andreo P 1992 Absorbed dose beam quality factors for the dosimetry of high-energy photon beams *Phys. Med. Biol.* **37** 2189-2211

[Andreo90] Andreo P 1990 Depth-dose and stopping-power data for monoenergetic electron beams *Nucl. Instr. Meth.* **B51** 107-121

[Andreo86] Andreo P and Brahme A 1986 Stopping-power data for high-energy photon beams *Phys. Med. Biol.* **31** 839-858

[Armstr72] Armstrong T W and Chandler K G 1972 HETC – A High Energy Transport Code *Nucl. Sci. Eng.* **49** 110

[Armstr73] Armstrong T W and Chandler K G 1973 *Nucl.Instr Meth.* **113** 313

[Atchis80] Atchison F 1980 Spallation and Fission in Heavy Metal Nuclei under Medium Energy Proton Bombardment, in “Targets For Neutron Beam Spallation Sources”, KFA Julich, Report Jul-Conf-34 17

[Atchis94] Atchison F 1994 A Treatment of Fission for HETC *Proc of a Specialists’ Meeting: Intermediate Energy Nuclear Data: Models and Codes, Paris*

[Attix85] Attix F H, 1986, Introduction to Radiological Physics and Radiation Dosimetry, Wiley, New York

[Barash72] Barashenkov V S and Toneev V D 1972 Interaction of high energetic particles and atomic nuclei with nucleons *Атомиздат (Atomedit), Moscow* (in Russian)

[Barash73A] Barashenkov V S et al 1973 Interaction of particles and atomic nuclei with nucleons *УФН* **109** 91 (in Russian)

[Barash73B] Barashenkov V S and Toneev V D 1973 Neutron fluxes, generated by high energetic protons in the thick Uranium blocks *Atomic Energy* **35** 163 (in Russian)

[Barish81] Barish J et al. HETFIS High-Energy Nucleon-Meson Transport Code with Fission. ORNL/TM-7882, Oak Ridge National Laboratory (1981).

[Bassler06] Bassler N, 2006, Experimental Studies Relevant for Antiprotons Cancer Therapy, Aarhus, Denmark, Dissertation

[Bath00] Batheld B 2000 Filmdosimetry in der Schwerionen-Tumortherapie: 3-dimensionale Dosisverifikation in gemischten Teilchenstrahlenfeldern, Darmstadt, Germany, Dissertation

[Benitsch05] Benitsch T 2005 Monte-Carlo-Simulationen der Dosisverteilungen eines therapeutischen Kohlenstoff-Ionenstrahls mithilfe von GEANT4, Heidelberg, DKFZ, Diploma Thesis

[Bertini69] Bertini H W 1969 Intranuclear-Cascade Calculation of the Secondary Nucleon Spectra from Nucleon-Nucleus Interactions in the Energy Range 340 to 2900 MeV and Comparisons with Experiment *Phys. Rev.* **188** 1711-30

[Blann83] Blann M 1983 Precompound analyses of spectra ans yields following nuclear capture of stopped pions, *Phys. Rev*. **C28** 1648-1662

[Botvina87] Botvina A S, Iljinov A S, Mishustin I N et al 1987 Statistical simulation of the break-up of highly excited nuclei *Nucl. Phys*. **A475** 663

[Botvina97] Botvina A S, Dementyev A V, Smirnova O N, Sobolevsky N M, Toneev V D 1997 MSDM - Multy Stage Dynamical Model. In International Codes and Model Intercomparison for Intermediate Energy Activation Yields, Eds. R.Michel and P.Nagel, NSC/DOC(97)-1, NEA/P&T No 14, OECD, Paris, p.307.

[Botvina05] Private communication

[Bragg05] Bragg W H and Kleeman R 1905 On the Alpha Particles of Radium and Their Loss of Range in Passing through Various Atoms and Molecules *Phil Mag* **10** 138

[Bred00] Brede H J, Hecker O and Hollnagel R 2000 An absorbed dose to water calorimeter for collimated radiation fields *Nucl Instr Method* **A455** 721-732

[Brun78] Brun R et al. GEANT User Guide and Reference Manual. CERN DD/78/2

[Byckl73] Byckling E and Kajantie K 1973 Particle Kinematics *John Wiley and Sons Ltd*, London

[Carls85] Carlsson G A 1985 Theoretical basis for Dosimetry, Academic Press

[Cas95] Castro J R 1995 Results of heavy ion radiotherapy *Radiat. Environ. Biophys.* **34** 45-8

[Cloth88] Cloth P, Filges D et al 1988 R. KFA-Report Jul-2203

[Colem71] Coleman W A and Armstrong T W, 1971, NMTC – A Nucleon-Meson Transport Code*. Nucl. Sci. Eng.* **43** 353

[Dement99] Dementyev A V and Sobolevsky N M 1999 SHIELD-Universal Monte Carlo Hadron Transport Code: Scope and Applications *Radiat. Meas.***30** 553

[Dresner61] Dresner L 1961 EVAP - A FORTRAN Program for Calculating the Evaporation of Various Particles from Excited Nuclei *ORNL-TM-*196

[Emmet75] Emmet M B 1975 The MORSE Monte Carlo Radiation Transport Code System, ORNL-4972

[Fasso93] Fasso A, .Ferrari A, Ranft J, Sala P R et al 1993 FLUKA92*. Proc. of First Workshop on Simulating Accelerator Radiation Environments (SARE 1), Santa Fe, USA,* January 11-15

[Fasso94] Fasso A, .Ferrari A, Ranft J, Sala P R et al 1994 Nuclear models in FLUKA for interactions in the intermediate energy *. Proc. of a Specialists' Meeting* "Intermediate Energy Nuclear Data: Models and Codes", Issy-les-Moulineaux (France), Paris, OECD

[Fesef85] Fesefeld H C 1985 Simulation of Hadronic Showers, physics and applications*. Technical Report* PITHA 85-02, Aachen

[Garls88] Garlsson G A 1985 Theoretical basis for Dosimetry *The dosimetry of ionizing radiations* Vol.1 Academic Press

[Geithner06] Geithner O, Andreo P, Sobolevsky N, Hartmann G and Jäkel O 2006 Calculation of stopping power ratios for carbon ion dosimetry *Phys. Med. Biol.* **51** 2279-2292

[Geiss97] Geiss O 1997 Dissertation Universität GhK Kassel

[Gudima83] Gudima K K, Mashnik S G, Toneev V D 1983 Cascade-Excitation Model of Nuclear Reactions *Nucl. Phys.* **A401** 329

[Gudow04] Gudowska I, Sobolevsky N, Andreo P et al 2004 Ion Beam Transport in tissue-like media using the Monte Carlo code SHIELD-HIT, *Phys. Med. Biol* **49** 1933-1958

[Gunzert04] Gunzert-Marx K 2004, PhD-thesis, Technical University of Darmstadt

[Haber93] Haberer T et al 1993 Magnetic Scanning System for Heavy Ion Therary *Nucl. Instr. Meth.* **A330** 296

[Hartm99] Hartmann G H, Jäkel O et al Determination of water absorbed dose in a carbon ion beam using thimble ionization chambers, *Phys Med Biol* **44** 1193-1206

[Hughes97] Hughes G et al 1997 MCNPXTM-The LAHETTM/MCNPXTM Code Merger *Proc of Third Workshop on Simulating Accelerator Radiation Environments (SARE 3),* Japan

[IAEA00] IAEA 2000 Technical Reports Series -398: Absorbed Dose Determination in External Beam Radiotherapy, International Code of Practice for Dosimetry, Vienna

[ICRU84] Stopping powers for electrons and positrons vol. 37 ICRU Report, 1984 International Commission of Radiation Units and Measurements, Bethesda, Maryland

[ICRU93] Stopping powers and ranges for protons and alpha particles, vol. 49 ICRU Report, 1993 International Commission of Radiation Units and Measurements, Bethesda, Maryland

[ICRU05] Stopping of Ions Heavier Than Helium, vol. 73 ICRU Report, 2005 International Commission of Radiation Units and Measurements, Oxford University Press

[Irving65] Irving D C et al 1965 O5R, A General-Purpose Monte Carlo Neutron Transport Code Kinney W E, 1964, The nucleon transport code, NTC *Report No. ORNL-3622* (Oak Ridge National Laboratory, Oak Ridge, TN)

[Iwase02] Iwase H, Niita K and Nakamura T 2002 *J. Nucl. Sci. Technol.* **39** 1142

[Jäkel06] Jäkel O and Geithner O 2006 The lateral penumbra of carbon ion beam in large depths in water *In preparation*

[Kalin85] Kalinovskiy A N, Mohov N V and Nikitin Y P 1985 Penetration of high energetic particles through the matter M., Энергоатомиздат (Energy-atomedit) (in Russian)

[Kinn64] Kinney W E, 1964, The nucleon transport code, NTC *Report No. ORNL-3610* (Oak Ridge National Laboratory, Oak Ridge, TN)

[Kraft98] Kraft G 1998 Heavy-Ion Therapy at GSI *Phys. Med* 14 Suppl I 86-90

[Krämer94] Krämer M and Kraft G 1994 Calculations of heavy ion track structure *Rad. Environ. Phys.* **33**(2) 91-109

[Krämer00] Krämer M, Jäkel O, Haberer T, Kraft G, Schardt D and Weber U, 2000, Treatment planning for heavy-ion radiotherapy: physical beam model and dose optimization *Phys. Med Biol.* **45** 3299-3317

[Krämer06] Private communication

[Matsuf03] Matsufuji N et al 2003 Influence of fragment of relativistic charged particles on heavy ion radiotherapy *Phys Med Biol* **48** 1605-1623

[Matsuf05] Matsufuji N et al 2005 Spatial fragment distribution from a therapeutic pencil-like carbon beam in water *Phys Med Biol* **50** 3393-3403

[Metrop49] Metropolis N and Ulam S M, 1949, The Monte Carlo method *J. Amer. Statist. Assoc.* **44**, 335-41

[Mokhov74] Mokhov N V 1974 Calculation of particle distribution in accelerator shielding of energy 50MeV-1500GeV with Monte Carlo method Moscow, M., «Наука» (in Russian)

[Mokhov98] Mokhov N V, Striganov S I, A.Van Genniken, Mashnik S G, Sirec A J and Ranft J. 1998 MARS Code Developments. *Proc. of 4th Workshop on Simulating Accelerator Radiation Environments* (SARE 4), Knoxville (TN), USA, September 14-16, 1998. ORNL, Ed. by T.A.Gabriel, p. 87.

[Morse83] MORSE: General Purpose Monte Carlo Multigroup Neutron and Gamma-Ray Transport Code with Combinatorial Geometry, Oak Ridge National laboratory

[Nahum80] Nahum A E and Svensson H, 1980, Electron beam dosimetry: The state of the art, Paper presented at the Tenth Nordic Meeting on Clinical Physics, Finland

[Nara01] Nara Y et al 2001 *Phys Rev* C61 024901

[NCRP27] National Council on Radiation protection and Measurements, 1961 *Stopping Powers for Use with Cavity Chambers,* NCRP Report No. 27, Bethseda

[Nelson85] Nelson W R, Hirayama N and Rogers D W O 1985. The EGS4 Code System, SLAC-265

[Niita95] Niita K et al 1995 *Phys. Rev.* **C52** 2620

[Niita01] Niita K et al 2001 *Nucl. Instr. And Meth.* **B184** 406

[Odder89] Oddershede J and Sabin J R 1989 Bragg Rule Additivity of Bond Stopping Cross Sections *Nucl Instr Meth* **B42** 7

[Paul02] Paul H and Schinner A. 2002 MSTAR – Stopping Power for Light Ions. Available form <http://www.exphys.uni-linz.ac.at/stopping/>

[Paul06A] Paul H 2006 A comparison of recent stopping power tables for light and medium-heavy ions with experimental data, and applications to radiotherapy dosimetry *Nucl Instrum Meth* (submitted)

[Paul06B] Paul H, Geithner O and Jäkel O 2006 The Influence of Stopping Powers upon Dosimetry for Radiation Therapy with energetic Ions *Adv Qu Chem* (in progress)

[Prael88] Prael R E and Bozoian M 1988 Adaptation of the Multistage Preequilibrium Model for the Monte Carlo Method *LA-UR-88-3238*

[Prael89] Prael R E and Lichtenstein H 1989 User Guide to LCS: The LAHET Code System, *LANL report* LA-UR-89-3014

[Prael94] Prael R E 1994 A Review of Physics Models in the LAHET^{TM} *Meeting* Intermediate Energy Nuclear Data: Models and Codes, Paris

[Ranft74] Ranft J and Routti J T 1974 Monte Carlo Programs for Calculating Threedimensional High Energy (50 MeV-500 GeV) Hadron Cascades in Matter*. Comp.Phys.Com*. **7** 327

[Ranft97] Ranft J 1997 DPMJET version II.3 and II.4 *Preprint INFN/AE-97/45*

[Sakam91] Sakamoto N, Ogawa H et al 1991 Stopping Powers of Metallic Elements for High Energy Ions *Radiat Eff* (in press)

[Schall96] Schall *et al* 1996 Charge-changing nuclear reactions of relativistic light-ion beams $(5 \le z \le 10)$ passing through thick absorbers *Nucl Instrum Phys Res* B **117** 221-334

[Scholz97] Scholz, M, Kellerer, AM, Kraft-Weyrather, W, Kraft, G. 1997 Computation of cell survival in heavy ion beams for therapy - the model and its approximation*. Radiat. Environ. Biophysics* **36**, 59-66

[Semp04] Sempau J, Andreo P et al Electron beam quality correction factors for plane-parallel ionization chambers: Monte Carlo calculations using the PENELOPE system *Phys Med Biol* **49** 4427-4444

[Sihver98] Sihver L, Schardt D and Kanai T 1998 Depth-Dose Distributions of High-Energy Carbon, Oxygen and Neon Beams in Water *Jpn J Med Phys* **18** (1)

[Sobol70] Sobolevsky N, 1970, Program for calculations nucleon-meson cascade in media with Monte Carlo method, Dubna (In Russian)

[Sobol96] Sobolevsky N, 1996, Conclusions of International Code Comparison for Intermediate Energy Nuclear Data. Thick Target Benchmark for Lead and Tungsten *Report NEA OECD NSC/DOC* 15

[Sobol00] Sobolevsky N, 2000, The SHIELD Transoprt Code: a tool for Computer Study of Interaction of particles and Nuclei with Complex Media, YUNSC, Belgrade

[Spenc95] Spencer L and Attix F 1995 A theory of cavity ionization, *Rad. Res.* **3,** 239

[Sych79] Sychov B S, Serov A Y and Manko B V 1979 Analytical Approximation of differential cross-sections for secondary particles in inelastic hA-interaction for energies higher then 20MeV Препринт (Pre-print) МРТИ №799, M (in Russian)

[Sych86] Sychov B S, Serov A Y and Manko B V 1986 Analytical Approximation of differential cross-sections for elastic scattering of nucleons of energies higher then 10MeV Вести АН БССР, Сер физико-энергетических наук, №4, Минск (Minsk) (in Russian)

[Toneev83] Toneev V D, Gudima K K 1983 Particle emission in light and heavy ion reactions *Nucl. Phys*. **A400** 173

[Tsu94] Tsujii T, Morita K, Mizoe J, Miyamoto T, Mukai M, Nakano T and Moriat S 1994 HIMAC clinical plans and protocols for light ion therapy *Abstract of the XX PTGOC Meeting(Chester)* (Cambridge, MA: Proton Therapy Co-Operative Group) p 22

[Yariv79] Yariv Y and Fraenkel Z 1979 Intranuclear cascade calculation of high-energy heavy-ion interactions *Phy.s Rev.* **C20** 2227

[Weber99] Weber U and Kraft G 1999 Design and construction of a ripple filter for a smoothed depth dose distribution in conformal particle therapy *Phys Med Biol* **44** 2765-2775

[Wilkens06] Wilkens J 2006 Private communication

Acknowledgement

There were many people who contributed to the success of this thesis and who supported me during the last three years. Finally, I have the possibility to express my gratitude to them. These people are:

- Prof. Dr. W. Schlegel, who gave me the possibility to work in his department. He supported my ideas of further education in the field of medical physics.
- My direct supervisor and doctor father Prof. Dr. Oliver Jäkel. Being very friendly and easy going, he was a great help during the time of my project, not only the most important scientific advisor during discussions, but also an anchor stone in all ups and downs which happen during a PhD work. Exceptional I found his openness for my plans about further education. Without his support, it would not have been possible to learn German intensively and to attend educational courses.
- My referee Prof. Dr. J. Bille kindly took over the task of acting as second corrector of my thesis.
- Prof. Dr. P. Andreo, as a very important contributor and inspirer. He was one of the main scientific partners in discussions and generator of ideas, teaching me principles of dosimetry and aspects of Monte Carlo simulations.
- Prof. Dr. N. Sobolevsky for his help and great contribution to the improvements of SHIELD-HIT. He introduced me to the world of Monte Carlo computation, sharing his deep knowledge and experience.
- Prof. Dr. G. Hartmann as a very important discussion partner. He always supported me in all aspects of this PhD project.
- Prof. Dr. H. Paul for the nice collaboration and fruitful discussions about stopping powers and importance of the ionization potential.
- Michael Krämer, who provided the calculations with TRiP BEAM.
- The members of our small group: Sima, Malte, Benjamin, Marina, Christian, Peter and Tobias. They were always willing to help and support. Special thanks go to Peter, Christian, Benjamin and Malte for their great help and friendly atmosphere during our beam times.
- The colleagues of our department: Urban, Anja, Monika, Gerhard, Thomas, Maria, Wolfram and Ralf. To them I want to express my gratitude for providing a nice group

spirit and support. They are not only colleagues, but also friends, who were (and hopefully will remain) very important for my social life.

- My best friends Larisa and Svetlana. They were always near when I needed them and gave friendly support in all phases of my life during this work.
- My parents deserve the utmost thank. They supported me with love and material goods during my studies. Furthermore, they let their only daughter go to a foreign country far away from home, leaving the telephone as only means of being close to each other.
- Last but not least my dear husband Wolfgang for his never-ending patience with his always-working wife. Moreover, he was a friendly and constructive critic, who never refused to do a bit of reviewing of this thesis. Finally, most of all I am grateful for this support and care and for the fact that life together with him is much more beautiful.